

AD-A041 534

MCDONNELL DOUGLAS RESEARCH LABS ST LOUIS MO
DEVELOPMENT OF THE HGCDSE ALLOY SYSTEM FOR INFRARED SENSOR APPL--ETC(U)
FEB 77 C R WHITSETT, C J SUMMERS

F/G 17/5

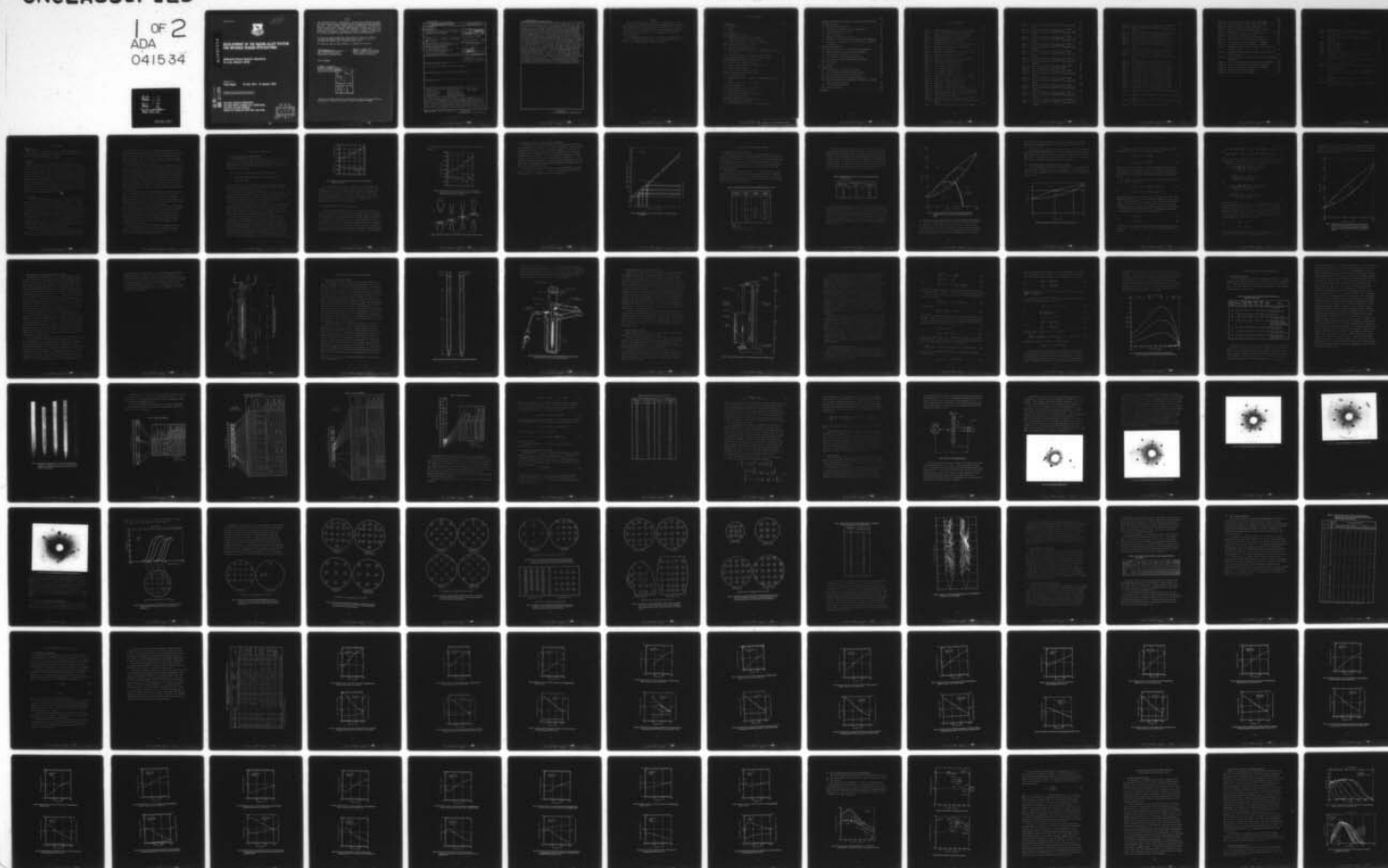
F33615-74-C-5167

UNCLASSIFIED

AFAL-TR-76-112

NL

1 OF 2
ADA
041534





92

AD A 041534

DEVELOPMENT OF THE HgCdSe ALLOY SYSTEM FOR INFRARED SENSOR APPLICATIONS

McDonnell Douglas Research Laboratories
St. Louis, Missouri 63166

FEBRUARY 1977

Final Report

15 July 1974 - 15 January 1976

Approved for public release; distribution unlimited

AD No. _____
DDC FILE COPY

AIR FORCE AVIONICS LABORATORIES
AIR FORCE WRIGHT AERONAUTICAL LABORATORIES
AIR FORCE SYSTEMS COMMAND
WRIGHT-PATTERSON AIR FORCE BASE, OHIO 45433

DDC
RECEIVED
JUL 11 1977
A

NOTICE

When Government drawings, specifications, or other data are used for any purpose other than in connection with a definitely related Government procurement operation, the United States Government thereby incurs no responsibility nor any obligation whatsoever; and the fact that the government may have formulated, furnished, or in any way supplied the said drawings, specifications, or other data, is not to be regarded by implication or otherwise as in any manner licensing the holder or any other person or corporation, or conveying any rights or permission to manufacture, use, or sell any patented invention that may in any way be related thereto.

This report has been reviewed by the Information Office (OI) and is releasable to the National Technical Information Service (NTIS). At NTIS, it will be available to the general public, including foreign nations.

This technical report has been reviewed and is approved for publication.

Thad Pickenpaugh
THAD PICKENPAUGH, Project Monitor
Electro-Optic Detectors Group
Electro-Optics Technology Branch

Robert L. Hickmott
ROBERT L. HICKMOTT, Project Monitor
Laser and Optical Materials Branch
Air Force Materials Laboratory

FOR THE COMMANDER

William C. Schoonover
WILLIAM C. SCHOONOVER, Chief
Electro-Optics Technology Branch
Electronic Technology Division

DTIC	WH/AS Section	<input checked="" type="checkbox"/>
DDO	Soft Section	<input type="checkbox"/>
OWANDOUNCED		<input type="checkbox"/>
JUSTIFICATION		
BY		
DISTRIBUTION/AVAILABILITY CODES		
Dist.	AVAIL. and/or SPECIAL	
A		

Copies of this report should not be returned unless return is required by security considerations, contractual obligations, or notice on a specific document.

UNCLASSIFIED

SECURITY CLASSIFICATION OF THIS PAGE (When Data Entered)

19 REPORT DOCUMENTATION PAGE		READ INSTRUCTIONS BEFORE COMPLETING FORM
1. REPORT NUMBER AFAL-TR-76-112	2. GOVT ACCESSION NO.	3. RECIPIENT'S CATALOG NUMBER
4. TITLE (and Subtitle) DEVELOPMENT OF THE HgCdSe ALLOY SYSTEM FOR INFRARED SENSOR APPLICATIONS.		5. TYPE OF REPORT & PERIOD COVERED Final Report, for the Period 15 July 1974-15 Feb 1976
7. AUTHOR(s) C. R. Whitsett, C. J. Summers, J. G. Broerman and D. A. Nelson		6. PERFORMING ORG. REPORT NUMBER
9. PERFORMING ORGANIZATION NAME AND ADDRESS McDonnell Douglas Research Laboratories McDonnell Douglas Corporation St. Louis, Missouri 63166		8. CONTRACT OR GRANT NUMBER(s) F33615-74-C-5167 new
11. CONTROLLING OFFICE NAME AND ADDRESS Air Force Avionics Laboratory (DHO) Air Force Systems Command Wright-Patterson Air Force Base, Ohio 45433		10. PROGRAM ELEMENT, PROJECT, TASK AREA & WORK UNIT NUMBERS Project No. 7371
14. MONITORING AGENCY NAME & ADDRESS (if different from Controlling Office)		12. REPORT DATE February 1977
		13. NUMBER OF PAGES 146 12-148 p.
		15. SECURITY CLASS. (for this report) Unclassified
		15a. DECLASSIFICATION DOWNGRADING SCHEDULE
16. DISTRIBUTION STATEMENT (of this Report) Approved for public release; distribution unlimited.		
17. DISTRIBUTION STATEMENT (of the abstract entered in Block 20, if different from Report)		
18. SUPPLEMENTARY NOTES		
19. KEY WORDS (Continue on reverse side if necessary and identify by block number) Mercury cadmium selenide Electrical conductivity Phase diagram Semiconductor Hall coefficient Laue topography Infrared detection Infrared transmittance Photoconductivity Infrared absorptance Crystal growth Recombination lifetime		
20. ABSTRACT (Continue on reverse side if necessary and identify by block number) A study was made of the crystal growth, electrical characteristics, optical absorption, and photoconductivity of mercury-cadmium-selenide ($\text{Hg}_{1-x}\text{Cd}_x\text{Se}$) alloys and of the pseudobinary HgSe-CdSe phase diagram. Emphasis was given to alloy compositions suitable for infrared photoconductive-detectors in the 2.5-2.8, 4.2-4.5, and 8-14 μm wavelength intervals. The liquidus temperature-composition curve for the HgSe-CdSe system implies an entropy of mixing of $-2.69x(1-x)$ J/mol, and the solidus curve conforms closely to that of an ideal solution.		

DD FORM 1 JAN 73 1473

EDITION OF 1 NOV 65 IS OBSOLETE

UNCLASSIFIED

SECURITY CLASSIFICATION OF THIS PAGE (When Data Entered)

405315

Jace

UNCLASSIFIED

SECURITY CLASSIFICATION OF THIS PAGE(When Data Entered)

The ideal-solution behavior of the solid solutions of HgSe and CdSe is consistent with the small variation with x of the interatomic spacing. $\text{Hg}_{1-x}\text{Cd}_x\text{Se}$ alloys with $x < 0.55$ solidify from the melt with the cubic, zincblende crystal structure, and higher- x alloys crystallize from the melt with the hexagonal, wurtzite structure. Solid in equilibrium with the melt transforms by peritectic reaction at $947 \pm 4^\circ\text{C}$ from the zincblende to the wurtzite structure. Large single-crystals that had average x -values from 0.16 to 0.33 were grown by the Bridgman method. All of the $\text{Hg}_{1-x}\text{Cd}_x\text{Se}$ crystals were n -type and had extrinsic conduction-electron concentrations from 1.3×10^{16} to $5.2 \times 10^{17}\text{cm}^{-3}$. Annealing in vacuum at 200-300 K reduced the conduction-electron concentration in as-grown $\text{Hg}_{1-x}\text{Cd}_x\text{Se}$ crystals by as much as an order of magnitude. Annealing in Se-vapor at 200-300 K had little effect on the conduction-electron concentration but increased the ratio of the 4.2 K mobility to the 300 K mobility. The electron mobility at 4.2 K was between 5 000 and 27 000 $\text{cm}^2/\text{V}\cdot\text{s}$ for samples that had $0.60 < x < 0.15$, and the mobility was higher for smaller x and lower electron concentration. At 300 K, the electron mobility for the same samples ranged from 1000 to 8000 $\text{cm}^2/\text{V}\cdot\text{s}$. By fitting optical absorptance data for $\text{Hg}_{1-x}\text{Cd}_x\text{Se}$ crystals with $0.15 < x < 0.30$, it was determined that the energy gap in electronvolts is given at 80 K by the relation $E_G = -0.20 + 1.70x$ and at 300 K by the relation $E_G = -0.06 + 1.57x$. The infrared photoconductive responsivity at 77 and 300 K is limited by radiative recombination of electron-hole pairs, and the excess-carrier lifetime at 77 K in specimens with approximately 10^{10} electrons/ cm^3 is 0.5 μs . For Johnson-noise as the dominant contributor to noise-equivalent-power, the photoconductivity results imply that $\text{Hg}_{1-x}\text{Cd}_x\text{Se}$ crystals with fewer than 5×10^{15} electrons/ cm^3 can have the theoretical maximum detectivity under 300 K background operating conditions.

UNCLASSIFIED

SECURITY CLASSIFICATION OF THIS PAGE(When Data Entered)

PREFACE

This report for the period 15 July 1974 to 15 February 1976 is the final report of work performed by the McDonnell Douglas Research Laboratories under United States Air Force Contract No. F33615-74-C-5167. The contract is monitored by Mr. R. L. Hickmott for the Air Force Materials Laboratory and, effective 1 July 1975, by Mr. T. D. Pickenpaugh for the Air Force Avionics Laboratory.

The principal investigator is Dr. C. R. Whitsett. Co-investigators are Dr. C. J. Summers, Mr. D. A. Nelson, Dr. J. G. Broerman, and Dr. B. B. Rath. Mr. D. S. Wright provides technical assistance.

TABLE OF CONTENTS

	Page
1 INTRODUCTION	1
1.1 Objective	1
1.2 Scope	1
1.3 Rationale	1
2 THE $\text{Hg}_{1-x}\text{Cd}_x\text{Se}$ ALLOY SYSTEM	3
2.1 Crystal Structure and Lattice Constant	3
2.2 Energy Band Structure of $\text{Hg}_{1-x}\text{Cd}_x\text{Se}$ Alloys	4
2.3 Estimated Variation of Band Gap with Composition	6
3 PHASE DIAGRAM OF THE HgSe-CdSe SYSTEM	8
3.1 Liquidus and Solidus Temperatures	8
3.2 Peritectic Reaction and Miscibility Gap Between Crystallographic Phases	10
3.3 Theoretical Analysis of Binary-Alloy Phase Diagram	11
3.4 Experimental Method for Determining Thermal Arrests	15
4 ALLOY PREPARATION AND CRYSTAL GROWTH METHODS	18
4.1 Reaction of the Alloying Elements	18
4.2 Single-Crystal Growth by the Bridgman Method	21
4.3 Capsule Rupture Problem	21
4.4 Vapor Pressures within the Capsules	23
5 CRYSTAL PREPARATIONS AND CHARACTERIZATION	27
5.1 Crystal Preparations	27
5.2 Determination of Alloy Composition by Mass Density Measurements	33
5.3 Method of Measurement of Mass Density	34
5.4 Laue Topography	37
5.5 Compositional Homogeneity Determinations	43
5.6 Vacuum Annealing of $\text{Hg}_{1-x}\text{Cd}_x\text{Se}$	53
5.7 Selenium-Vapor Annealing of $\text{Hg}_{1-x}\text{Cd}_x\text{Se}$	53
5.8 Trace Impurity Analyses	55
6 ELECTRICAL PROPERTIES OF $\text{Hg}_{1-x}\text{Cd}_x\text{Se}$ ALLOYS	57
6.1 Galvanomagnetic Measurements	57
6.2 Electron Mobility as Function of Alloy Composition	79

	Page
7 INFRARED ABSORPTION AND DEPENDENCE OF ENERGY GAP ON COMPOSITION OF $\text{Hg}_{1-x}\text{Cd}_x\text{Se}$ ALLOYS	82
7.1 Infrared Optical Absorption	82
7.2 Preparation of Samples for Optical Measurements	83
7.3 Infrared Transmittance Spectra	83
7.4 Index of Refraction	89
7.5 Absorptance Spectra Calculations	91
7.6 Dependence of the Energy Gap on Composition and Temperature	94
7.7 Calculation of Absorption Coefficient for Direct Interband Transitions	101
8 INFRARED PHOTOCONDUCTIVITY	109
8.1 Sample Preparation for Photoconductivity Measurements	109
8.2 Photoconductivity Spectral-Response Measurements	110
8.3 Photoconductive Charge-Carrier Lifetime	116
8.4 Photoconductivity Time-Response Measurements	116
8.5 Calculation of Radiative-Recombination Lifetimes	124
9 DEVICE FEASIBILITY	128
9.1 Detectivity	128
10 CONCLUSIONS	130
10.1 Phase Diagram of the HgSe-CdSe Systems	130
10.2 Alloy Preparation and Crystal-Growth Methods	130
10.3 Crystal Preparations and Characterization	131
10.4 Electrical Properties of the $\text{Hg}_{1-x}\text{Cd}_x\text{Se}$ Alloys	131
10.5 Infrared Absorption and Dependence of Energy Gap on Composition of $\text{Hg}_{1-x}\text{Cd}_x\text{Se}$ Alloys	132
10.6 Infrared Photoconductivity	132
10.7 Device Feasibility	132
REFERENCES	134

LIST OF ILLUSTRATIONS

	Page
Figure 1 Interatomic distance in $\text{Hg}_{1-x}\text{Cd}_x\text{Se}$ and $\text{Hg}_{1-x}\text{Cd}_x\text{Te}$	4
Figure 2 Lattice-constant in $\text{Hg}_{1-x}\text{Cd}_x\text{Se}$ and $\text{Hg}_{1-x}\text{Cd}_x\text{Te}$	5
Figure 3 Transition to negative band-gap in $\text{Hg}_{1-x}\text{Cd}_x\text{Se}$	5
Figure 4 Estimated dependences of the energy gap on x	7
Figure 5 Pseudobinary HgSe-CdSe phase diagram	10
Figure 6 Phase diagram for binary-alloy system	11
Figure 7 Liquidus and solidus curves for the HgSe-CdSe system . .	14
Figure 8 Experimental arrangement for thermal-arrests	17
Figure 9 Dimensions of quartz tubes	19
Figure 10 Experimental arrangement for sealing quartz tubes	20
Figure 11 Apparatus for growing single crystals	22
Figure 12 Partial pressures of Hg, Cd, and Se_2	26
Figure 13 $\text{Hg}_{1-x}\text{Cd}_x\text{Se}$ recrystallized by the Bridgman method	29
Figure 14 Diagram of Laue topography apparatus	38
Figure 15 Laue topograph of HgCdSe 16E slice	39
Figure 16 Laue topograph of HgCdSe 24A slice	40
Figure 17 Laue topograph of HgCdSe 24A slice	41
Figure 18 Laue topograph of HgCdSe 24A slice	42
Figure 19 Laue topograph of HgCdSe 33A slice	43
Figure 20 Transmittance spectra at 300 K for 1 mm diam areas . . .	44
Figure 21 Homogeneity of 16DAH and 16DCD slices	45
Figure 22 Homogeneity of 16EA6 and 16EB4 slices	46
Figure 23 Homogeneity of 16EB7 and 16EB12 slices	47
Figure 24 Homogeneity of 16EC8 and 16EC12 slices	48
Figure 25 Homogeneity of 24AC13 and 24AC15 slices	48
Figure 26 Homogeneity of 24AA1, 24AA3, 24AB14, and 24AB16 slices .	49
Figure 27 Homogeneity of 33AT1, 33AT4, 33AT8, and 33AT11 slices .	50
Figure 28 Equal-x contours in HgCdSe 24A	52
Figure 29 Electrical resistivity of $\text{Hg}_{0.847}\text{Cd}_{0.153}\text{Se}$ (16EC8) . . .	60
Figure 30 Electron concentration and mobility of $\text{Hg}_{0.847}\text{Cd}_{0.153}\text{Se}$ (16EC8)	60
Figure 31 Electrical resistivity of $\text{Hg}_{0.847}\text{Cd}_{0.153}\text{Se}$ (16EC12) . . .	61

	Page
Figure 32 Electron concentration and mobility of $\text{Hg}_{0.847}\text{Cd}_{0.153}\text{Se}$ (16EC12)	61
Figure 33 Electrical resistivity of $\text{Hg}_{0.838}\text{Cd}_{0.162}\text{Se}$ (16DAH)	62
Figure 34 Electron concentration and mobility of $\text{Hg}_{0.838}\text{Cd}_{0.162}\text{Se}$ (16DAH)	62
Figure 35 Electrical resistivity of $\text{Hg}_{0.806}\text{Cd}_{0.194}\text{Se}$ (16EB12) . . .	63
Figure 36 Electron concentration and mobility of $\text{Hg}_{0.806}\text{Cd}_{0.194}\text{Se}$ (16EB12)	63
Figure 37 Electrical resistivity of $\text{Hg}_{0.806}\text{Cd}_{0.194}\text{Se}$ (16EB12-S) . .	64
Figure 38 Electron concentration and mobility of $\text{Hg}_{0.806}\text{Cd}_{0.194}\text{Se}$ (16EB12-S)	64
Figure 39 Electrical resistivity of $\text{Hg}_{0.793}\text{Cd}_{0.207}\text{Se}$ (16EB7)	65
Figure 40 Electron concentration and mobility of $\text{Hg}_{0.793}\text{Cd}_{0.207}\text{Se}$ (16EB7)	65
Figure 41 Electrical resistivity of $\text{Hg}_{0.793}\text{Cd}_{0.207}\text{Se}$ (16EB7-S) . . .	66
Figure 42 Electron concentration and mobility of $\text{Hg}_{0.793}\text{Cd}_{0.207}\text{Se}$ (16EB7-S)	66
Figure 43 Electrical resistivity of $\text{Hg}_{0.791}\text{Cd}_{0.209}\text{Se}$ (16DCD)	67
Figure 44 Electron mobility of $\text{Hg}_{0.791}\text{Cd}_{0.209}\text{Se}$ (16DCD)	67
Figure 45 Electrical resistivity of $\text{Hg}_{0.784}\text{Cd}_{0.216}\text{Se}$ (24AC15)	68
Figure 46 Electron concentration and mobility of $\text{Hg}_{0.784}\text{Cd}_{0.216}\text{Se}$ (24AC15)	68
Figure 47 Electrical resistivity of $\text{Hg}_{0.772}\text{Cd}_{0.228}\text{Se}$ (16EA6)	69
Figure 48 Electron concentration and mobility of $\text{Hg}_{0.772}\text{Cd}_{0.228}\text{Se}$ (16EA6)	69
Figure 49 Electrical resistivity of $\text{Hg}_{0.749}\text{Cd}_{0.251}\text{Se}$ (24AB14)	70
Figure 50 Electron concentration and mobility of $\text{Hg}_{0.749}\text{Cd}_{0.251}\text{Se}$ (24AB14)	70
Figure 51 Electrical resistivity of $\text{Hg}_{0.703}\text{Cd}_{0.297}\text{Se}$ (24AC13)	71
Figure 52 Electron concentration and mobility of $\text{Hg}_{0.703}\text{Cd}_{0.297}\text{Se}$ (24AC13)	71
Figure 53 Electrical resistivity of $\text{Hg}_{0.672}\text{Cd}_{0.328}\text{Se}$ (24AB16-1) . .	72
Figure 54 Electron concentration and mobility of $\text{Hg}_{0.672}\text{Cd}_{0.328}\text{Se}$ (24AB16-1)	72

	Page
Figure 55 Electrical resistivity of $\text{Hg}_{0.672}\text{Cd}_{0.328}\text{Se}$ (24AB16-2) . . .	73
Figure 56 Electron concentration and mobility of $\text{Hg}_{0.672}\text{Cd}_{0.328}\text{Se}$ (24AB16-2)	73
Figure 57 Electrical resistivity of $\text{Hg}_{0.648}\text{Cd}_{0.352}\text{Se}$ (24AA1-1) . . .	74
Figure 58 Electron mobility of $\text{Hg}_{0.648}\text{Cd}_{0.352}\text{Se}$ (24AA1-1)	74
Figure 59 Electrical resistivity of $\text{Hg}_{0.648}\text{Cd}_{0.352}\text{Se}$ (24AA1-2) . . .	75
Figure 60 Electron mobility of $\text{Hg}_{0.648}\text{Cd}_{0.352}\text{Se}$ (24AA1-2)	75
Figure 61 Electrical resistivity of $\text{Hg}_{0.648}\text{Cd}_{0.352}\text{Se}$ (24AA1-3) . . .	76
Figure 62 Electron concentration and mobility of $\text{Hg}_{0.648}\text{Cd}_{0.352}\text{Se}$ (24AA1-3)	76
Figure 63 Electrical resistivity of $\text{Hg}_{0.634}\text{Cd}_{0.366}\text{Se}$ (24AA3-S) . . .	77
Figure 64 Electron mobility of $\text{Hg}_{0.634}\text{Cd}_{0.366}\text{Se}$ (24AA3-S)	77
Figure 65 Electrical resistivity of $\text{Hg}_{0.400}\text{Cd}_{0.600}\text{Se}$ (33AT1)	78
Figure 66 Electron concentration and mobility of $\text{Hg}_{0.400}\text{Cd}_{0.600}\text{Se}$ (33AT1)	78
Figure 67 Electron mobilities of $\text{Hg}_{1-x}\text{Cd}_x\text{Se}$ alloys at 4.2 K	79
Figure 68 Electron mobilities of $\text{Hg}_{1-x}\text{Cd}_x\text{Se}$ alloys at 80 K	80
Figure 69 Electron mobilities of $\text{Hg}_{1-x}\text{Cd}_x\text{Se}$ alloys at 300 K	80
Figure 70 Transmittance spectra for $\text{Hg}_{0.847}\text{Cd}_{0.153}\text{Se}$ (16EC8)	84
Figure 71 Transmittance spectra for $\text{Hg}_{0.838}\text{Cd}_{0.162}\text{Se}$ (16DAH)	84
Figure 72 Transmittance spectra for $\text{Hg}_{0.806}\text{Cd}_{0.194}\text{Se}$ (16EB12)	85
Figure 73 Transmittance spectra for $\text{Hg}_{0.791}\text{Cd}_{0.209}\text{Se}$ (16DCD)	85
Figure 74 Transmittance spectra for $\text{Hg}_{0.775}\text{Cd}_{0.225}\text{Se}$ (16EB4)	86
Figure 75 Transmittance spectra for $\text{Hg}_{0.772}\text{Cd}_{0.228}\text{Se}$ (16EA6)	87
Figure 76 Transmittance spectra for $\text{Hg}_{0.747}\text{Cd}_{0.253}\text{Se}$ (16LG)	87
Figure 77 Transmittance spectra for $\text{Hg}_{0.703}\text{Cd}_{0.297}\text{Se}$ (24AC13)	88
Figure 78 Transmittance spectra for $\text{Hg}_{0.634}\text{Cd}_{0.366}\text{Se}$ (24AA3)	88
Figure 79 Absorption coefficient spectra at 30 K for $\text{Hg}_{0.747}\text{Cd}_{0.253}\text{Se}$ (16LG)	92
Figure 80 Absorption coefficient spectra at 125 K for $\text{Hg}_{0.747}\text{Cd}_{0.253}\text{Se}$ (16LG)	93
Figure 81 Absorption coefficient spectra at 200 K for $\text{Hg}_{0.747}\text{Cd}_{0.253}\text{Se}$ (16LG)	93
Figure 82 Optical energy gap for $\text{Hg}_{0.847}\text{Cd}_{0.153}\text{Se}$ (16EC8)	95

	Page
Figure 83 Optical energy gap for $\text{Hg}_{0.806}\text{Cd}_{0.194}\text{Se}$ (16EB12)	96
Figure 84 Optical energy gap for $\text{Hg}_{0.773}\text{Cd}_{0.227}\text{Se}$ (16EA6)	97
Figure 85 Optical energy gap for $\text{Hg}_{0.747}\text{Cd}_{0.253}\text{Se}$	98
Figure 86 Optical energy gap for $\text{Hg}_{0.703}\text{Cd}_{0.297}\text{Se}$ (24AC13)	99
Figure 87 Energy gap as a function of x in $\text{Hg}_{1-x}\text{Cd}_x\text{Se}$	100
Figure 88 Six-contact photo-Hall bar element	109
Figure 89 Apparatus for photoconductive measurements	110
Figure 90 Photoconductive spectral response for 24AA1PC1	111
Figure 91 Photoconductive spectral response for 24AB16PC1	112
Figure 92 Photoconductive spectral response for 24AB14PC2	113
Figure 93 Dependence of photoconductive signal on bias voltage for element 24AA1PC1	114
Figure 94 Dependence of photoconductive signal on bias voltage for element 24AB14PC2	115
Figure 95 Temporal output of GaAs laser diode used for time response measurements	117
Figure 96 Decay of photoconductive response for element 24AB16PC1	118
Figure 97 Effect of minority-carrier trapping for 24AB16PC1	119
Figure 98 Decay of photoconductive response for 24AB14PC2	120
Figure 99 Radiative lifetime for 24AB16PC1	122
Figure 100 Radiative lifetime for 24AB14PC2	123

LIST OF TABLES

	Page
TABLE 1 PHASE-DIAGRAM DATA FOR THE PSEUDOBINARY HgSe-CdSe SYSTEM . .	8
TABLE 2 COMPOSITIONS OF SOLIDS TO FIRST FREEZE FROM DIFFERENT Hg _{1-x} Cd _x Se MELTS	9
TABLE 3 Hg _{1-x} Cd _x Se ALLOY PREPARATIONS IN CHRONOLOGICAL ORDER OF PROCESSING	27
TABLE 4 HgCdSe 16D SAMPLES	30
TABLE 5 HgCdSe 16E SAMPLES	31
TABLE 6 HgCdSe 24A SAMPLES	32
TABLE 7 HgCdSe 33A SAMPLES	33
TABLE 8 MASS DENSITY OF Hg _{1-x} Cd _x Se ALLOYS	35
TABLE 9 APPROXIMATE x-VALUES CORRESPONDING TO TRANSMISSION-EDGE WAVELENGTHS FOR Hg _{1-x} Cd _x Se AT 300 K	51
TABLE 10 ELECTRICAL CHARACTERISTICS OF Hg _{0.71} Cd _{0.29} Se ANNEALED IN Se VAPOR	54
TABLE 11 TRACE IMPURITY ANALYSES OF HgCdSe 16D and 16E.	56
TABLE 12 RESULTS OF GALVANOMAGNETIC MEASUREMENTS AT 4.2, 80, AND 300 K ON Hg _{1-x} Cd _x Se CRYSTALS	59
TABLE 13 INDEX OF REFRACTION OF Hg _{1-x} Cd _x Se ALLOYS AT DIFFERENT TEMP- ERATURES; BASED ON TRANSMITTANCE-SPECTRA INTERFERENCE FRINGES	90
TABLE 14 PHOTOCONDUCTIVE RESPONSE OF Hg _{1-x} Cd _x Se PHOTO-HALL-BAR ELEMENTS WITH 0.5 V BIAS	113
TABLE 15 CALCULATED DETECTIVITY FOR JOHNSON-NOISE-LIMITED CONDITION OF Hg _{1-x} Cd _x Se PHOTO-HALL-BAR ELEMENTS	129

1. INTRODUCTION

1.1 Objective

The objective of this program was to establish the feasibility of developing selected compositions from the mercury-cadmium-selenide alloy system for infrared sensor applications.

1.2 Scope

The Air Force has requirements in three wavelength regions of the infrared spectrum: 2.5-2.8 μm , 4.2-4.5 μm , and 8-14 μm . The emphasis in this program was on compositions of mercury-cadmium-selenide suitable for these wavelength regions. Principal questions that were to be answered by this research program are: What alloy compositions correspond to the wavelengths of interest? Are these compositions readily grown with reasonably large single-crystal regions where the ratio of mercury to cadmium is uniform? Can stoichiometry be adjusted to provide low carrier concentration, high carrier mobility, and long carrier lifetime? Are there special features such as traps for minority carriers, a large ratio of electron-mobility to hole-mobility, or good stability in vacuum at elevated temperatures to permit high-temperature bake-out?

1.3 Rationale

The mercury-cadmium-telluride alloy system has many infrared sensor applications because the cut-off wavelength can be varied by adjusting the ratio of mercury to cadmium. Mercury-cadmium-selenide is a similar alloy system, but it has not been developed, in part because the alloys crystallize in two different structures but chiefly because the alloys have high melting temperatures and thus are more difficult to prepare than the HgCdTe alloys. The compositions of HgCdSe alloys that are of importance for infrared detector applications crystallize in the cubic, zincblende structure, and the existence of a second crystal structure for high-cadmium compositions is not a factor. For the research reported here, a broad range of compositions of HgCdSe alloys was prepared, and the high melting temperatures presented no serious problems.

There are no good reasons that the HgCdSe alloys should not be as practical as the HgCdTe alloys. The electron energy-band structures of the two alloys are nearly identical, and their intrinsic electrical and

optical characteristics are similar. The most significant difference is that the HgCdSe alloys form with a stoichiometric excess of Hg, which makes them n-type, whereas the HgCdTe alloys form with a Hg deficiency, which tends to make them p-type. The annealing procedures and chemical dopants that must be employed to control the electrical characteristics, therefore, must be different for the two alloy systems.

To convert HgCdTe alloys to n-type, they must be annealed in Hg vapor to reduce the Hg-vacancy concentration in as-grown material and/or chemical donor-dopants must be added to the melt during their preparation. If devices made from the HgCdTe must be operated in a vacuum enclosure, the alloy will tend to lose Hg and thus the effect of Hg-vapor annealing will be partially reversed. As-grown HgCdSe has an excess of Hg, which must be removed by annealing in vacuum. A HgCdSe-alloy device will thus be stable in a vacuum enclosure. Furthermore, after sufficient development of purification and chemical-doping methods for HgCdSe, it should be possible to prepare these alloys as n-type with less compensation and thus higher electron mobilities than n-type HgCdTe.

The crystal-lattice mismatch between the end-point compounds, HgSe and CdSe, of the HgCdSe system is very small, and this favors the growth of large, single crystals even when the alloy composition is not uniform. Moreover, because of the close crystal-lattice match, the contribution from lattice strain to the "alloying effect" on the lattice vibrations and charge-carrier mobilities will be minimal for the HgCdSe alloys.

The differences in the dominant defects, Hg interstitials in the HgCdSe alloys and Hg vacancies in HgCdTe, undoubtedly will be reflected in differences in the charge-carrier trapping and surface states between the two alloy systems, although this has not yet been studied. The different chemical dopants that must be used to control the charge-carrier concentrations in the two alloy systems will likely cause further differences in trapping phenomena and consequently the infrared photoconductivity responsivity and response-time.

On the basis of the present understanding of the HgCdSe alloys, the prospect is promising that they will be superior for applications that require large, homogeneous, single crystals of high-mobility, n-type, small-to-medium band-gap, semiconducting material.

2. THE $\text{Hg}_{1-x}\text{Cd}_x\text{Se}$ ALLOY SYSTEM

2.1 Crystal Structure and Lattice Constant

The compound HgSe crystallizes in the cubic, zincblende structure. In this structure the Hg atoms form a face-centered-cubic sublattice, and the Se atoms form another face-centered-cubic sublattice displaced one-quarter of a body diagonal from the Hg lattice. Within a cubic unit cell of edge a_0 , the coordinates of the atoms are:

$$\text{Hg: } (0,0,0), (a_0/2, a_0/2, 0), (a_0/2, 0, a_0/2), (0, a_0/2, a_0/2)$$

$$\text{Se: } (3a_0/4, a_0/4, a_0/4), (a_0/4, 3a_0/4, a_0/4), (a_0/4, a_0/4, 3a_0/4), \\ (3a_0/4, 3a_0/4, a_0/4).$$

The lattice constant, a_0 , at 20°C has been measured as 6.088 \AA by Cruceanu, Nistor, and Niculescu¹, 6.085 \AA by Swanson, Gilfrich, and Cook², 6.086 \AA by Singh and Dayal³, and 6.086 \AA by Kalb and Leute⁴.

The compound CdSe crystallizes in the hexagonal, wurtzite structure. The 20°C lattice constants a and c have been measured as 4.299 and 7.010 \AA by Swanson, Gilfrich, and Cook⁵, 4.300 and 7.020 \AA by Kot and Mshenskii⁶, 4.309 and 7.024 \AA by Stuckes and Farell⁷, 4.298 and 6.009 \AA by Cruceanu and Niculescu⁸, and 4.301 and 7.014 \AA by Kalb and Leute⁴.

The zincblende and wurtzite lattices are both formed by tetrahedral bonding between anions and cations. The closest packing of atoms occurs in the $\{111\}$ planes of the zincblende lattice, and the $\{111\}$ planes of each atom species have an ABCABC... stacking sequence. The packing is identical in the wurtzite $\{0001\}$ planes, but the stacking sequence is ABAB....

The Se-Se interatomic spacing is nearly equal in HgSe (4.303 \AA) and CdSe (4.301 \AA). For comparison, the Te-Te spacing is 4.569 \AA in HgTe and 4.583 \AA in CdTe , both of which have the zincblende structure. The data of Kalb and Leute⁴ have been used to construct the plot, shown in Figure 1, of the Se-Se interatomic spacing as a function of x for the $\text{Hg}_{1-x}\text{Cd}_x\text{Se}$ system. As x increases, the interatomic spacing slowly decreases until $x = 0.65$; the interatomic spacing then decreases rapidly. Between $x = 0.77$ and $x = 0.81$, the zincblende structure transforms to the wurtzite structure at 20°C , and above $x = 0.81$ the Se-Se interatomic spacing is nearly the same as for $x < 0.65$.

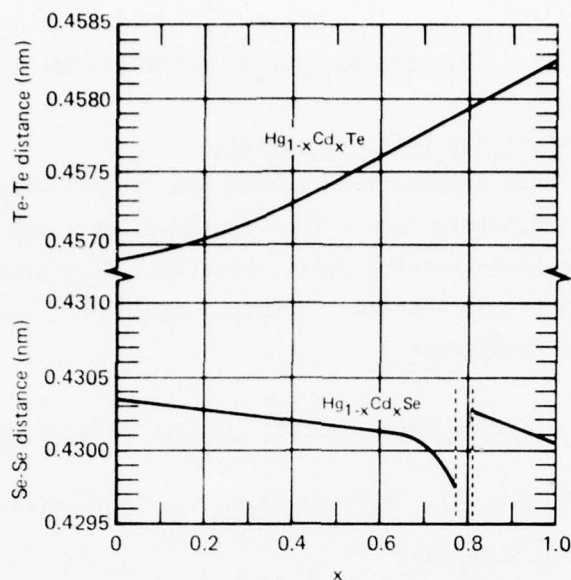


Figure 1 Se-Se and Te-Te interatomic distance as a function of x in the $\text{Hg}_{1-x}\text{Cd}_x\text{Te}$ and $\text{Hg}_{1-x}\text{Cd}_x\text{Se}$ alloys

The variation with x of the lattice constants for the $\text{Hg}_{1-x}\text{Cd}_x\text{Se}$ and $\text{Hg}_{1-x}\text{Cd}_x\text{Te}$ systems is shown in Figure 2 where the plot for the wurtzite phase of $\text{Hg}_{1-x}\text{Cd}_x\text{Se}$ is of $\sqrt{2}a$ because this quantity is directly comparable with the cubic lattice constant, a_0 . The lesser dependence on x of the lattice constant of $\text{Hg}_{1-x}\text{Cd}_x\text{Se}$ alloys compared with the $\text{Hg}_{1-x}\text{Cd}_x\text{Te}$ alloys could cause important differences between the two alloy systems in their crystal-growth behavior and lattice vibrational spectra.

2.2 Energy Band Structure of $\text{Hg}_{1-x}\text{Cd}_x\text{Se}$ Alloys

The mercury-cadmium-selenide alloys can be considered as pseudobinary alloys of HgSe and CdSe. The composition of a particular alloy is specified by the mole fraction of CdSe, x , and the stoichiometric formula is $\text{Hg}_{1-x}\text{Cd}_x\text{Se}$. The compound HgSe has an inverted electron-energy-band structure relative to that of CdSe, so that HgSe is referred to as a semiconductor with a "negative" energy-band gap. When an alloy between CdSe and HgSe is grown as a homogeneous single crystal, the electron-energy band-gap of the alloy is intermediate to the positive gap of CdSe and the negative gap of HgSe. The band-gap magnitude varies with the mole fraction of CdSe, x , in the alloy. This variability

of the semiconductor band-gap with composition is shown schematically in Figure 3.

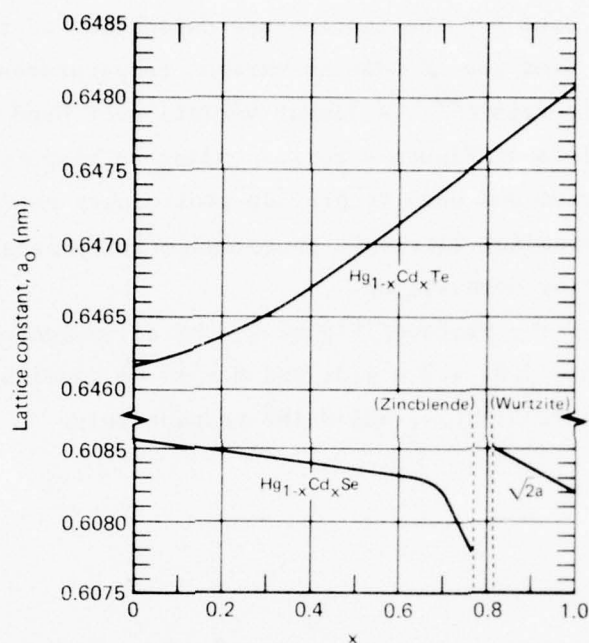


Figure 2 Variation of cubic unit-cell lattice-constant with x in the $\text{Hg}_{1-x}\text{Cd}_x\text{Se}$ and $\text{Hg}_{1-x}\text{Cd}_x\text{Te}$ alloy systems; for the $\text{Hg}_{1-x}\text{Cd}_x\text{Se}$ alloys with $x > 0.81$, $\sqrt{2}a$ is plotted where a is the hexagonal unit-cell edge

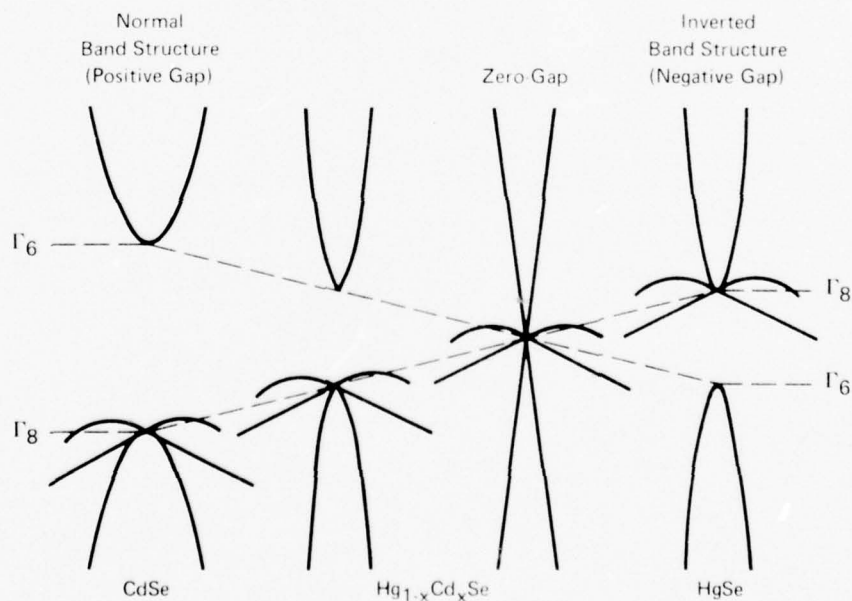


Figure 3 Transition from positive to negative band-gap in the $\text{Hg}_{1-x}\text{Cd}_x\text{Se}$ system as x decreases

2.3 Estimated Variation of Band Gap with Composition

The band gap of a specific composition of $\text{Hg}_{1-x}\text{Cd}_x\text{Se}$ alloy also significantly depends upon temperature. The results of Lehoczky, Broerman, Nelson, and Whitsett⁹ were used for the temperature dependence of the band gap in pure HgSe, and the band gap of CdSe at various temperatures was estimated from data in the literature¹⁰. A linear variation of band gap with x was assumed, and the plots of Figure 4 corresponding to temperatures of 77 and 300 K were constructed and used to provide preliminary estimates of the band gaps and the corresponding intrinsic photoconductivity wavelength-limits as functions of the alloy composition.

On the basis of the plots of Figure 4, the alloy compositions suitable at 77 K for the 2.5 - 2.8, 4.2 - 4.5, and 8 - 14 μm wavelength regions were estimated to be $x = 0.33$, 0.24, and 0.16, respectively.

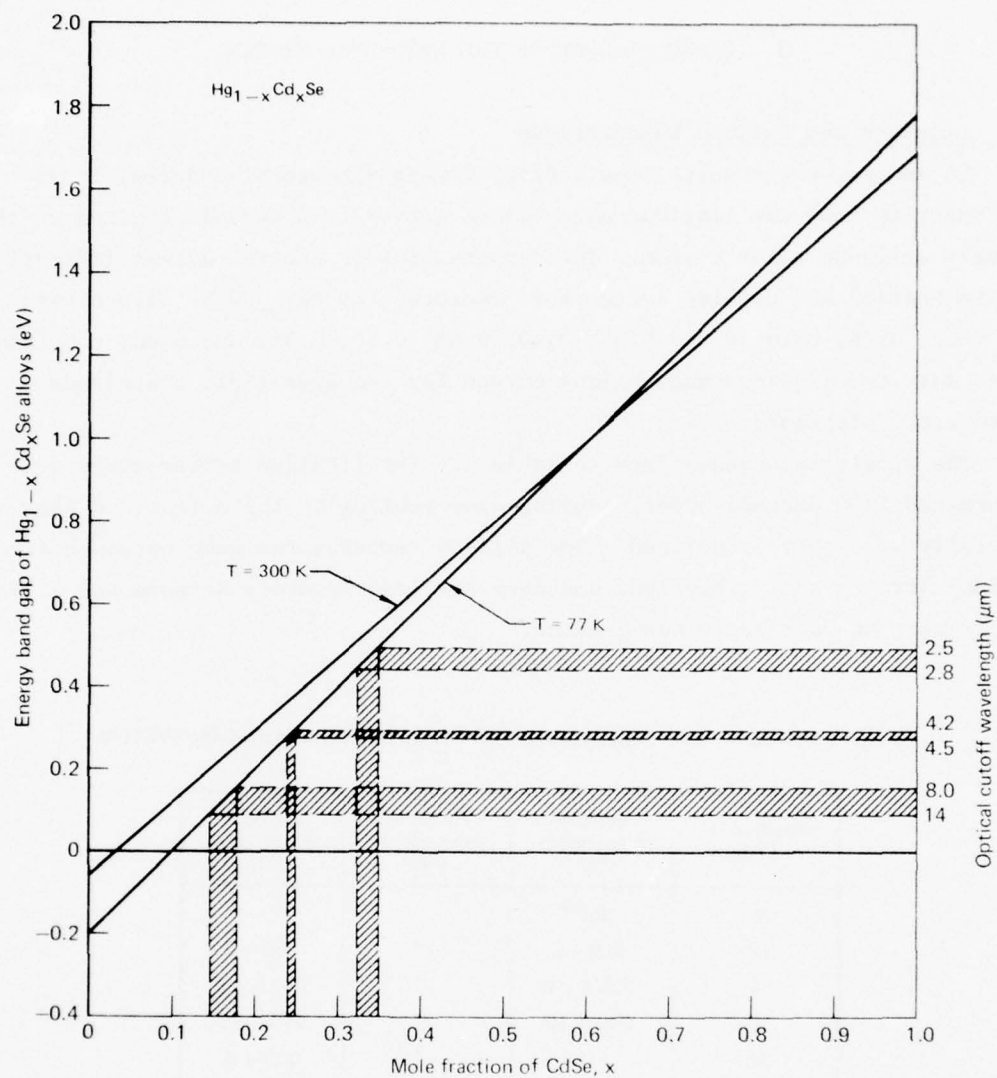


Figure 4. Estimated dependences of the energy-band gap on x for $\text{Hg}_{1-x}\text{Cd}_x\text{Se}$ alloys at 77 and 300 K

3. PHASE DIAGRAM OF THE HgSe-CdSe SYSTEM

3.1 Liquidus and Solidus Temperatures

To analyze the results of different crystal-growth procedures, it is necessary to know the liquidus and solidus curves over certain regions of the ternary Hg-Cd-Se alloy system. The temperatures of thermal-arrest inflections in the heating and cooling curves were measured for $\text{Hg}_{1-x}\text{Cd}_x\text{Se}$ alloys with $x = 0.12, 0.16, 0.20, 0.24, 0.33, 0.40, 0.45, 0.50, 0.55$, and 0.60 , and from these data the liquidus and solidus curves for the HgSe-rich, zincblende phase were determined.

The results are summarized in Table 1. The liquidus temperatures were determined from thermal arrests during slow cooling of the melts, and they generally were sharply defined. The solidus temperatures were obtained from thermal arrests during heating, and they are less accurate because the solid alloys were not perfectly homogeneous.

TABLE 1 PHASE-DIAGRAM DATA FOR THE PSEUDOBINARY HgSe-CdSe SYSTEM

Mole fraction of CdSe, x	Solidus temperature (°C)	Peritectic temperature (°C)	Liquidus temperature (°C)
0	799 ^(a)	—	—
12	815 ± 8	—*	860 ± 8
16	835.5 ± 6	—*	890.5 ± 6
20	840 ± 10	—*	910.6 ± 5
24	—*	—*	928 ± 6
33	858 ± 12	948 ± 5	972 ± 6
40	890 ± 10	951 ± 5	1006 ± 7
45	—†	947 ± 3	1032 ± 4
50	924 ± 8	943 ± 4	1053 ± 5
55	945 ± 8	949 ± 4	1079 ± 5
60	977 ± 12	—*	1093 ± 7
100	1239 ^(b)	—	—

(a) Reference 13

(b) Reference 14

*None observed

†Capsule exploded before completion of study

The tips first to freeze from melts with $x = 0.16, 0.24, 0.28, 0.33,$ and 0.40 had the compositions given in Table 2. The compositions of the crystal tips were calculated from their measured mass densities, and they should be the solidus compositions corresponding to melt liquidus temperatures. Because the tips may not have been homogeneous, the compositions listed in Table 2 represent minimum values. Inasmuch as the solidus temperatures in Table 1 should also be minimum values, the true solidus curve for the HgSe-CdSe system should lie between a curve constructed from the data of Table 1 and one constructed from the data of Table 2.

TABLE 2 COMPOSITIONS OF SOLIDS TO FIRST FREEZE FROM DIFFERENT
Hg_{1-x}Cd_xSe MELTS

Mole fraction of CdSe, x , in melt	Liquidus temperature of melt (°C)	Mole fraction of CdSe, x , in solid
0.16	885	0.31
0.24	928	0.46
0.28	950	0.54
0.33	972	0.60
0.40	1006	0.69

The solidus and liquidus points from Tables 1 and 2 were used to construct the phase diagram shown in Figure 5. This HgSe-CdSe phase diagram is not conventional because it does not represent phase equilibria at a constant pressure but, rather, at different pressures determined by the solid-liquid-vapor equilibrium for each alloy composition. The solidus curve shown in Figure 5 may shift significantly as a function of pressure, but as with the HgTe-CdTe system^{11,12}, the liquidus curve is not expected to be markedly dependent on pressure.

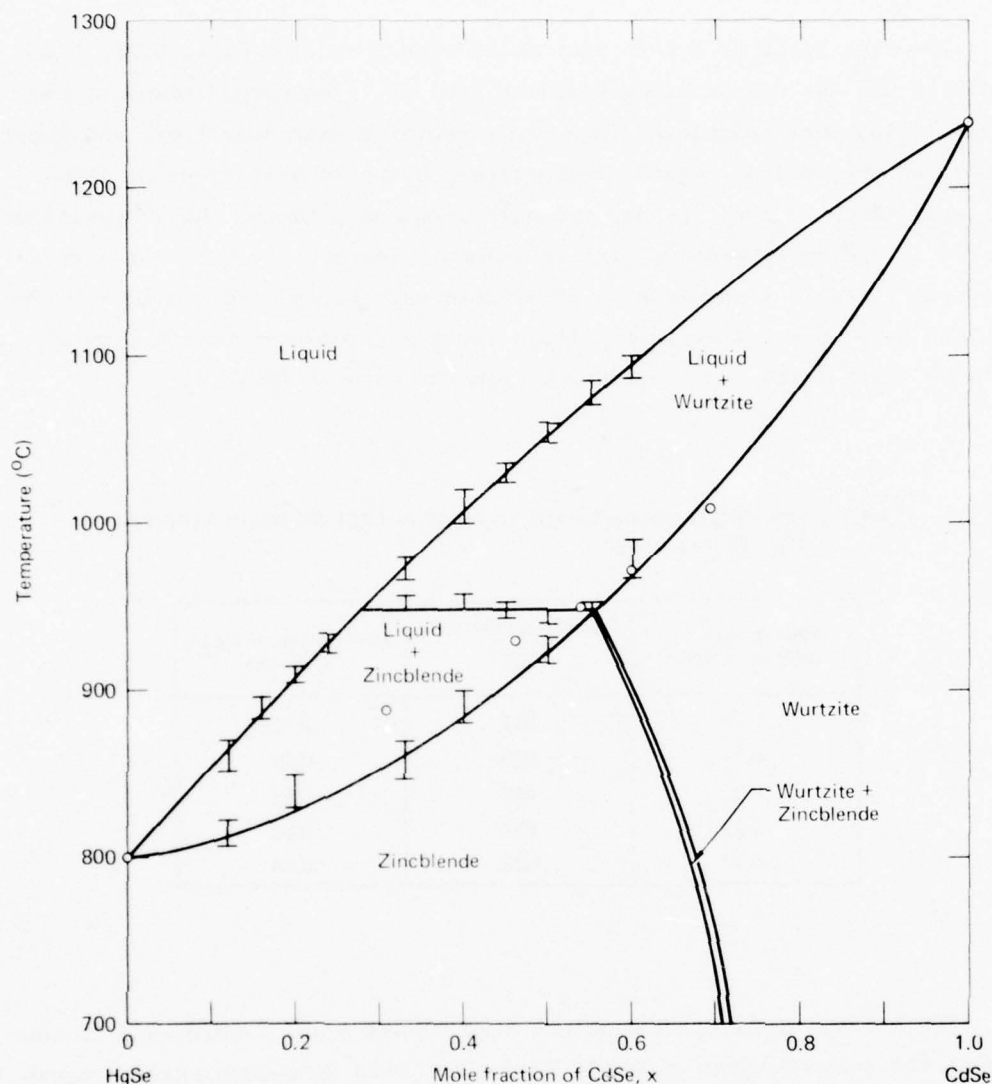


Figure 5. Pseudobinary HgSe-CdSe phase diagram; error bars are for thermal-arrest data points from Table 1; open circles are solid-composition data from Table 2

3.2 Peritectic Reaction and Miscibility Gap Between Crystallographic Phases

The data for alloys that had x -values between 0.33 and 0.50 establish the existence of a peritectic reaction at $947 \pm 4.0^\circ\text{C}$. Below this peritectic temperature, the solid in equilibrium with liquid has the zincblende crystal structure; above the peritectic temperature, the solid phase has the wurtzite crystal structure. The region of immiscibility of the zincblende

and wurtzite solid phases indicated in Figure 5 is speculative, although Kalb and Leute⁴ established that the miscibility gap at 0°C extends from $x = 0.77$ to $x = 0.81$.

The existence of a peritectic reaction and solid-miscibility gap between the zincblende and wurtzite phases does not perceptibly perturb the liquidus and solidus curves, which vary smoothly between the endpoint compositions of HgSe and CdSe. The wurtzite crystal structure forms only for x values higher than those of importance for infrared detector applications.

3.3 Theoretical Analysis of Binary-Alloy Phase Diagram

For two components, A and B, which are miscible in all proportions, the phase diagram is qualitatively as depicted in Figure 6. The melting temperatures of the pure components, A and B, are denoted by T_A and T_B , respectively, where $T_A < T_B$.

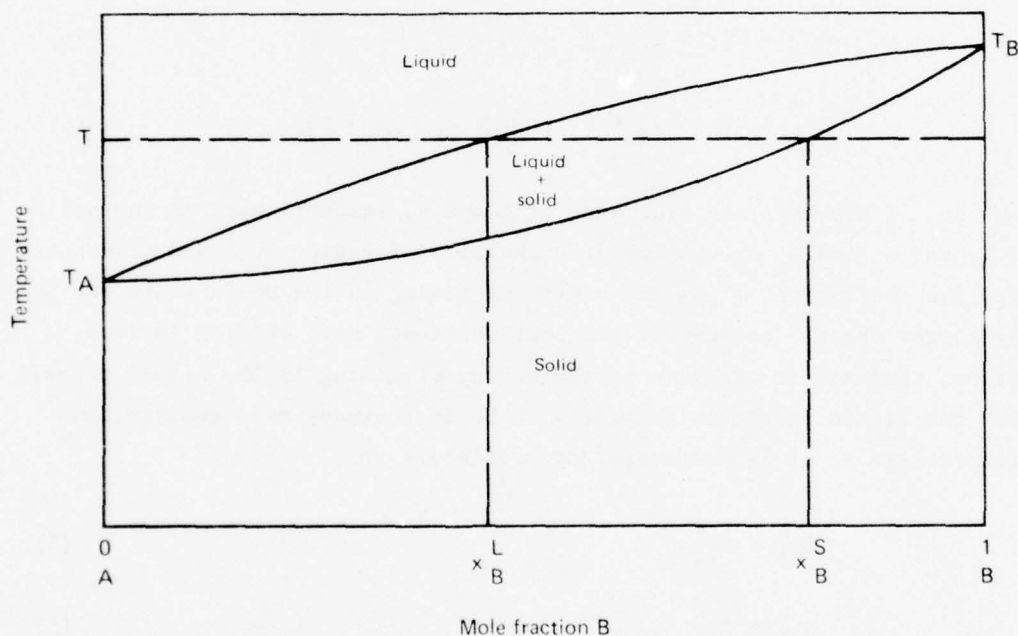


Figure 6 Phase diagram for homogeneous, monotonic, binary-alloy system

The changes in the chemical potentials of the two components resulting from mixing in the liquid are for A and B, respectively,

$$\Delta\mu_A^L = RT \ln x_A^L + B^L (x_B^L)^2 \quad (1)$$

and

$$\Delta\mu_B^L = RT \ln x_B^L + B^L (x_A^L)^2, \quad (2)$$

where R is the molar gas constant, T is the thermodynamic temperature, and x_A^L and x_B^L are the mole fractions of A and B in the liquid. The coefficient B^L is the energy of mixing that results from the reforming of chemical bonds and van der Waals forces between neighboring atoms; for an "ideal liquid", $B^L = 0$.

The changes in the chemical potentials upon mixing the components A and B in the solid are, respectively,

$$\Delta\mu_A^S = RT \ln x_A^S + B^S (x_B^S)^2 + L_A \left(\frac{T}{T_A} - 1 \right) \quad (3)$$

and

$$\Delta\mu_B^S = RT \ln x_B^S + B^S (x_A^S)^2 + L_B \left(\frac{T}{T_B} - 1 \right), \quad (4)$$

where x_A^S and x_B^S are the mole fractions of A and B, respectively, in the solid solution, and L_A and L_B are the molar enthalpies of fusion of A and B, respectively. The coefficient B^S is the energy of mixing in the solid state and is usually larger than B^L because it has contributions, such as from lattice distortion, that are in addition to the energy of mixing in the liquid phase.

For the liquid and solid solutions to be in thermodynamic equilibrium at a temperature T, it is necessary and sufficient that

$$\Delta\mu_A^L = \Delta\mu_A^S \quad (5)$$

and

$$\Delta\mu_B^L = \Delta\mu_B^S. \quad (6)$$

If Equations (1-4) are substituted into Equations (5) and (6) and the substitutions, $x_A^L = 1 - x_B^L$ and $x_A^S = 1 - x_B^S$, are made, the following expressions are obtained:

$$RT \ln(1 - x_B^L) + B^L (x_B^L)^2 = RT \ln(1 - x_B^S) + B^S (x_B^S)^2 + L_A(T - T_A)/T_A \quad (7)$$

and

$$RT \ln x_B^L + B^L (1 - x_B^L)^2 = RT \ln x_B^S + B^S (1 - x_B^S)^2 + L_B(T - T_B)/T_B. \quad (8)$$

If B^L , B^S , L_A , L_B , T_A , and T_B are known, Equations (7) and (8) can be solved simultaneously for the equilibrium values of x_B^L and x_B^S at each temperature.

Equations (7) and (8) can be solved for B^L and B^S ; the solutions are:

$$B^L = \frac{RT(1-x_B^S)^2 \ln \left[\frac{1-x_B^L}{1-x_B^S} \right] - (x_B^S)^2 \ln(x_B^L/x_B^S)}{(x_B^S)^2 (1-x_B^L)^2 - (x_B^L)^2 (1-x_B^S)^2} - \frac{(1-x_B^S)^2 L_A(T-T_A)/T_A - (x_B^S)^2 L_B(T-T_B)/T_B}{(x_B^S)^2 (1-x_B^L)^2 - (x_B^L)^2 (1-x_B^S)^2} \quad (9)$$

and

$$B^S = \frac{RT(1-x_B^L)^2 \ln \left[\frac{1-x_B^S}{1-x_B^L} \right] - (x_B^L)^2 \ln(x_B^S/x_B^L)}{(x_B^L)^2 (1-x_B^S)^2 - (x_B^S)^2 (1-x_B^L)^2} + \frac{(1-x_B^L)^2 L_A(T-T_A)/T_A - (x_B^L)^2 L_B(T-T_B)/T_B}{(x_B^L)^2 (1-x_B^S)^2 - (x_B^S)^2 (1-x_B^L)^2} \quad (10)$$

Values for x_B^L and x_B^S were taken from the experimental phase diagram (Figure 5) and used in Equations (9) and (10) to calculate B^L and B^S for the HgSe-CdSe alloy system. The following values were used: $T_A = 1072$ K (melting temperature of HgSe¹³); $T_B = 1512$ K (melting temperature of CdSe¹⁴); $L_A = 30.7$ kJ/mol (enthalpy of fusion for HgSe¹⁵); and $L_B = 43.9$ kJ/mol (enthalpy of fusion for CdSe¹⁶). The values of B^L and B^S required for the best fit to the experimental data are given by the relations

$$B^L/RT = -0.324 \quad (11)$$

and

$$B^S/RT = -0.00572. \quad (12)$$

The low value obtained for B^S/RT implies that the HgSe-CdSe solid solutions are nearly ideal. Because all the experimental data can be fitted to within

experimental error by one value of B^S/RT , both the zincblende and wurtzite structures have nearly equal energies of mixing. The fits to the experimental data afforded by the B^L/RT and B^S/RT values given in Equations (11) and (12) are shown in Figure 7.

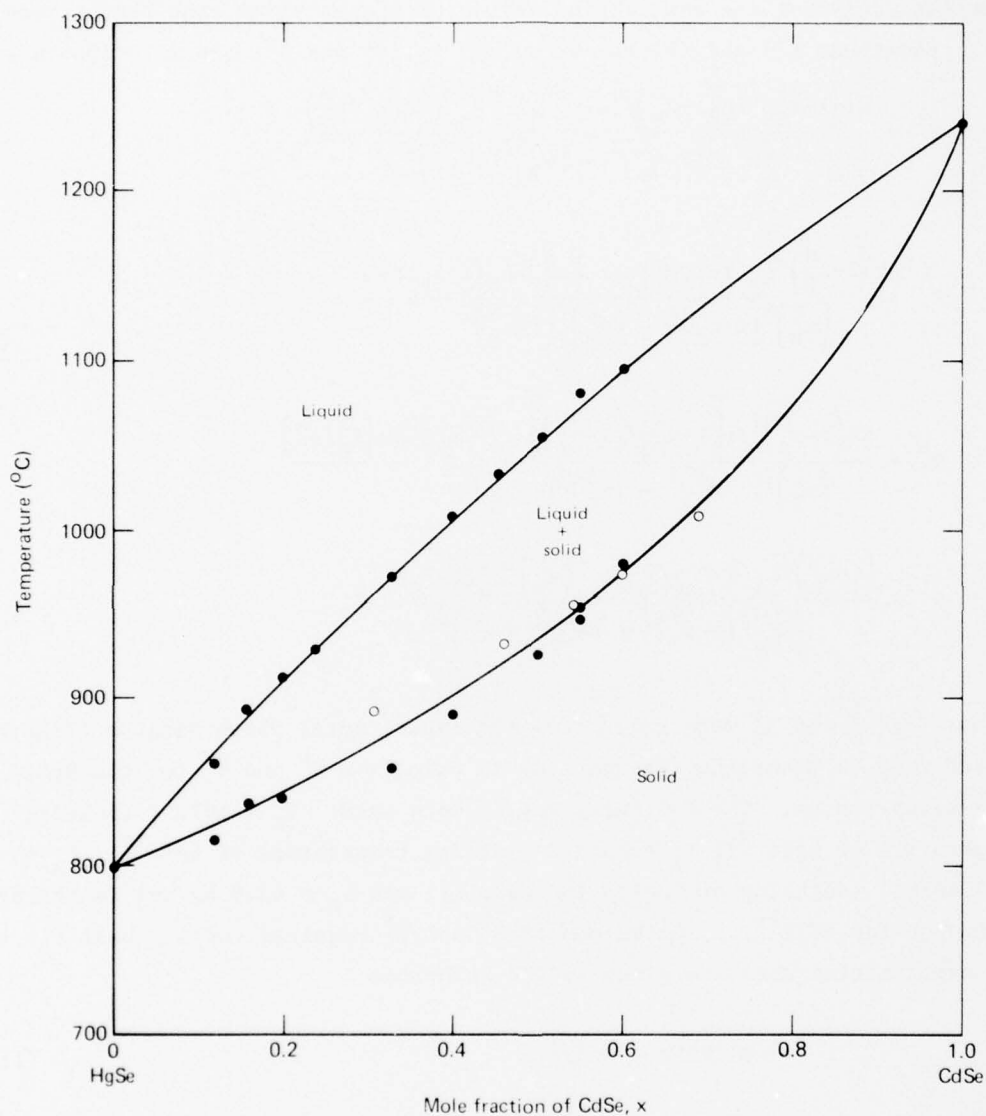


Figure 7. Calculated liquidus and solidus curves and experimental points for the HgSe-CdSe system; the interaction parameters used for the calculation are $B_L/RT = -0.324$ for the liquidus curve and $B_S/RT = -0.00572$ for the solidus curve, (●) data points from Table 1; (○) data points from Table 2

3.4 Experimental Method for Determining Thermal Arrests

The thermal arrest experiments involved sealing the HgSe-CdSe alloy in one quartz capsule and an equal number of moles of pure antimony in another, identical quartz capsule. The method used to prepare the HgSe-CdSe alloys was the same as that described in Section 4.1. A Chromel-P/Alumel thermocouple was used to measure the temperature of the HgSe-CdSe alloy, and a Chromel-P/Alumel differential thermocouple was used to measure the difference in temperature between the alloy and the antimony. The HgSe-CdSe alloy temperature was monitored on the x-axis of an x-y recorder, and the differential temperature was monitored on the y-axis. During heating or cooling of the capsules at a constant rate, the differential temperature was constant and proportional to the difference in specific heats of the HgSe-CdSe alloy and the antimony, except when the latent heats of phase transitions caused the differential temperature to change abruptly. Use of the antimony reference capsule provided a thermocouple calibration check at 651°C, the melting temperature of Sb¹⁷, for each heating and cooling curve.

The first experiments were conducted with a tube furnace that had external shunt taps for adjusting the current through various sections of its windings to obtain a flat temperature profile. However, temperature differences of a few degrees were unavoidable over the region of the furnace enclosing the HgSe-CdSe alloy and the Sb reference, and this limited the accuracy of the thermal-arrest temperature determination. The use of a sodium-vapor, isothermal, furnace liner within the tubular furnace reduced the undesired temperature gradients to negligible values, less than 0.01°C over the 46 cm length of the isothermal liner. The experimental arrangement with the isothermal liner is shown in Figure 8.

It is conventional to use reentrant capsules, with thermocouples inserted into the reentrant well, for measuring the thermal arrests of alloys. This was tried originally, but the reentrant quartz capsules did not withstand the high vapor pressures over HgSe-CdSe melts at temperatures $\geq 1000^\circ\text{C}$. Furthermore, because some of the thermal arrest experiments involved keeping the melts at high temperatures for many days, devitrification of the quartz capsules was an occasional problem. The quartz capsules were 5 mm i.d. x 12 mm o.d. x 7.5 cm long. These capsules occasionally ruptured after prolonged periods at 1100°C and higher temperatures, but they generally were adequate for all alloy compositions with $x \leq 0.6$. The capsules contained

a sufficient amount of alloy, 10.0 g, to show well-defined thermal arrests. During the study of the HgSe-CdSe phase diagram, the abruptness and the precise temperature of thermal arrests during heating were observed to depend on the previous thermal history of the alloy ingot. To obtain well-defined arrests during heating, it proved necessary to prepare alloy ingots by rapidly quenching homogeneous melts at a rate $\approx 450^{\circ}\text{C}/\text{min}$ and to homogenize the quenched alloys by annealing them for 50 h at temperatures 30°C below their solidus temperatures.

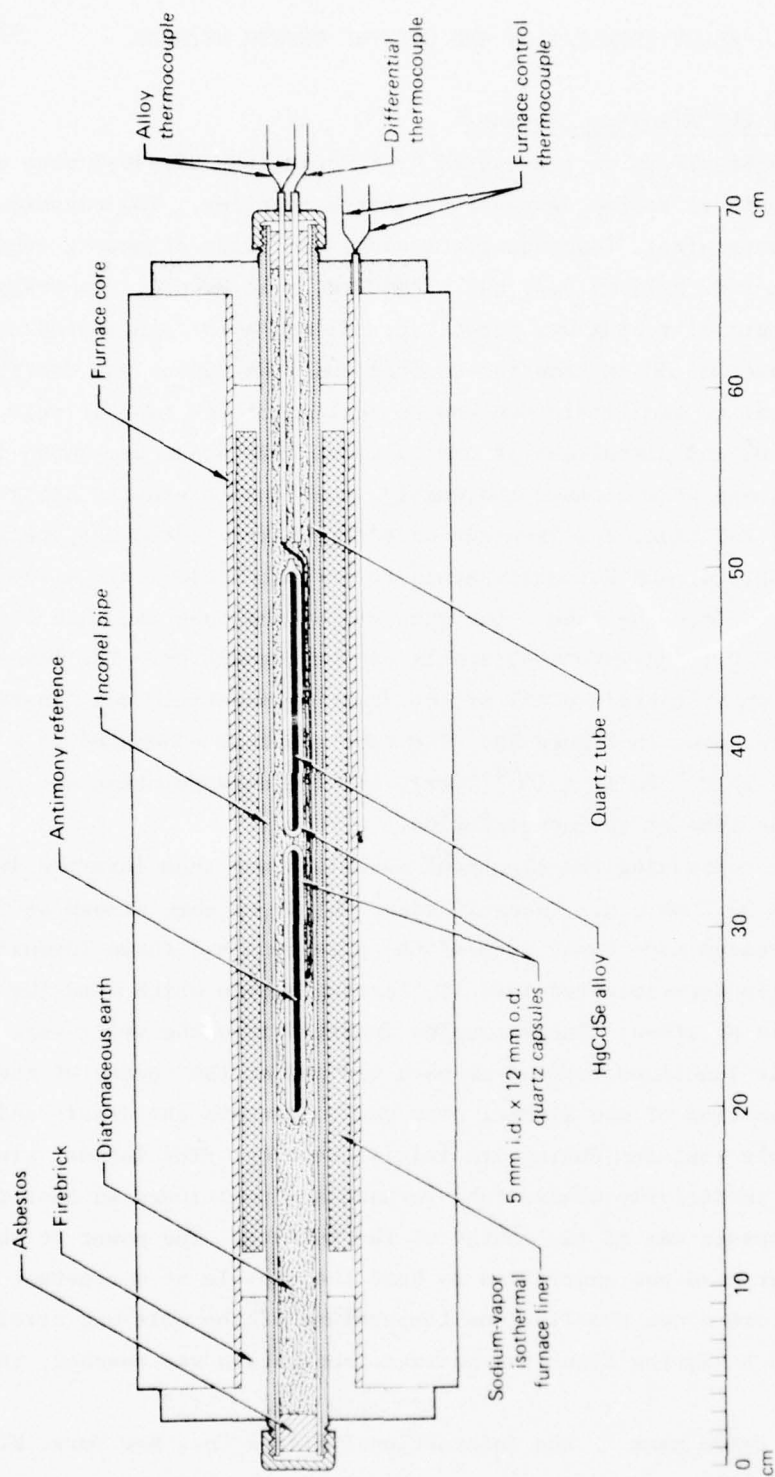


Figure 8 Experimental arrangement for determining thermal-arrest temperatures during heating and cooling of HgSe-CdSe alloys

4. ALLOY PREPARATION AND CRYSTAL GROWTH METHODS

4.1 Reaction of the Alloying Elements

The $\text{Hg}_{1-x}\text{Cd}_x\text{Se}$ alloys were prepared by reacting the 99.9999% pure elemental constituents in sealed, evacuated, quartz capsules. The capsules were made from water-free, fused-quartz tubing; two sizes of quartz tubing were used, 10 mm i.d. x 20 mm o.d. and 12 mm i.d. x 18 mm o.d. To prepare a capsule, a length of tubing was first tapered to a point and sealed at one end. At a distance of 30 cm from the tapered end, the tubing was constricted to about 5 mm i.d. to facilitate subsequent sealing of the tube at this point. The shapes and dimensions of the tubes at this stage are shown in Figure 9. The tubes were cleaned thoroughly, the final cleansing being done with a dilute HF solution, and then evacuated and baked. Precisely weighed amounts of the Hg, Cd, and Se constituents to form stoichiometric alloys were then inserted into the tube. The open end of the tube was then inserted through an O-ring fitting into a rotatable vacuum connection. The lower 25 cm of the tube, which contained all of the starting material, was immersed in an ice bath as shown in Figure 10. The tube was then evacuated to a pressure less than 1×10^{-4} Pa (1×10^{-6} Torr), and the encapsulation was completed by sealing the tube at the constriction.

The capsule containing the elemental materials was then inserted into a 50.8 mm i.d. x 57.2 mm o.d. Inconel* tube, which was then closed at both ends by threaded pipe caps. One of the pipe caps had three Inconel thermocouple-wells hard-soldered into it, forming a cage which held the quartz capsule in position. Thermocouples inserted into the wells were positioned with their junctions located at each end and at the center of the capsule. The function of the Inconel pipe was to contain the debris and vapor if a capsule ruptured during its initial heating. The Inconel pipe was placed in a resistively-heated tube-furnace and positioned so that the loaded quartz capsule was at the center of the furnace. The power to the furnace was programmed and controlled to heat the capsule at a constant rate until a temperature above the liquidus temperature of the melt was attained. During the 24-28 h heating after the maximum temperature was reached, the

*Inconel is the trade name of the International Nickel Co., New York, N.Y., for Ni-13Cr-10Fe alloy.

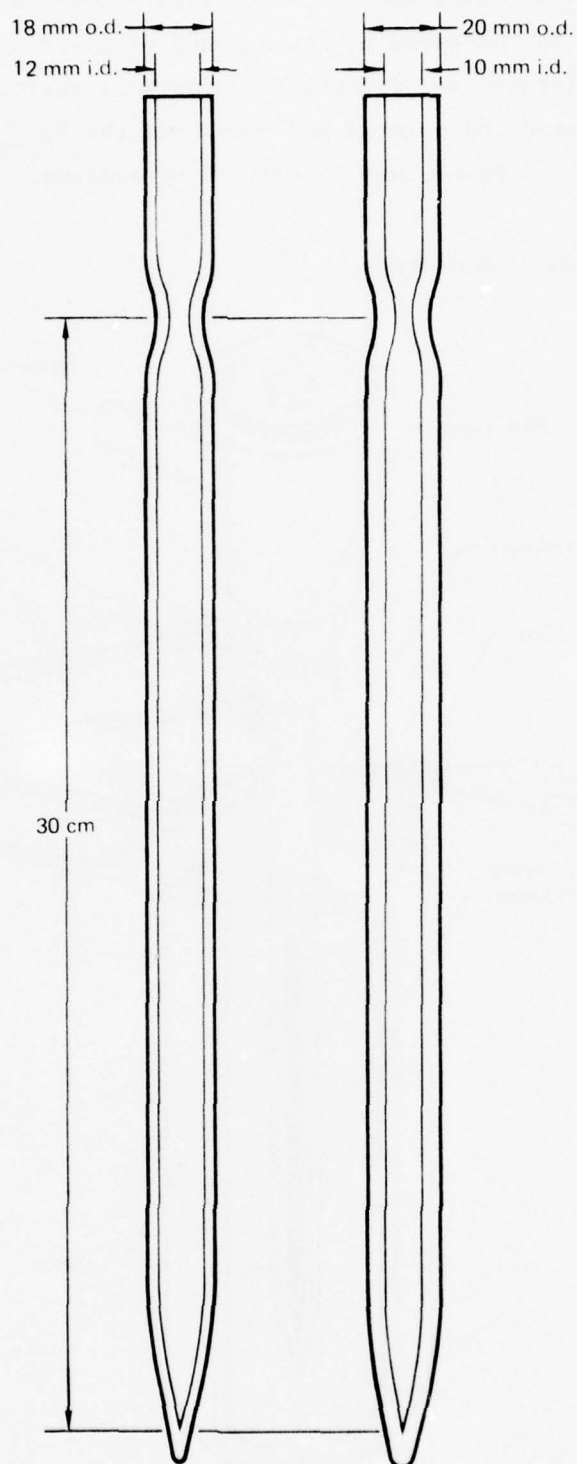


Figure 9 Dimensions of quartz tubes used for $\text{Hg}_{1-x}\text{Cd}_x\text{Se}$ alloy preparations

furnace was rocked $\pm 45^\circ$ back and forth to agitate and thereby homogenize the molten material in the capsule. At the end of 24-28 h at maximum temperature, the rocking furnace was rotated to a vertical position so that the capsule had its tapered and pointed end down, and the $\text{Hg}_{1-x}\text{Cd}_x\text{Se}$ alloy, which half-filled the capsule, was solidified by cooling.

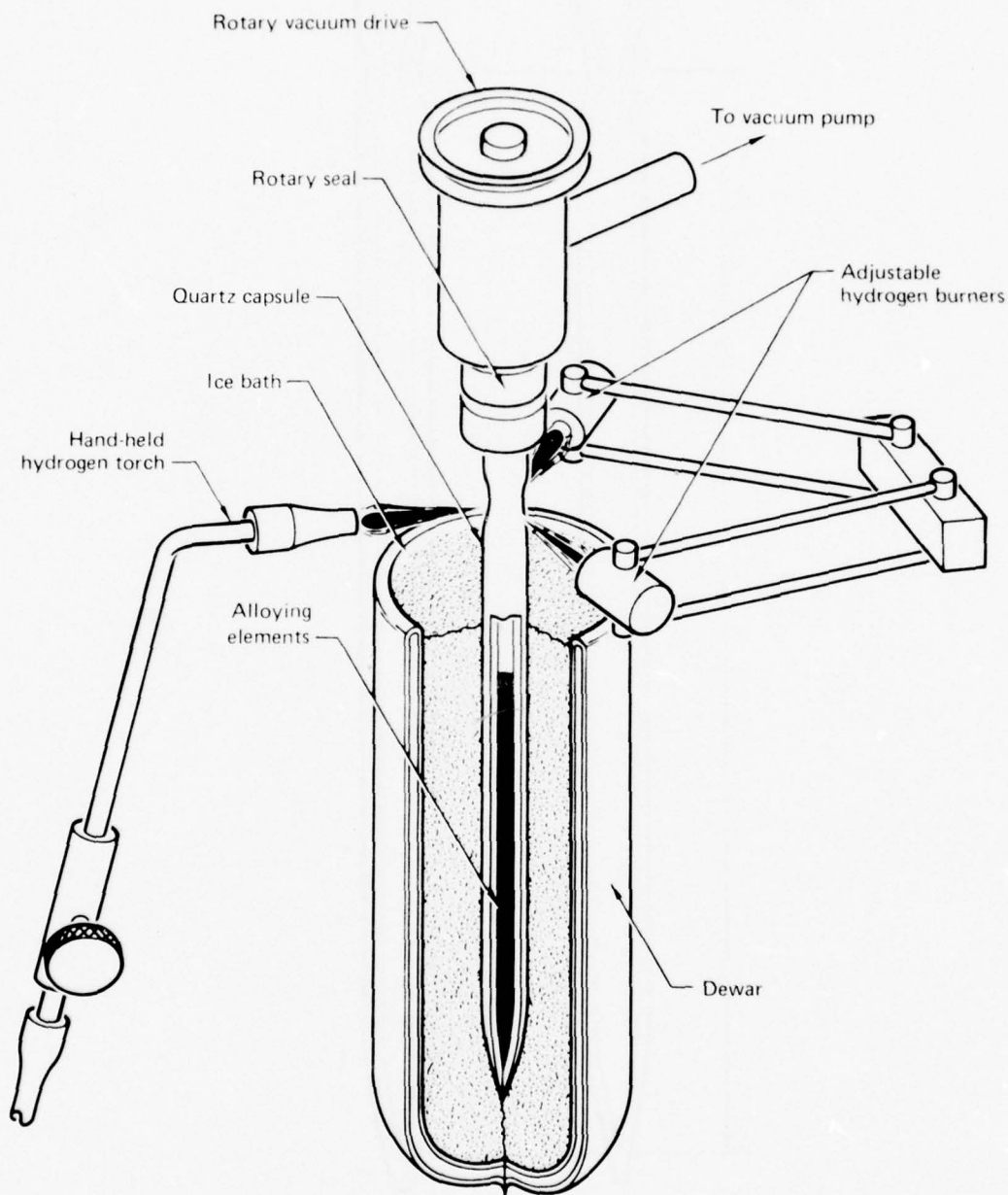


Figure 10 Experimental arrangement for evacuating and sealing quartz tubes containing the alloying elements for preparation of $\text{Hg}_{1-x}\text{Cd}_x\text{Se}$ alloys

4.2 Single-Crystal Growth by the Bridgman Method

The alloy in the quartz capsule is recrystallized by the Bridgman method for growing single crystals. The Bridgman apparatus is shown in Figure 11. The capsule is mounted, with its tapered end down, atop a quartz pedestal and remains stationary during the recrystallization. The furnace travels upward on vertical ways so that the alloy recrystallizes progressively upward from the bottom, tapered end of the quartz capsule. The Bridgman furnace is a resistively-heated, three-zone, tubular furnace, and each of the 30 cm long zones is separately controllable. The center zone has shunt-taps at 25 mm intervals, and the two end-zones have shunt-taps at 50 mm intervals. By placing appropriate shunt resistances between these taps, the axial temperature profile of the furnace can be shaped as required. The entire center zone is so shunted that its axial temperature is within $\pm 2^\circ\text{C}$ of a mean value. The shunting of the lower end-zone is adjusted to provide a sharp temperature gradient between this zone and the center zone. The furnace raising mechanism is driven by a variable-speed motor, and the furnace can be raised at any desired rate between 0.04 and 4.0 cm/h.

After it is recrystallized by the Bridgman method, the $\text{Hg}_{1-x}\text{Cd}_x\text{Se}$ alloy crystal is removed from the quartz capsule. This is accomplished by using a diamond-blade saw to cut longitudinal slots on opposite sides of the capsule. The two halves of the capsule then fall away from the enclosed crystalline ingot. The ingot is then "sand-blasted" with alumina powder of 15 μm particle size. This mechanical etching causes all but small-angle grain boundaries to be easily visible.

4.3 Capsule Rupture Problem

During several alloy preparations, the quartz capsules ruptured during the initial heating to react the alloying elements.

The quartz capsules were annealed at 1200°C for several hours and cooled slowly to room temperature before they were loaded with the alloying elements. After they were loaded, evacuated, and sealed, the quartz capsules were checked in polarized light for strains, and when necessary the capsules were hydrogen-flame annealed until they exhibited no strains.

An approach used to avoid capsule failure was to employ very slow capsule heating rates during the reaction process. Lengthy temperature soaks were also tried at 600° to 750°C before heating the capsules to the alloy liquidus temperatures. Using either method, the quartz capsules ruptured during the reaction process.

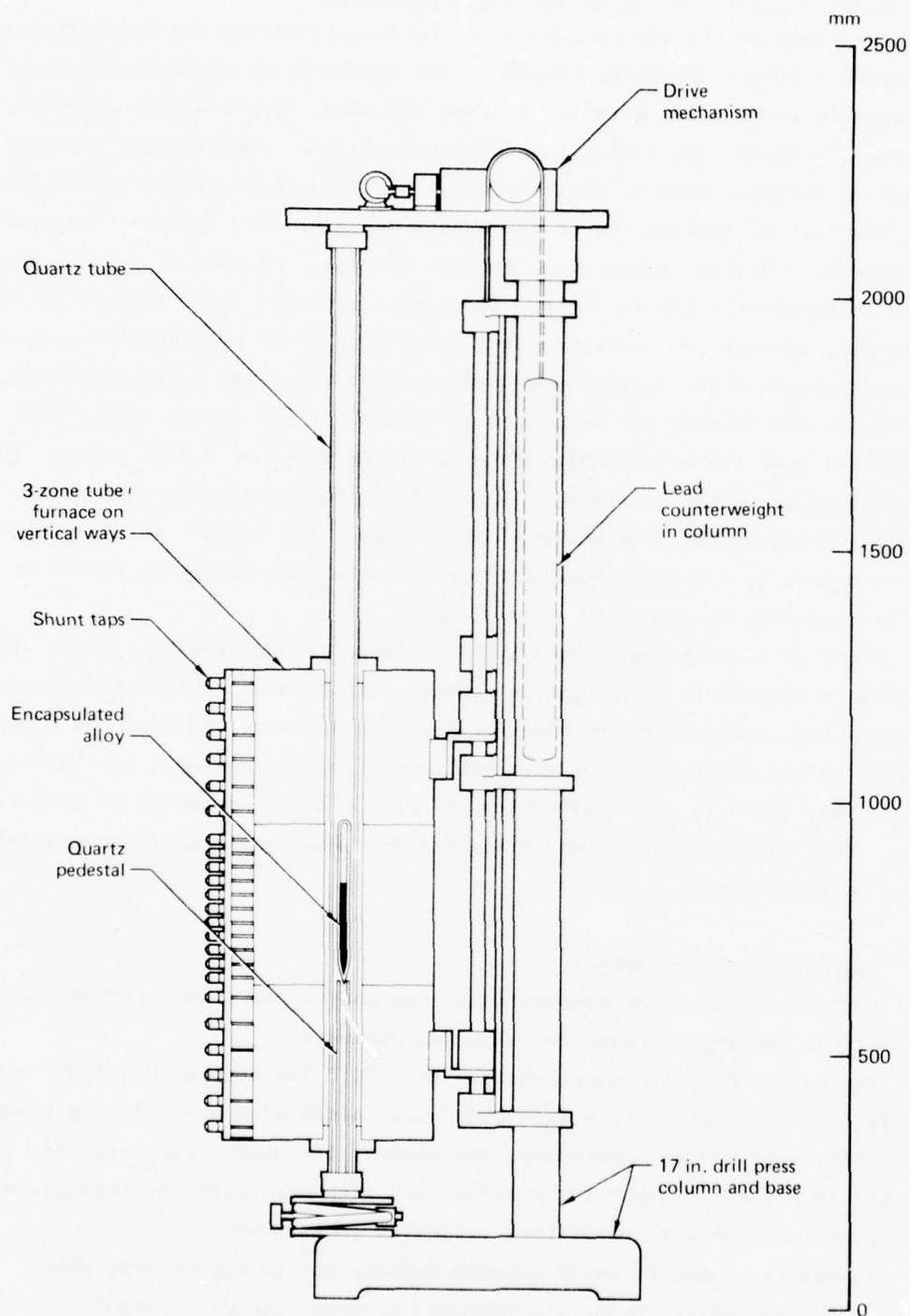


Figure 11 Apparatus for growing single crystals of $\text{Hg}_{1-x}\text{Cd}_x\text{Se}$ alloys by the Bridgman method

Initially, quartz tubing 12 mm i.d. x 18 mm o.d. was used successfully for the preparation of $\text{Hg}_{1-x}\text{Cd}_x\text{Se}$ alloys, but after several failures with this tubing, a thicker-wall quartz tubing, 10 mm i.d. x 20 mm o.d. was employed. A number of the thicker-wall quartz capsules failed also, but others served for successful preparations. Our conclusion is that the quartz capsule failures were caused by minute, random flaws in the quartz tubing. The quartz tubing was selected for concentricity of the inner and outer diameters, and tubing with visible striae or flaws was, of course, never used for preparing capsules. A method for determining the quality of a quartz tube before it is used for an alloy preparation was not evolved.

The quartz capsules that ruptured did so during the initial heating of the alloying elements and at temperatures well below the alloy liquidus temperatures. In every case, a rupture was immediately preceded by a sudden increase in the temperature of the reacting elements, presumably caused by the heat of reaction. In no case did a quartz capsule fail, even during subsequent temperature cycling, if its alloy contents were once melted and homogenized.

Consideration was given to placing the quartz capsule in a pressurized cylinder that could be inserted into the tube furnace. The pressure in the cylinder would reduce the pressure differential between the inside and the outside of the quartz capsule and thus reduce the likelihood of its rupture during the reaction of the elements to form the alloy. This scheme has merit but was not tried because of lack of time to develop a suitable design. Metal cylinders cannot be used because they have inadequate yield strengths at the melting temperatures of the $\text{Hg}_{1-x}\text{Cd}_x\text{Se}$ alloys. Refractory oxide cylinders have the required high strength at high temperatures, but they present fabrication problems. If the HgCdSe alloys were to be produced in quantity, a method utilizing refractory enclosures could significantly increase the yield.

4.4 Vapor Pressures within the Capsules

At the liquidus temperatures of the $\text{Hg}_{1-x}\text{Cd}_x\text{Se}$ alloys, from 799° to 1239°C, the Hg, Cd, and Se vapor pressures within the quartz capsules are quite high. If Raoult's Law is valid for the $\text{Hg}_{1-x}\text{Cd}_x\text{Se}$ alloys, and if it is assumed that Se exists as a dimer in the vapor phase, the elemental partial pressures are given by the relations

$$p_{\text{Hg}}^{\text{Hg}_{1-x}\text{Cd}_x\text{Se}} = (1-x)p_{\text{Hg}}^{\text{HgSe}}, \quad (13)$$

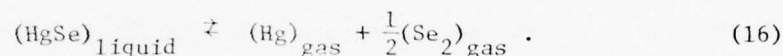
$$p_{\text{Cd}}^{\text{Hg}_{1-x}\text{Cd}_x\text{Se}} = x p_{\text{Cd}}^{\text{CdSe}}, \quad (14)$$

and

$$p_{\text{Se}}^{\text{Hg}_{1-x}\text{Cd}_x\text{Se}} = \frac{1-x}{2} p_{\text{Hg}}^{\text{HgSe}} + \frac{x}{2} p_{\text{Cd}}^{\text{CdSe}}, \quad (15)$$

where p_Y^X is the partial pressure of element Y in equilibrium with the alloy or compound X. $p_{\text{Hg}}^{\text{HgSe}}$ and $p_{\text{Cd}}^{\text{CdSe}}$ can be calculated from thermodynamic relations.

For the case of HgSe, consider that the reaction between compound and vapor is the following:



At equilibrium,

$$\left(p_{\text{Hg}}^{\text{HgSe}} \right) \left(p_{\text{Se}}^{\text{HgSe}} \right)^{1/2} = K^{\text{HgSe}}, \quad (17)$$

where K^{HgSe} is the thermodynamic equilibrium constant for the reaction. (The activities of Hg and Se are assumed to be equal to their partial pressures.) The value for K^{HgSe} can be calculated from the following expressions for the Gibbs energy for the reaction given by Equation (16).

$$\Delta G_{\text{HgSe}} = -RT \ln K^{\text{HgSe}} \quad (18)$$

and

$$\Delta G_{\text{HgSe}} = \Delta H_{\text{HgSe}} - T\Delta S_{\text{HgSe}}. \quad (19)$$

In these expressions, ΔH_{HgSe} is the enthalpy change and ΔS_{HgSe} is the entropy change upon forming liquid HgSe from the vapor phases of the constituent elements. The Gibbs energy of dissociation of solid HgSe¹⁹ is

$$\Delta G \left[(\text{HgSe})_{\text{solid}} \rightarrow (\text{Hg})_{\text{gas}} + \frac{1}{2}(\text{Se}_2)_{\text{gas}} \right] = (175.4 - 0.1774T) \text{ kJ/mol}. \quad (20)$$

If the heat of fusion of HgSe¹⁵, 30.7 kJ/mol, is subtracted from Equation (20), the result is

$$\Delta G_{\text{HgSe}} = 144.7 - 0.1774T \text{ kJ/mol}, \quad (21)$$

which can be substituted into Equation (18) to determine K^{HgSe} . Once K^{HgSe} is calculated for a given temperature, the partial pressures of Hg and Cd vapor in equilibrium with liquid HgSe can be calculated from the relations

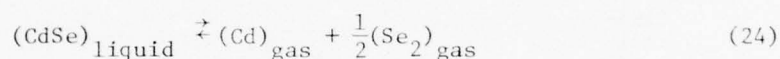
$$P_{\text{Hg}}^{\text{HgSe}} = 2^{1/3} \left(K^{\text{HgSe}} \right)^{2/3} \quad (22)$$

and

$$P_{\text{Se}}^{\text{HgSe}} = 2^{-2/3} \left(K^{\text{HgSe}} \right)^{2/3}. \quad (23)$$

Equations (22) and (23) are derived from Equation (17) and the condition that $d(P_{\text{Hg}}^{\text{HgSe}} + P_{\text{Se}}^{\text{HgSe}})/dP_{\text{He}}^{\text{HgSe}} = 0$.

The calculation for $P_{\text{Cd}}^{\text{CdSe}}$ and $P_{\text{Se}}^{\text{CdSe}}$ is similar to the HgSe calculation, and the key relationships for the reaction



are

$$\left(P_{\text{Cd}}^{\text{CdSe}} \right) \left(P_{\text{Se}}^{\text{CdSe}} \right) = K^{\text{CdSe}}, \quad (25)$$

$$\Delta G_{\text{HgSe}} = -RT \ln K^{\text{CdSe}}, \quad (26)$$

$$P_{\text{Cd}}^{\text{CdSe}} = 2^{1/3} \left(K^{\text{CdSe}} \right)^{2/3}, \quad (27)$$

and

$$P_{\text{Se}}^{\text{CdSe}} = 2^{-2/3} \left(K^{\text{CdSe}} \right)^{2/3}. \quad (28)$$

The Gibbs energy of dissociation of solid CdSe^{20} is

$$\Delta G \left[(\text{CdSe})_{\text{solid}} \longrightarrow (\text{Cd})_{\text{gas}} + \frac{1}{2}(\text{Se}_2)_{\text{gas}} \right] = (329.5 - 0.1997T) \text{ kJ/mol}, \quad (29)$$

and the heat of fusion of CdSe^{16} is 43.9 kJ/mol. Thus,

$$\Delta G_{\text{CdSe}} = (286 - 0.1997T) \text{ kJ/mol}.$$

The vapor pressures of Hg, Cd, and Se in equilibrium with $\text{Hg}_{1-x}\text{Cd}_x\text{Se}$ were calculated in accordance with the preceding formulation, and these partial pressures and their sum are plotted as functions of x in Figure 12. For the $\text{Hg}_{1-x}\text{Cd}_x\text{Se}$ alloy with the smallest x -value (0.16) prepared for this study, the pressure within the quartz capsule at the liquidus temperature

is 9 MPa (90 atm), and for the largest x-value (0.33), the pressure is 15 MPa (150 atm). The theoretical tensile strength of the 3-mm wall-thickness quartz capsules used for crystal growth is 10 MPa (100 atm) and that of the 5-mm wall thickness quartz capsules is 16 MPa (160 atm). Thus it is evident that the quartz tubing must be flawless to withstand the internal pressures generated by the stoichiometric alloys. The internal pressures could be significantly reduced if the melts contained excess Se, but the magnitude of the pressure reduction and the possible effect of excess Se upon crystal quality were not studied.

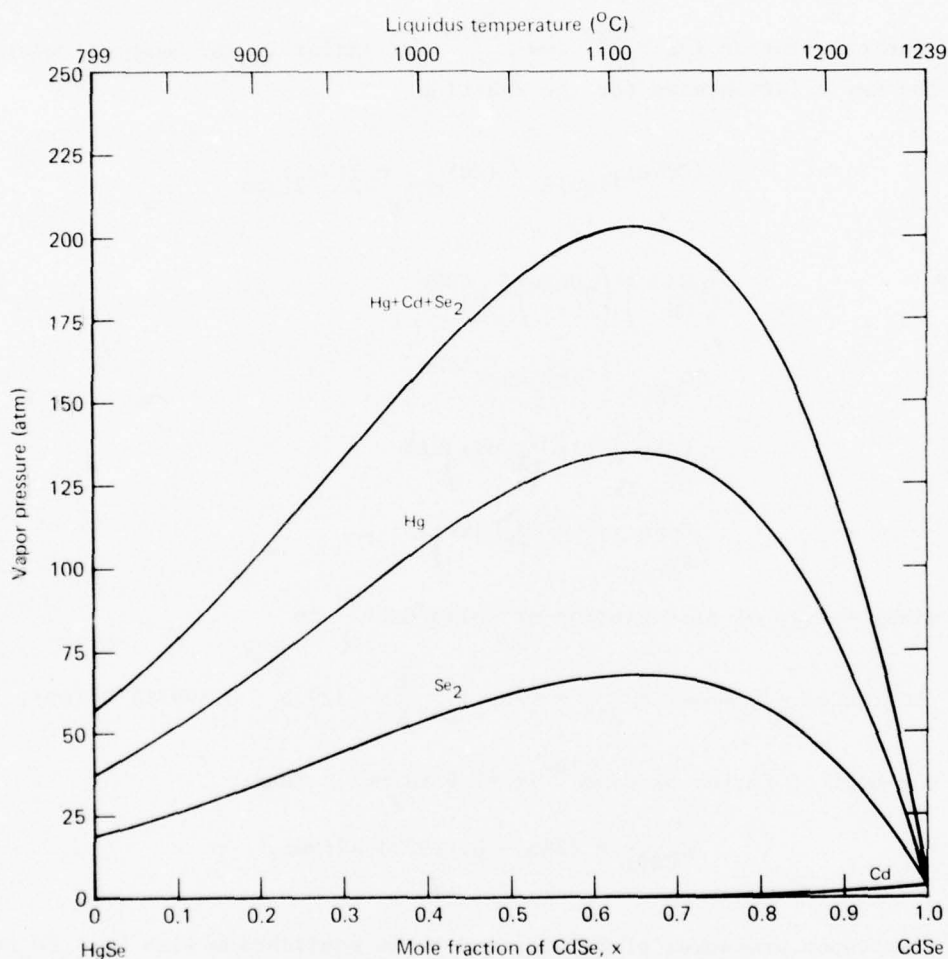


Figure 12 Partial pressures of vapor-phase Hg, Cd, and Se₂ and the total vapor pressure at equilibrium for Hg_{1-x}Cd_xSe alloys at their liquidus temperatures

5. CRYSTAL PREPARATIONS AND CHARACTERIZATION

5.1 Crystal Preparations

The alloy compositions prepared are summarized in Table 3. The alloy ingots are identified by a number that is the nominal x-value in hundredths and a letter that identifies different ingots that have the same composition. Four alloy ingots were prepared and recrystallized by the Bridgman method: 16D, 16E, 24A, and 33A.

TABLE 3 Hg_{1-x}Cd_xSe ALLOY PREPARATIONS IN CHRONOLOGICAL ORDER OF PROCESSING

Hg _{1-x} Cd _x Se ingot no.	Average x	Capsule i.d. x o.d. (mm)	Weight of Hg (g)	Weight of Cd (g)	Weight of Se (g)	Total weight (g)	Comments
16C	0.160	12 x 18	72.369	7.724	33.908	114.001	Heated at 480°C/h. Capsule ruptured at 450°C.
16A	0.160	12 x 18	72.370	7.724	33.908	114.002	Heated at 10°C/h. Capsule ruptured at 700°C.
16B	0.160	12 x 18	72.369	7.724	33.908	114.001	Not processed.
16D	0.160	10 x 20	50.787	5.420	23.796	80.003	Heated at 20°C/h to 925°C. Recrystallized by Bridgman method.
33A	0.330	10 x 20	42.928	11.847	25.217	79.992	Heated 600°C/h to 600°C, 10°C/h to 825°C; soaked 65h at 825°C; heated 10°C/h to 975°C. Recrystallized by Bridgman method.
16F	0.160	10 x 20	50.788	5.420	23.796	80.004	Heated 10°C/h. Capsule ruptured at 700°C.
16E	0.160	10 x 20	50.790	5.421	23.798	80.009	Heated 10°C/h to 925°C. Recrystallized by Bridgman method.
24A	0.240	10 x 20	47.201	8.352	24.444	79.997	Heated 600°C/h to 600°C, 10°C/h to 940°C. Recrystallized by Bridgman method.

Figures 13a, 13b, 13c, and 13d are photographs of the Bridgman-grown ingots 16D, 16E, 24A, and 33A respectively. HgCdSe 16D was grown at the rate of 0.50 cm/h through a temperature gradient of 13°C/cm; it had one transverse grain boundary 1.0 cm above the bottom tip where recrystallization commenced. HgCdSe 16E was grown at the slower rate of 0.04 cm/h through a gradient of 14°C/cm until approximately a 9 cm length had

crystallized and grown at 0.5 cm/h thereafter; it was a bicrystal from the bottom tip upward for 6.2 cm, single crystalline from 6.2 to 9.3 cm, and large grain polycrystalline from 9.3 cm for the remainder of its 14 cm length. HgCdSe 24A was recrystallized at the rate of 0.04 cm/h through a temperature gradient of 13°C/cm. Near the end of the growth of HgCdSe 24A, a furnace-control thermocouple failed, causing the furnace power to be turned off. HgCdSe 24A was a single crystal except for the last 1.4 cm of its length which was essentially quenched from the melt when the furnace power was turned off. After these crystals had been grown, the Bridgman crystal-growth furnace was improved by the addition of two sodium-vapor isothermal furnace-liners. The liners, each 30 cm long, are separated vertically by 1.5 mm within the furnace tube. The temperature of the region within each liner is uniform, and a 220°C temperature differential can be maintained between the two liners. The isothermal furnace liners reduce unwanted radial temperature gradients in the melt of alloys that are recrystallized by the Bridgman method and facilitate establishing steeper temperature gradients at the solid-melt interface during crystal growth. HgCdSe 33A was recrystallized by the Bridgman method at a rate of 0.030 cm/h through a temperature gradient of 35°C/cm. The temperature gradient was smaller than that between the isothermal liners because a 2.65 mm i.d. x 3.27 mm o.d. Inconel pipe was placed inside the liners to protect them from possible capsule explosions. The resultant crystal was single crystalline for a distance of approximately 10 cm from the bottom tip; because a power failure caused an abortion of the crystal growth, the upper 5-cm length of the ingot was quenched and is polycrystalline. During the preparation of this ingot, the melt wet the quartz at some spots, and the solidified ingot adhered to the quartz at these places. This made it necessary to fracture the ingot in several places to remove it from the quartz capsule. Several of the fracture surfaces are parallel to each other (those at 6.8, 7.4, and 8.7 cm) and perpendicular to the fracture running from 1.0 to 3.0 cm. This fracture pattern implies that the cleavage planes are $[100]$ and that the direction of crystal growth was $\langle 100 \rangle$.

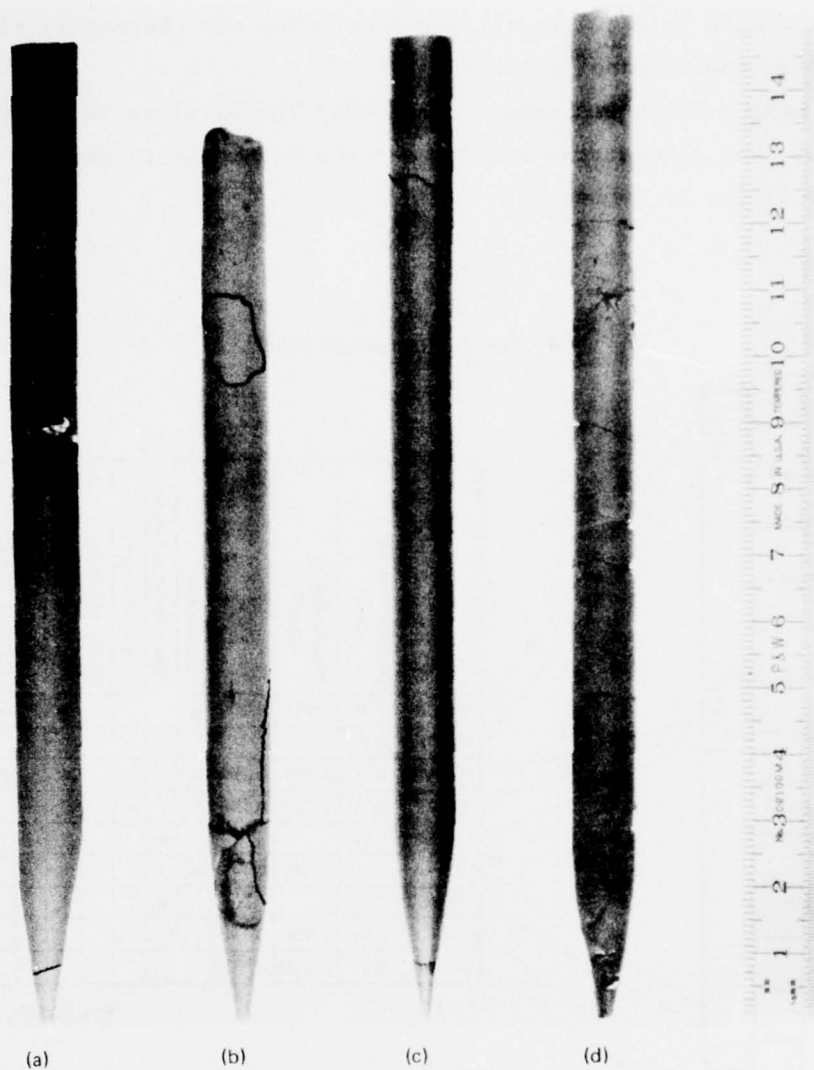


Figure 13 Photographs of $\text{Hg}_{1-x}\text{Cd}_x\text{Se}$ alloys recrystallized by the Bridgman method (a) 16D (b) 16E (c) 24A (d) 33A; white lines are boundaries between single crystalline regions except for the upper 2.5 cm of 24A and the upper 5 cm of 33A, which were quenched

A diamond-rim saw was used to slice each of the crystals into 0.5 to 2.0 mm thick sections. The slices are identified in Tables 4-7. Each slice was etched in a 10% Br₂-methanol solution and thoroughly rinsed in a 50% benzene-methanol solution.

The mass density was measured and used to calculate the average x-value of many slices; the results and the measurements made on each slice are listed in Tables 4-7.

TABLE 4. HgCdSe 16D SAMPLES

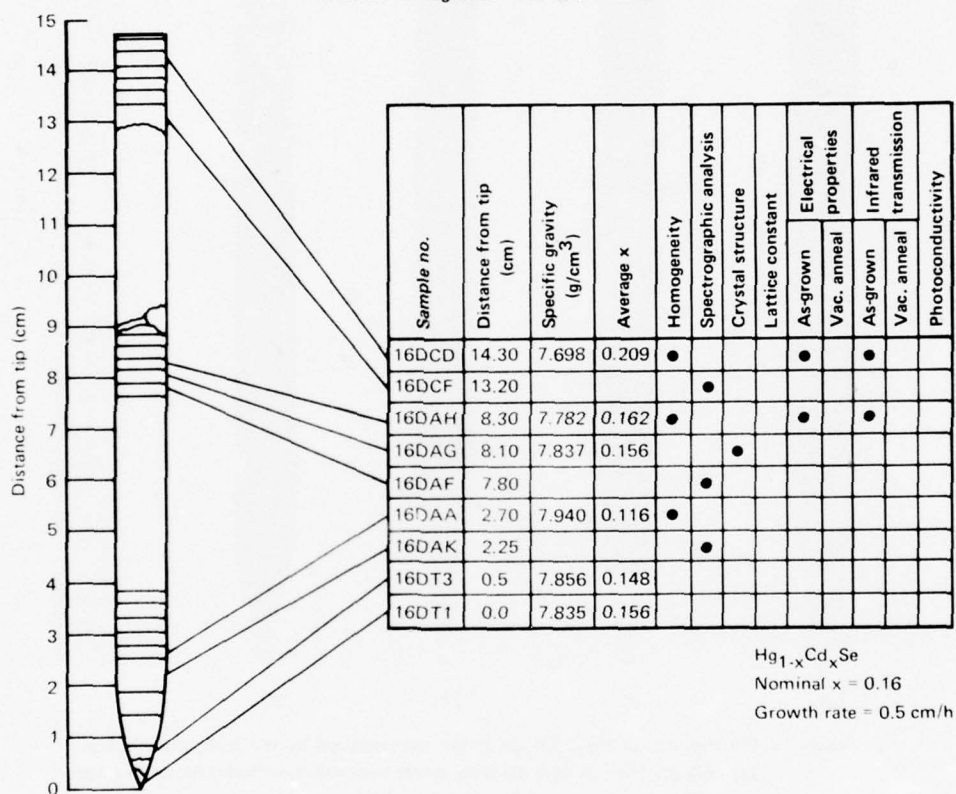


TABLE 5. HgCdSe 16E SAMPLES

$\text{Hg}_{1-x}\text{Cd}_x\text{Se}$
 Nominal $x = 0.16$
 Growth rate = 0.04 cm/h

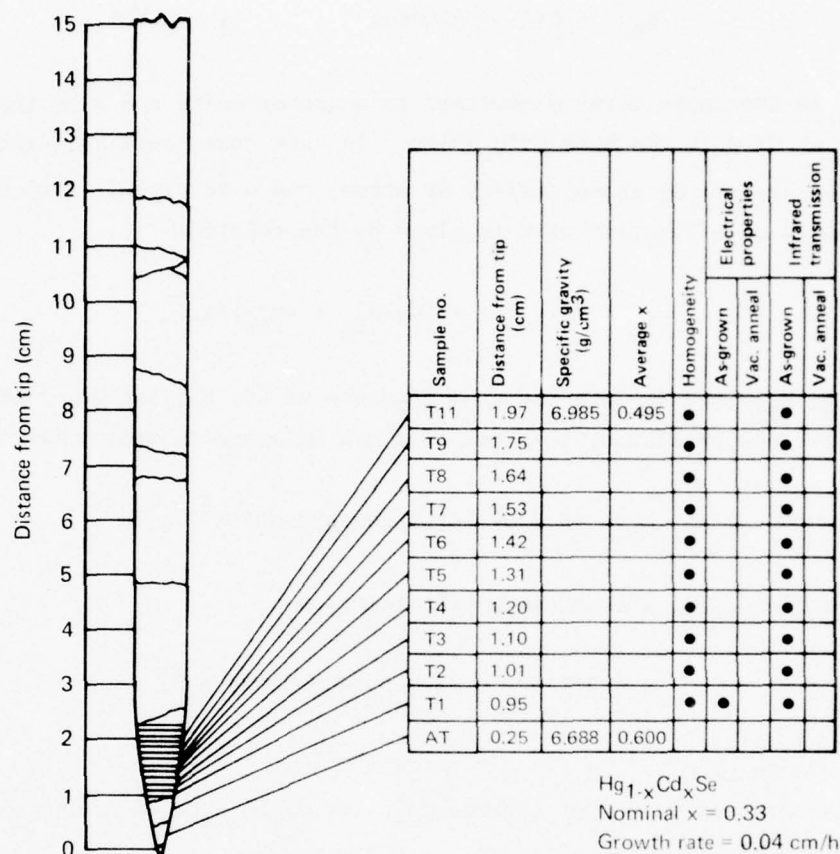
Sample no.	Distance from tip (cm)	Specific gravity (g/cm ³)	Average x	Homogeneity	Spectrographic analysis	Crystal structure	Electrical properties		Infrared transmission		Photoconductivity
							As-grown	Vac. anneal	As-grown	Vac. anneal	
16EE6	13.60				•						
16EE4	13.30				•						
16EE2	12.85	8.064	0.068								
16ED10	10.95			•							
16ED8	10.65				•						
16ED3	9.90	7.908	0.128	•							
16ED2	9.65	7.912	0.127	•							
16EC16	9.25			•		•					
16EC15	9.10			•							
16EC13	8.80	7.837	0.156	•							
16EC12	8.65	7.845	0.153	•				•			
16EC8	8.03	7.843	0.153	•				•		•	
16EC4	7.45			•							
16EC3	7.25				•						
16EC2	7.00	7.782	0.177	•							
16EC1	6.75				•						
16EB12	6.55	7.740	0.193	•				•		•	
16EB11	6.43			•							
16EB10	6.25			•							
16EB9	6.05			•							
16EB8	5.90	7.706	0.206	•				•		•	
16EB7	5.70	7.703	0.207	•				•		•	
16EB6	5.55			•							
16EB5	5.40	7.644	0.230	•							
16EB4	5.23	7.657	0.225	•	•			•		•	
16EB3	5.00			•							
16EA6	4.30	7.650	0.228	•				•		•	
16EA5	4.10										
16EA4	3.95	7.645	0.230	•							
16EA3	3.83	7.630	0.236	•							
16EA2	3.70	7.613	0.243	•							
16EA1	3.55				•						
16ET2	2.40	7.503	0.285		•						
16ET1	1.25	7.440	0.309								

TABLE 6 HgCdSe 24A SAMPLES

$\text{Hg}_{1-x}\text{Cd}_x\text{Se}$
 Nominal $x = 0.24$
 Growth rate = 0.04 cm/h

Sample no.	Distance from tip (cm)	Specific gravity (g/cm ³)	Average x	Homogeneity	Spectrographic analysis	Crystal structure	Electrical properties		Infrared transmission		Photoconductivity
							As-grown	Vac anneal	As-Grown	Vac anneal	
24AE10	12.40			•		•					
24AC1	8.70			•							
24AC2	8.55			•							
24AC3	8.40			•							
24AC4	8.25			•							
24AC5	8.10			•							
24AC6	7.95			•							
24AC7	7.80			•							
24AC8	7.65			•							
24AC9	7.50			•							
24AC10	7.35			•		•					
24AC11	6.3-7.3	7.380	0.332	•		•					
24AC12	6.3-7.3	7.417	0.318	•		•					
24AC13S	6.3-7.3	7.561	0.262	•			•				
24AC13L	6.3-7.3	7.473	0.297	•			•			•	
24AC14	6.3-7.3	7.590	0.251	•							
24AC15	6.3-7.3	7.682	0.216	•				•			
24AB2	6.05			•							
24AB3	5.90			•							
24AB4	5.75			•							
24AB5	5.60			•							
24AB6	5.45			•							
24AB7	5.30			•							
24AB8	5.15			•							
24AB9	5.00			•							
24AB10	4.85			•							
24AB11	3.6-4.8			•							
24AB12	3.6-4.8			•							
24AB13	3.6-4.8			•							
24AB14	3.6-4.8	7.517	0.279	•				•	•	•	•
24AB15	3.6-4.8	7.456	0.303	•							
24AB16	3.6-4.8	7.393	0.328	•				•	•	•	•
24AA1	3.60	7.328	0.353	•				•	•	•	•
24AA2	3.45	7.305	0.362	•							
24AA3	3.30	7.293	0.366	•				•		•	
24AA4	3.15			•							
24AA5	3.00			•							
24AA6	2.85			•							
24AA7	2.70			•							
24AA8	2.55			•							
24AA9	2.40			•							
24AA10	2.25			•		•					
24AT	0.0	7.053	0.459								

TABLE 7 HgCdSe 33A SAMPLES



5.2 Determination of Alloy Composition by Mass Density Measurements

The crystal lattice constant of the $\text{Hg}_{1-x}\text{Cd}_x\text{Se}$ alloys varies so little with x that its measurement cannot be used to calculate precise values for the compositions of specimens. X-ray fluorescence spectroscopy was tried as a method to determine x , but the uncertainty in the derived x -values was ± 0.02 , which is too large for a satisfactory evaluation of the alloys. For this program, x -values of specimens were calculated from their measured mass densities and values of the crystal lattice constant published by Kalb and Leute⁴ (see Figure 2).

The lattice constant data of Kalb and Leute can be represented by the equation

$$a_0 = 6.0856 - 0.0040x \quad (x \leq 0.65), \quad (31)$$

where a_0 is the cubic lattice constant in angstrom units and x is the mole fraction of CdSe in the HgSe-CdSe alloy. In each cubic unit cell there are, on the average, $4x$ Cd atoms, $4(1-x)$ Hg atoms, and 4 Se atoms. Thus the mass density as a function of x is given by the relation

$$\rho_m = (4xM_{\text{Cd}} + 4(1-x)M_{\text{Hg}} + 4M_{\text{Se}})/a_0^3, \quad (32)$$

where M_{Cd} , M_{Hg} , and M_{Se} are the atomic masses of Cd, Hg, and Se, respectively. With sufficient precision, this relation can be approximated by the formula

$$\rho_m = (8.2389 - 2.5829x - 0.0051x^2) \text{ g/cm}^3.$$

As a function of ρ_m , x is given by the relation

$$x = 3.170 - 0.3823 \rho_m - 0.00029 \rho_m^2, \quad (33)$$

where ρ_m is in g/cm^3 .

Table 8 gives values of the mass density of $\text{Hg}_{1-x}\text{Cd}_x\text{Se}$ alloys for $0.00 \leq x \leq 0.65$.

5.3 Method of Measurement of Mass Density

The mass density of a specimen is determined by obtaining its apparent weight, W_a , in air and its apparent weight, W_w , when it is immersed in water. The apparent weights are given by the relations $W_a = V(\rho_m - \rho_a)$ and $W_w = V(\rho_m - \rho_w)$, where V is the specimen volume, ρ_a is the mass density of air, and ρ_w is the mass density of water. These relations, when solved for ρ_m , give the result

$$\rho_m = \frac{W_a \rho_w - W_w \rho_a}{W_a - W_w}. \quad (34)$$

An uncertainty of 0.0026 g/cm^3 in determining ρ_m leads to an uncertainty of 0.001 in calculating x . If the magnitude of the possible errors in measuring W_a and W_w are ΔW_a and ΔW_w , respectively, the resulting uncertainty, $\Delta \rho_m$, in determining ρ_m is

TABLE 8 MASS DENSITY OF $\text{Hg}_{1-x}\text{Cd}_x\text{Se}$ ALLOYS

Mole fraction of CdSe, x	Mass density of $\text{Hg}_{1-x}\text{Cd}_x\text{Se}$ alloy (g/cm ³)	Mole fraction of CdSe, x	Mass density of $\text{Hg}_{1-x}\text{Cd}_x\text{Se}$ alloy (g/cm ³)
0.00	8.239	0.33	7.386
0.01	8.213	0.34	7.360
0.02	8.187	0.35	7.334
0.03	8.161	0.36	7.308
0.04	8.135	0.37	7.282
0.05	8.110	0.38	7.257
0.06	8.084	0.39	7.231
0.07	8.058	0.40	7.205
0.08	8.032	0.41	7.179
0.09	8.006	0.42	7.153
0.10	7.980	0.43	7.127
0.11	7.955	0.44	7.101
0.12	7.929	0.45	7.076
0.13	7.903	0.46	7.050
0.14	7.877	0.47	7.024
0.15	7.851	0.48	6.998
0.16	7.825	0.49	6.972
0.17	7.800	0.50	6.946
0.18	7.774	0.51	6.920
0.19	7.748	0.52	6.894
0.20	7.722	0.53	6.868
0.21	7.696	0.54	6.843
0.22	7.670	0.55	6.817
0.23	7.644	0.56	6.791
0.24	7.619	0.57	6.765
0.25	7.593	0.58	6.739
0.26	7.567	0.59	6.713
0.27	7.541	0.60	6.687
0.28	7.515	0.61	6.661
0.29	7.489	0.62	6.635
0.30	7.464	0.63	6.610
0.31	7.438	0.64	6.584
0.32	7.412	0.65	6.558

$$\Delta\rho_m \approx \frac{(1+\rho_m)\Delta W_a + \rho_m \Delta W_w}{\Delta W_a} \rho_m, \quad (35)$$

where it has been assumed that ρ_w is exactly 1.0 g/cm^3 and that there is no error in determining ρ_w . A circular slice of $\text{Hg}_{1-x}\text{Cd}_x\text{Se}$ alloy, 10 mm diam \times 0.5 mm thick, weighs approximately 0.5 g, and for a specimen of this weight, ΔW_a must be less than 0.000002 g and ΔW_w less than 0.00002 g for $\Delta\rho_m$ to be sufficiently small ($< 0.0026 \text{ g/cm}^3$) to give x to within ± 0.001 . For specimens that weigh less than 0.5 g, it is difficult to make all the weight measurements with sufficient precision to calculate x to within ± 0.001 . For example, x can, at best, be determined to within ± 0.006 for a $1 \times 1 \times 10$ mm Hall effect sample.

The method described by Bowman and Schooner²¹ is used for the mass density determinations. The $\text{Hg}_{1-x}\text{Cd}_x\text{Se}$ specimen is immersed in water, and the water is boiled briefly to eliminate gases dissolved in the water and to rid the specimen of minute air bubbles that may be attached to it. After the sample and the water have cooled to room temperature, the weight of the immersed specimen is measured with a balance that weighs with a precision of ± 0.000001 g. However, the precision of the weight determination in water is much poorer than this because of the surface-tension forces upon the 0.013 mm diam wire that is used to suspend the specimen from the balance arm. Some of the suspension wires that have been prepared permit the weight in water to be determined with an accuracy of ± 0.00001 g, but usually an accuracy of only ± 0.00002 g is achieved. To do significantly better requires an inordinate amount of time.

The following expression, from Reference 21, is used to calculate the density of the water in which the sample is immersed:

$$\begin{aligned} \rho_w = & \left[1 - \frac{(t_w - 3.9863)^2}{508929.2} \times \frac{t_w + 288.9414}{t_w + 68.12963} \right] \\ & \times \left[0.999973 \right] \left[\frac{1}{1-C \left(\frac{B}{760} + \frac{I}{1033} - 1 \right)} \right] \\ & \times \left[1 - (2.11 - 0.053t_w) \left(1 - \frac{1}{1+D} \right) (10^{-6}) \right] \text{ g/cm.} \end{aligned} \quad (36)$$

In this expression, t_w is the water temperature in °C, C is the compressibility of water ($C = 47.7$ ppm/atm), B is the barometric pressure in Torr, I is the depth of immersion of the sample in water in cm, and D is the number of days elapsed since the water was boiled. After the measurement in water, the specimen is dried and weighed in air with the same balance. The mass density of air is calculated from the following expression given in Reference 21:

$$\rho_a = \left[\frac{464.56B - H(0.085594t_a^2 - 1.8504t_a + 34.47)}{t_a + 273.16} \times 10^{-6} \right] \text{ g/cm}^3, \quad (37)$$

where H is the relative humidity in percent and t_a is the air temperature in °C.

Nichrome (80Ni-20Cr) wire, 0.013 mm diam, was used to suspend the specimens for the weighings in water. The wires were baked at 700-800°C for 1 h in air at 0.1 Pa (1×10^{-3} Torr) to prepare their surfaces. The oxidized surfaces of the wires developed micro-fissures when the wires were cooled. These micro-fissures cause the water meniscus and surface tension to be nearly the same at each point along the wire when it is raised and lowered in the water during the weighings. No surface film on the water is tolerable, and microscopic dust particles in the meniscus region can invalidate the weight measurements in water.

5.4 Laue Topography

The crystalline perfection of several $\text{Hg}_{1-x}\text{Cd}_x\text{Se}$ slices was investigated by Laue topography. The experimental procedure employed is similar to that described by Swink and Brau²² and permits a rapid, non-destructive evaluation of macroscopic defects.

The apparatus, a diagram of which is given in Figure 14, consists of a fine-focus, sealed-tube, x-ray source and a Laue back-reflection camera. The pinhole collimator is removed from the camera, and the distances between the x-ray source, camera, and sample are adjusted so that the diameter of the x-ray beam at the sample surface is 0.5 cm. The sample-

to-film distance can be adjusted to obtain back-reflected Laue spots that have diameters of 0.5 - 1.0 cm. Good results are obtained with a source-to-sample distance of 12 cm and sample-to-film distances of 3-9 cm. A copper x-ray source that is operated at 15 kV and 50 mA gives Laue spots with optimum contrast for 30-min exposures on Kodak NS-54T film when the sample-to-film distance is 5 cm.

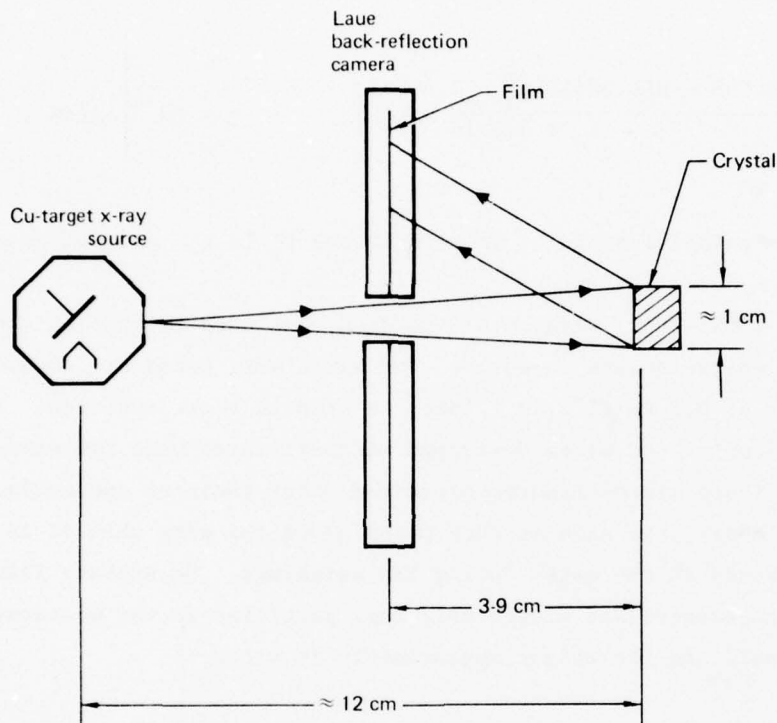


Figure 14 Diagram of Laue topography apparatus

Each back-reflected Laue spot is an image of the region of the sample that is illuminated by the x-ray source. Crystalline misorientations over the illuminated region cause gradations of the intensity within each Laue spot-image. If the crystal is perfect, each Laue spot is uniform in intensity over its entire area. Adjacent crystal grains that are only slightly misaligned have slightly different image intensities. A spot-image that appears "mottled" is representative of crystals that have a high density of small-angle grain boundaries.

Because the Laue reflections are from only the near-surface region of the samples, it is essential that the surfaces be as damage free as possible. The $\text{Hg}_{1-x}\text{Cd}_x\text{Se}$ samples were optically polished and then etched to remove surface damage before they were studied by Laue topography.

Figure 15 is a Laue topograph of a slice cut perpendicular to the growth axis and 11.2 cm from the bottom tip of crystal 16E. The symmetry of the spots on the photograph shows that the growth direction is one characterized by high Miller-indices (probably $\langle 123 \rangle$). Each spot represents an image of the sample surface. The white, nearly horizontal lines represent small-angle grain-boundaries that are concave in their orientation to the incoming x-ray beam. The degree of overlap of the images of adjacent grains shows that the relative misorientation between grains is small ($\approx 0.25^\circ$). The dark spot just above the center of the image represents a small grain, and the image of this grain appears above the main image. The misorientation of this grain is approximately 4° .

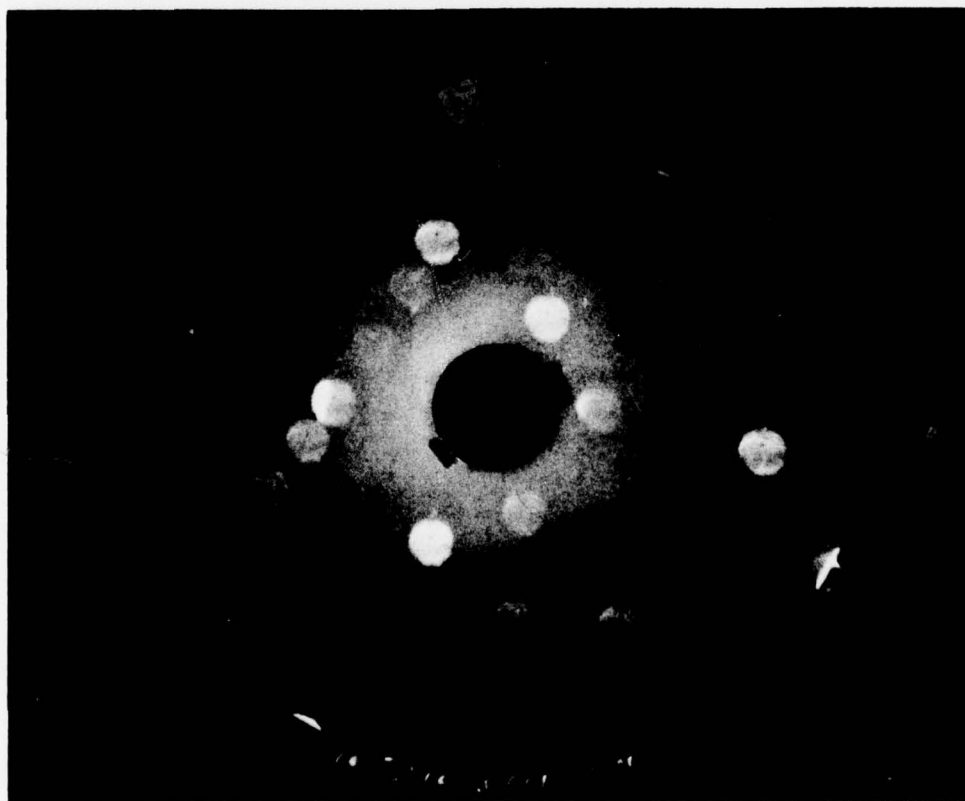


Figure 15 Laue topograph of HgCdSe 16E slice

Figures 16, 17 and 18 show topographs from three slices cut perpendicular to the growth axis at distances of 2.2, 7.4 and 12.3 cm, respectively, from the bottom tip of crystal 24A. The topographs clearly demonstrate the $\langle 100 \rangle$ growth direction of the primary grain structure of the ingot. Figures 16 and 17 show a similar substructure that consists of horizontal lines and two highly misoriented grains in the center. Figure 17 shows considerable substructure at the center of the ingot and a large, rectangular-shaped grain near the center. Near the ingot top (Figure 18), the image is more uniform, which is indicative of less substructure. Two grains are evident in Figure 18: a V-shaped grain at the top and a small grain at the lower right. Both of these grains are convex in their orientation to the x-ray beam. Figure 19 is a topograph obtained from a slice cut 7.5 cm from the bottom tip of crystal 33A, and this image is similar in quality to those obtained from crystal 24A.

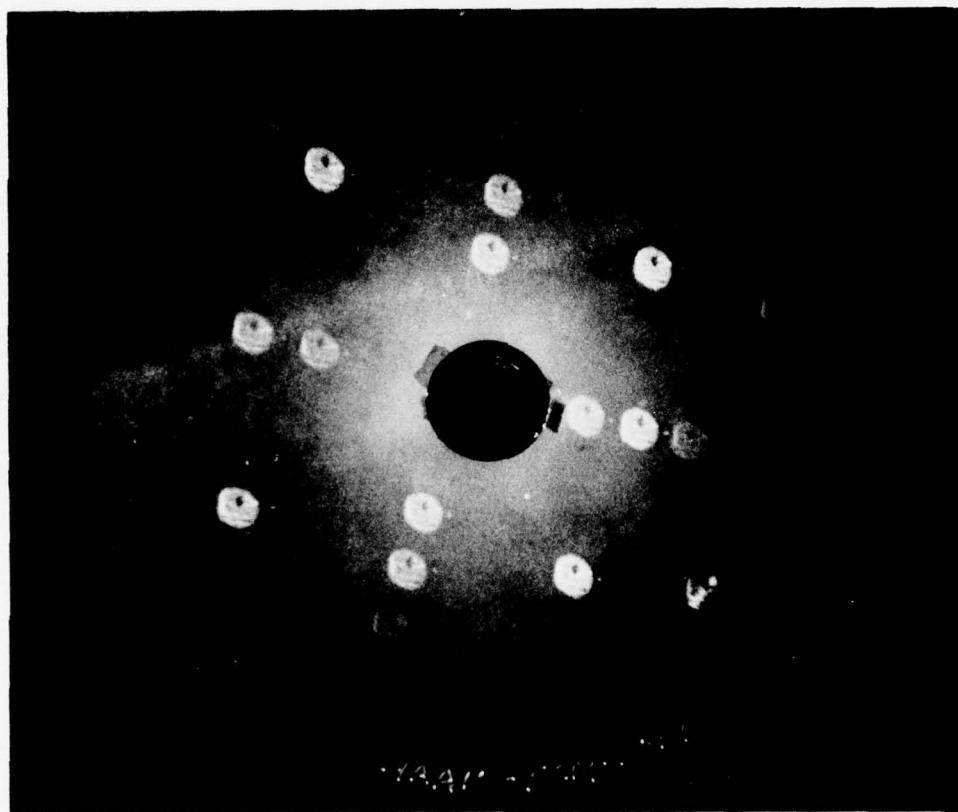


Figure 16 Laue topograph of HgCdSe 24A slice 2.2 cm from bottom of ingot

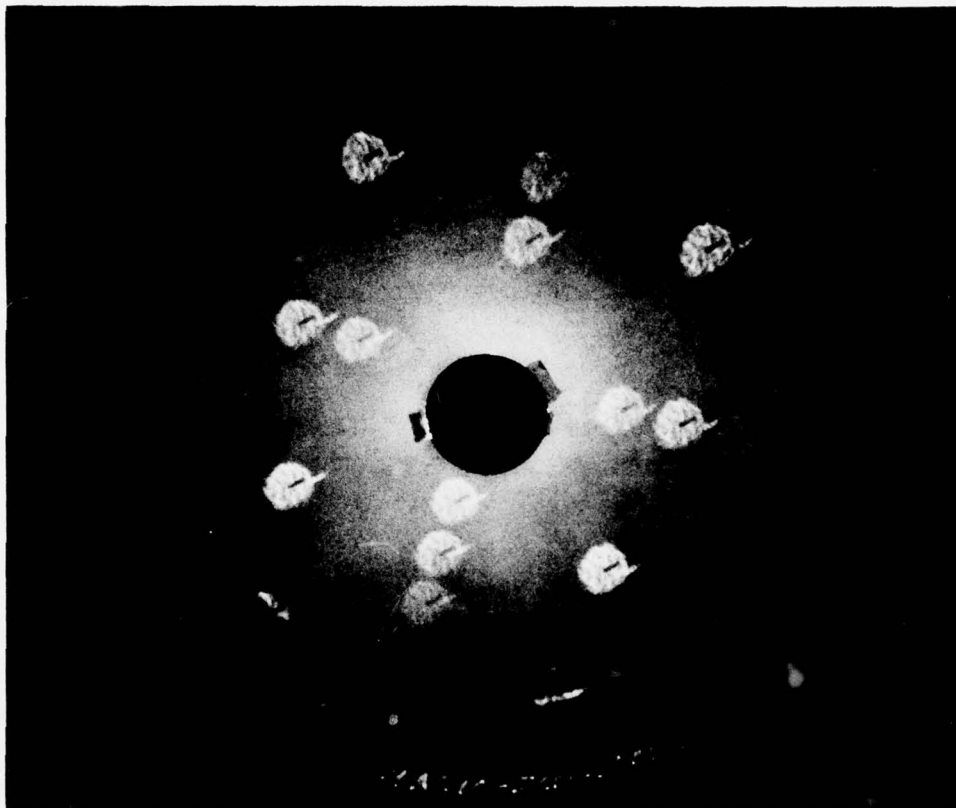


Figure 17 Laue topograph of HgCdSe 24A slice 7.4 cm from bottom of ingot

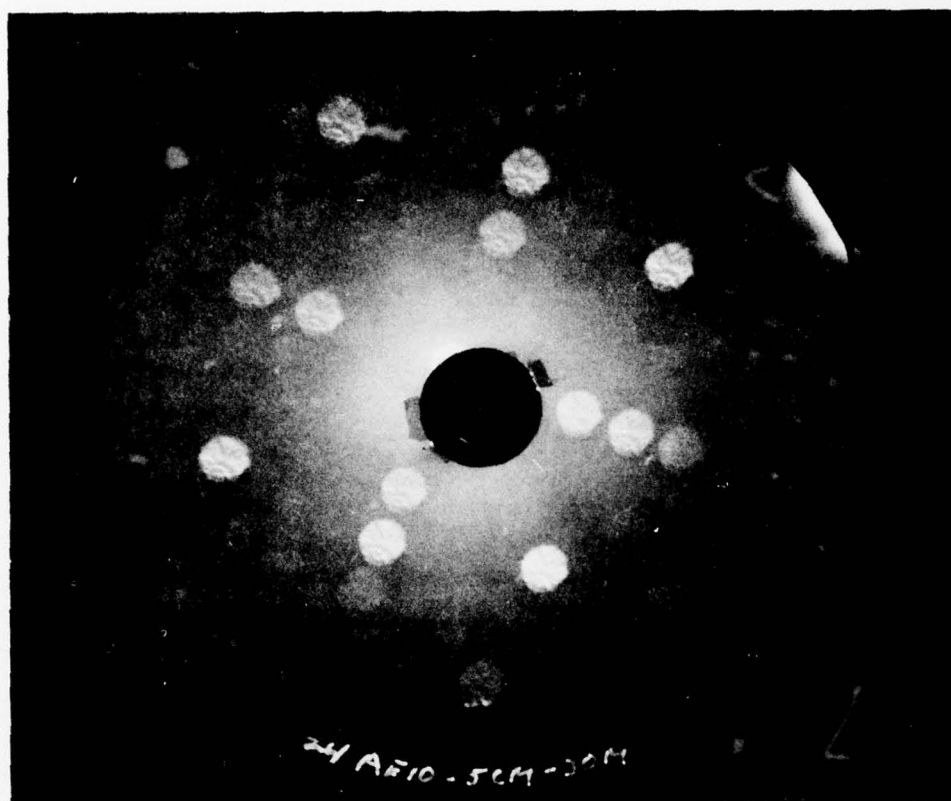


Figure 18 Laue topograph of HgCdSe 24A slice 12.3 cm from bottom of ingot

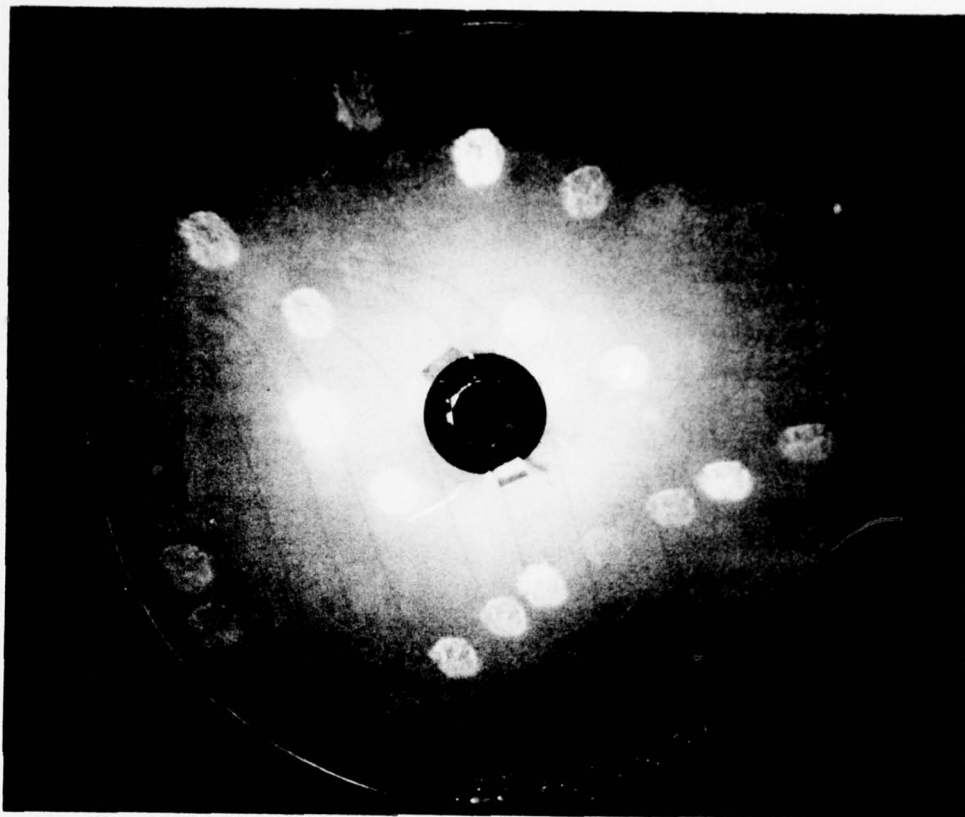


Figure 19 Laue topograph of HgCdSe 33A slice 7.5 cm from bottom of ingot

Crystals 24A and 33A were grown at the comparable rates of 0.04 and 0.03 cm/h, respectively, but the temperature gradient was increased from 13°C/cm to 35°C/cm for the growth of 33A. The Laue topographs show that this change had little effect on the crystal quality. Crystal 16E was also grown with a temperature gradient of 13°C/cm, but the upper 6 cm was grown at the faster rate of 0.5 cm/h. The topographs for a slice from the upper 6 cm of 16E (Figure 15) had the most uniform images, and this suggests that the faster growth-rate produces crystals of greater perfection.

5.5 Compositional Homogeneity Determinations

To determine the homogeneity of individual slices, measurements were made of the room-temperature infrared transmission through 1 mm diam areas at regularly spaced locations on each slice. Many of the slices from

HgCdSe ingots 16D, 16E, and 24A were screened in this manner. Representative data for one slice, 24AA1, are shown in Figure 20.

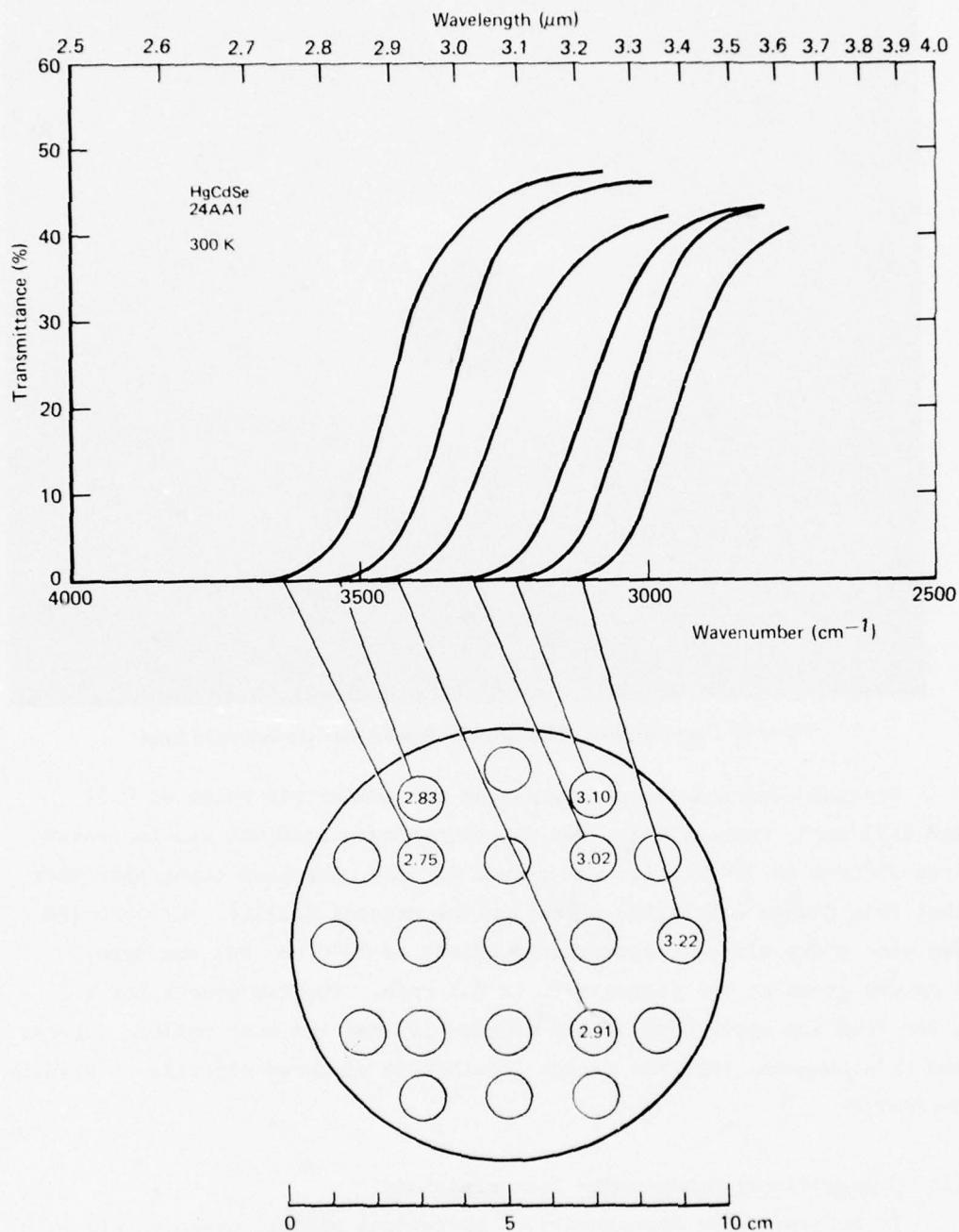


Figure 20. Representative transmittance spectra at 300 K for 1 mm diam areas on a 1 cm diam $\text{Hg}_{1-x}\text{Cd}_x\text{Se}$ crystal slice; numbers in circles are transmission-edge wavelengths in μm

In Figures 21-27 are shown the infrared-transmission screening results for crystal slices that were used for optical and electrical measurements. The small circles indicate the locations on the 1 cm diam slices of the 1 mm diam areas through which the infrared transmission spectra were measured. The number in each circle is the wavelength at which that particular area began to transmit. In Table 9 are listed approximate x-values that correspond to various wavelengths; the x-values were calculated on the basis that the material has 1×10^{17} electrons/cm³, and although the magnitudes of the x-values may not be precise, the difference between x-values for wavelengths that differ by only $\approx 1 \mu\text{m}$ are sufficiently accurate to assess the homogeneity of the alloy slices. Specimens for measurements usually were cut from those regions of the slices for which x deviated no more than ± 0.005 from the average x-value for each specimen.

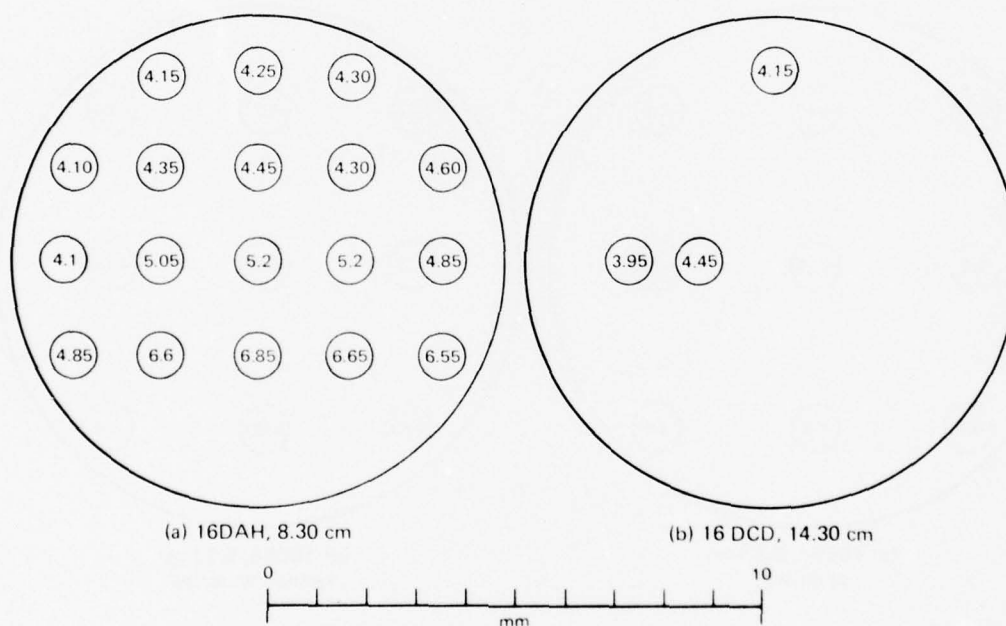


Figure 21 Homogeneity of as-grown HgCdSe 16DAH and 16DCD slices; numbers are wavelengths in μm for onset of transmission at 300 K through the 1 mm diam areas; blank areas did not transmit; distances of slices from bottom tip of the crystal are given

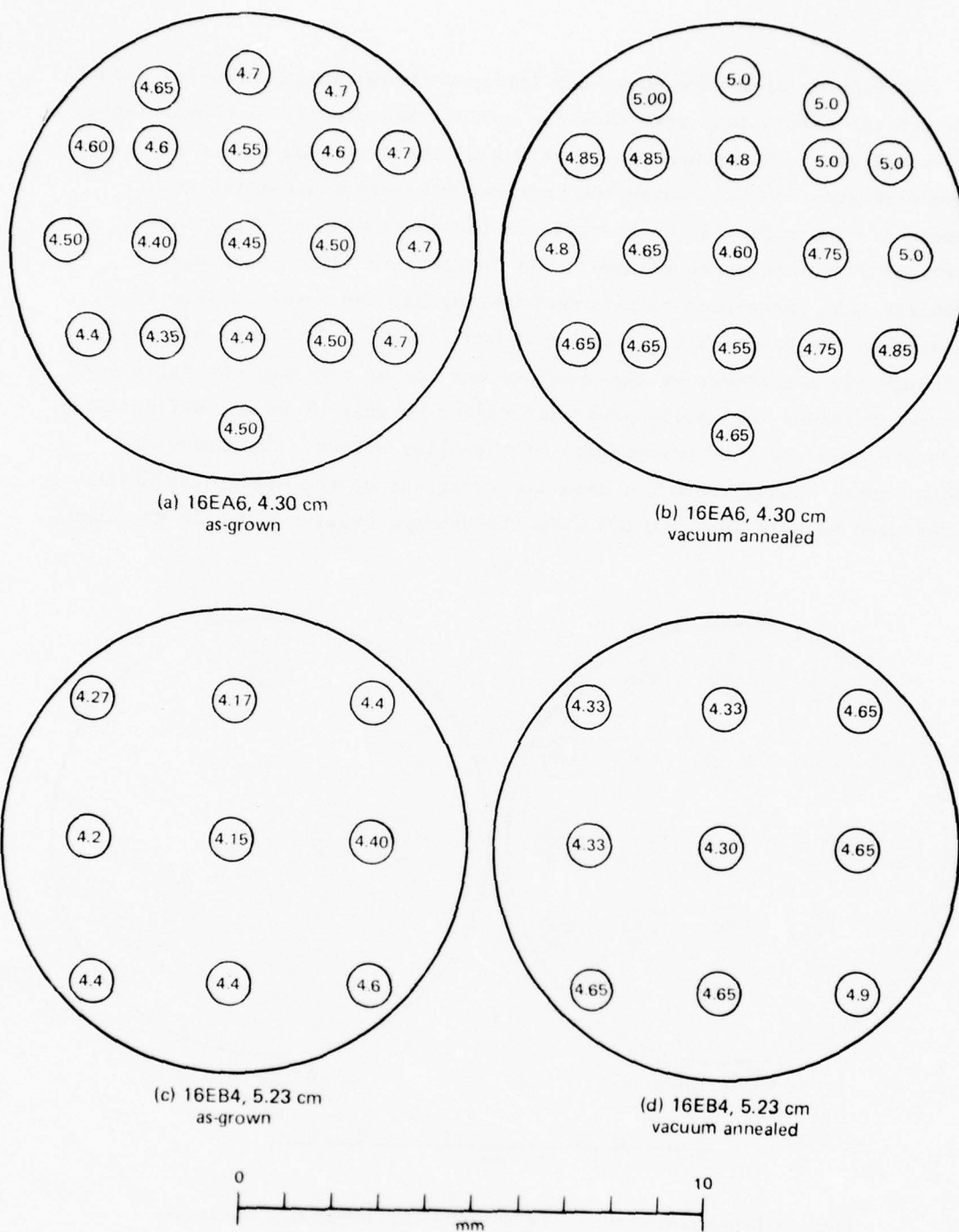


Figure 22 Homogeneity of HgCdSe 16EA6 and 16EB4 slices; numbers are wavelengths in μm for onset of transmission through the 1 mm diam areas; distances of slices from bottom tip of the crystal are given

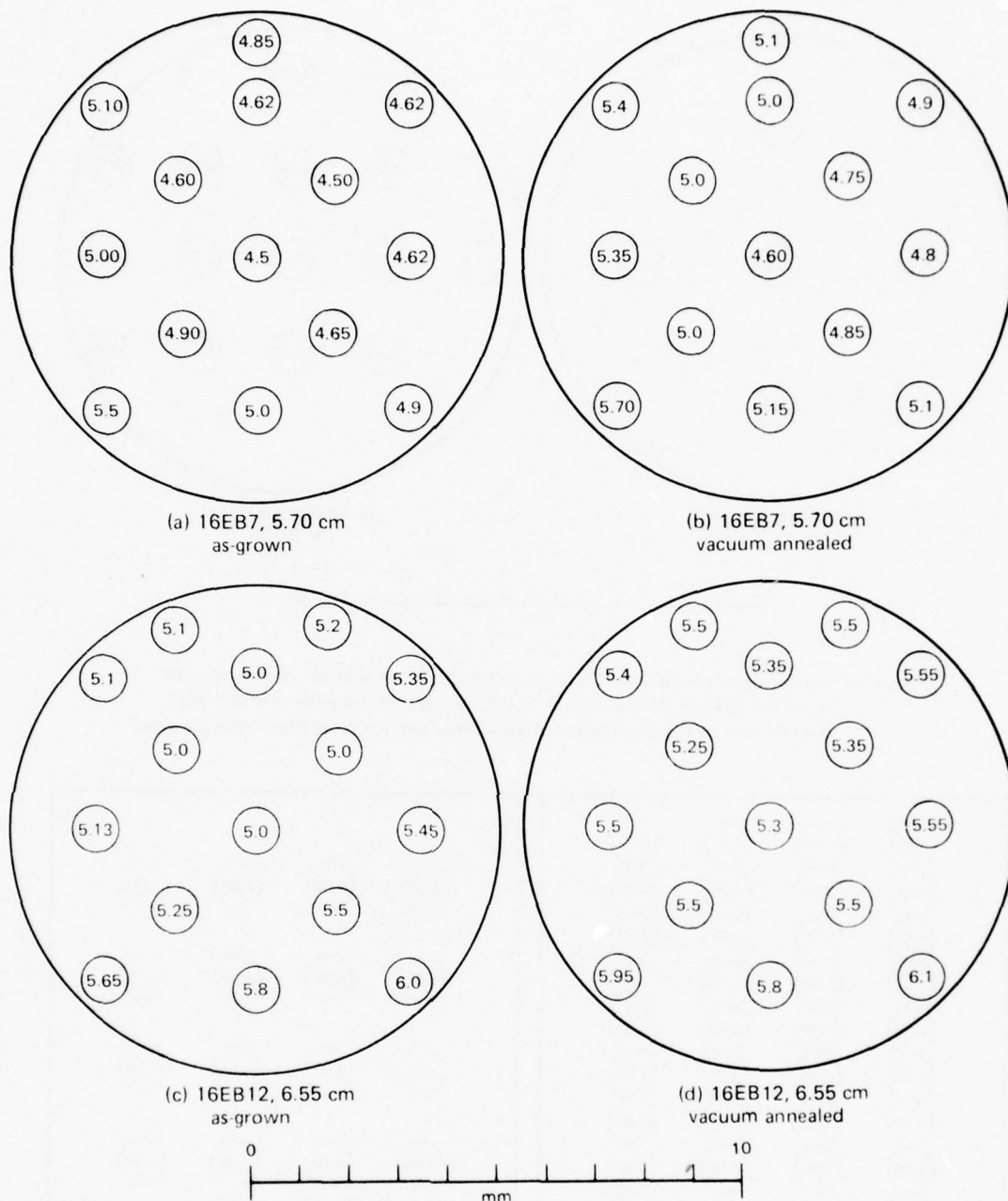


Figure 23 Homogeneity of HgCdSe 16EB7 and 16EB12 slices; numbers are wavelengths in μm for onset of transmission through the 1 mm diam areas; distances of slices from bottom tip of the crystal are given

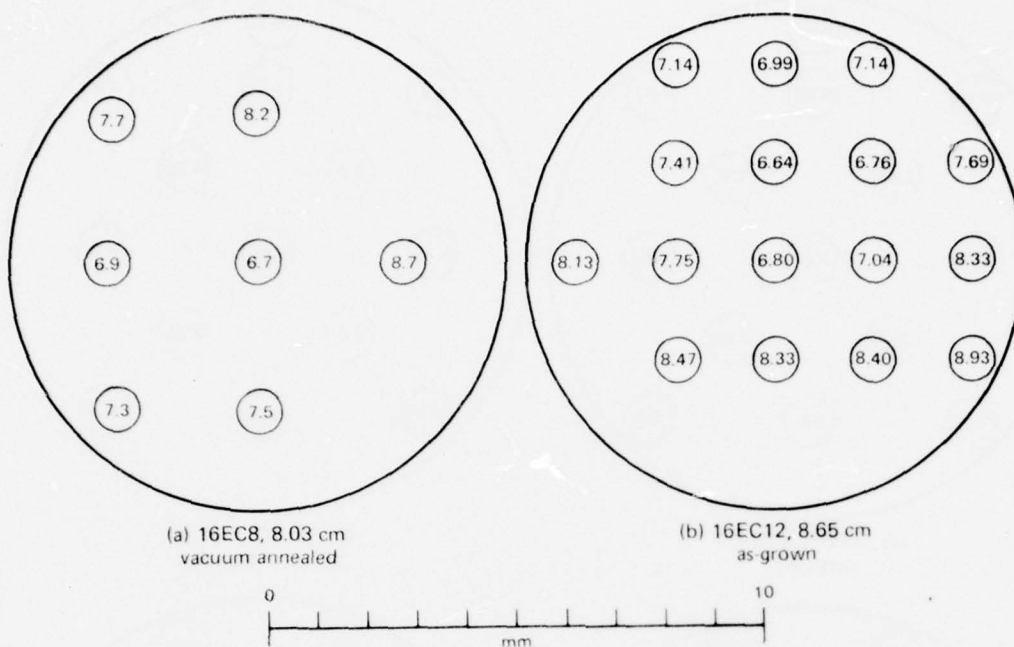


Figure 24 Homogeneity of HgCdSe 16 EC8 and 16 EC12 slices; numbers are wavelengths in μm for onset of transmission at 300 K through the 1 mm diam areas; blank areas did not transmit; distances of slices from bottom tip of the crystal are given

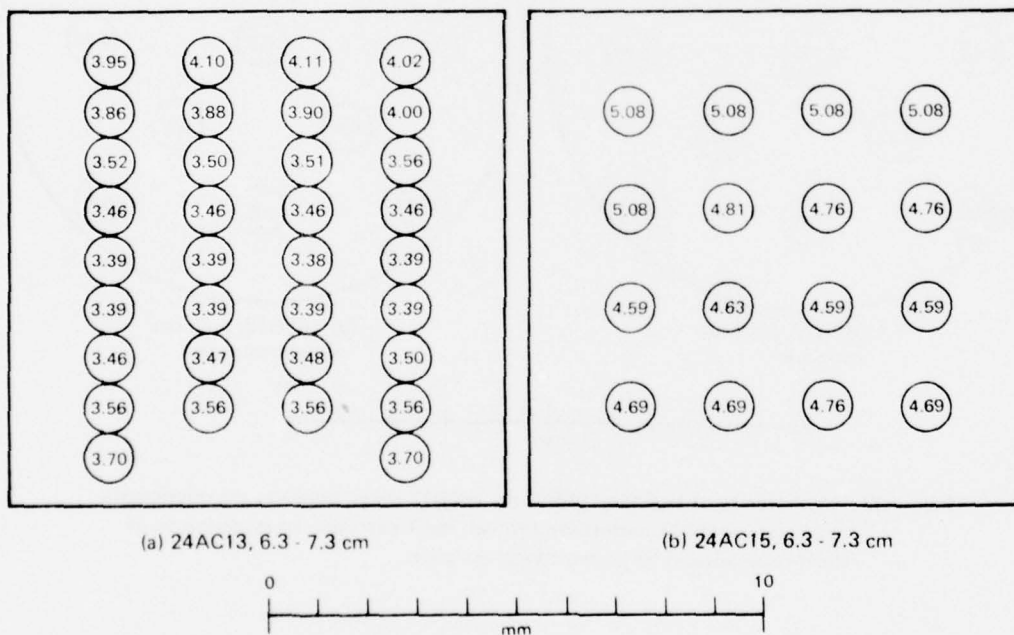


Figure 25 Homogeneity of as-grown HgCdSe 24AC13 and 24AC15 slices; numbers are wavelengths in μm for onset of transmission through the 1 mm diam areas; distances of slices from bottom tip of the crystal are given

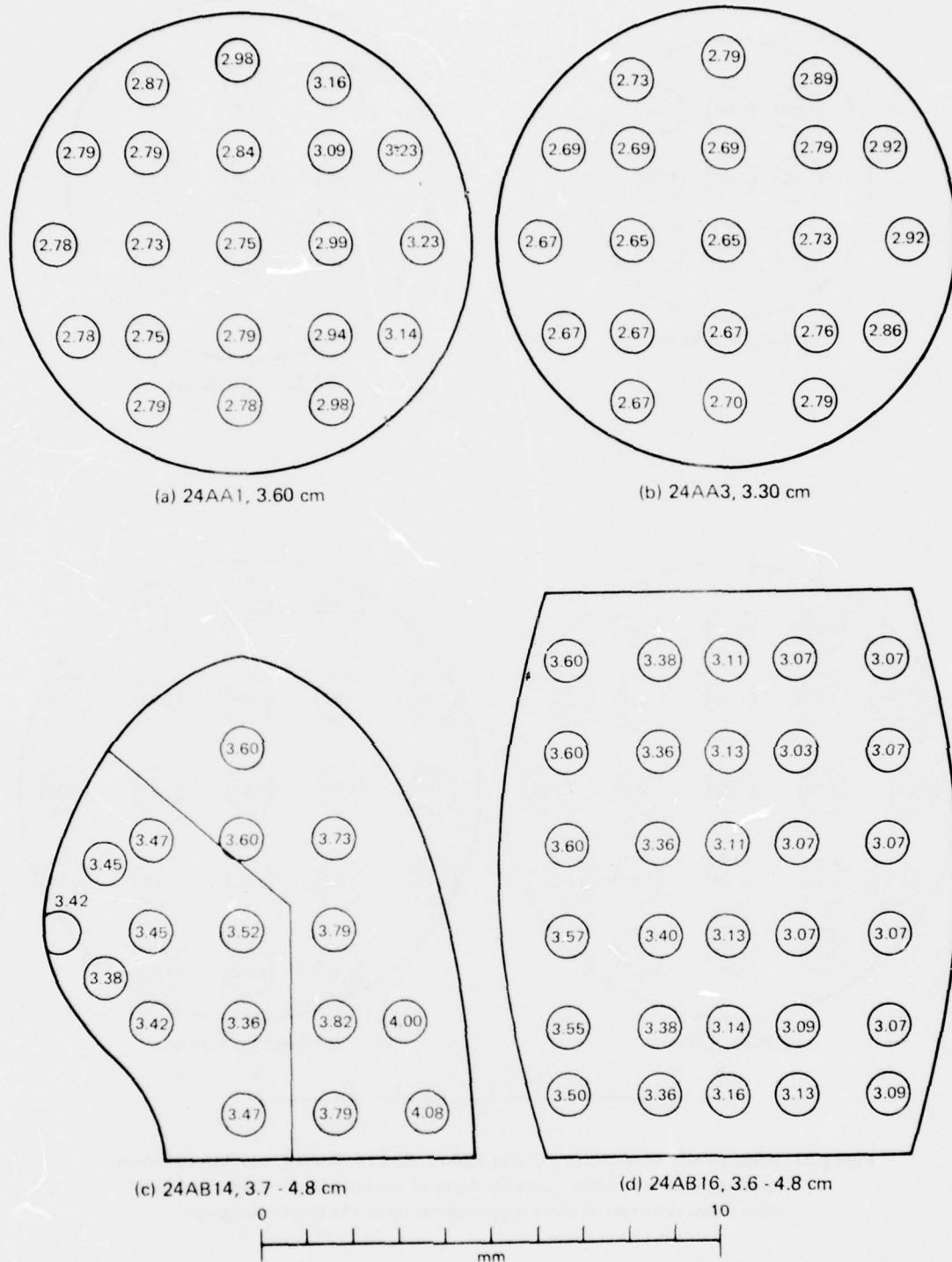


Figure 26 Homogeneity of as-grown HgCdSe 24AA1, 24AA3, 24AB14, and 24AB16 slices; numbers in circles are wavelengths in μm for onset of transmission through 1 mm diam areas; distances of slices from bottom tip of the crystal are given

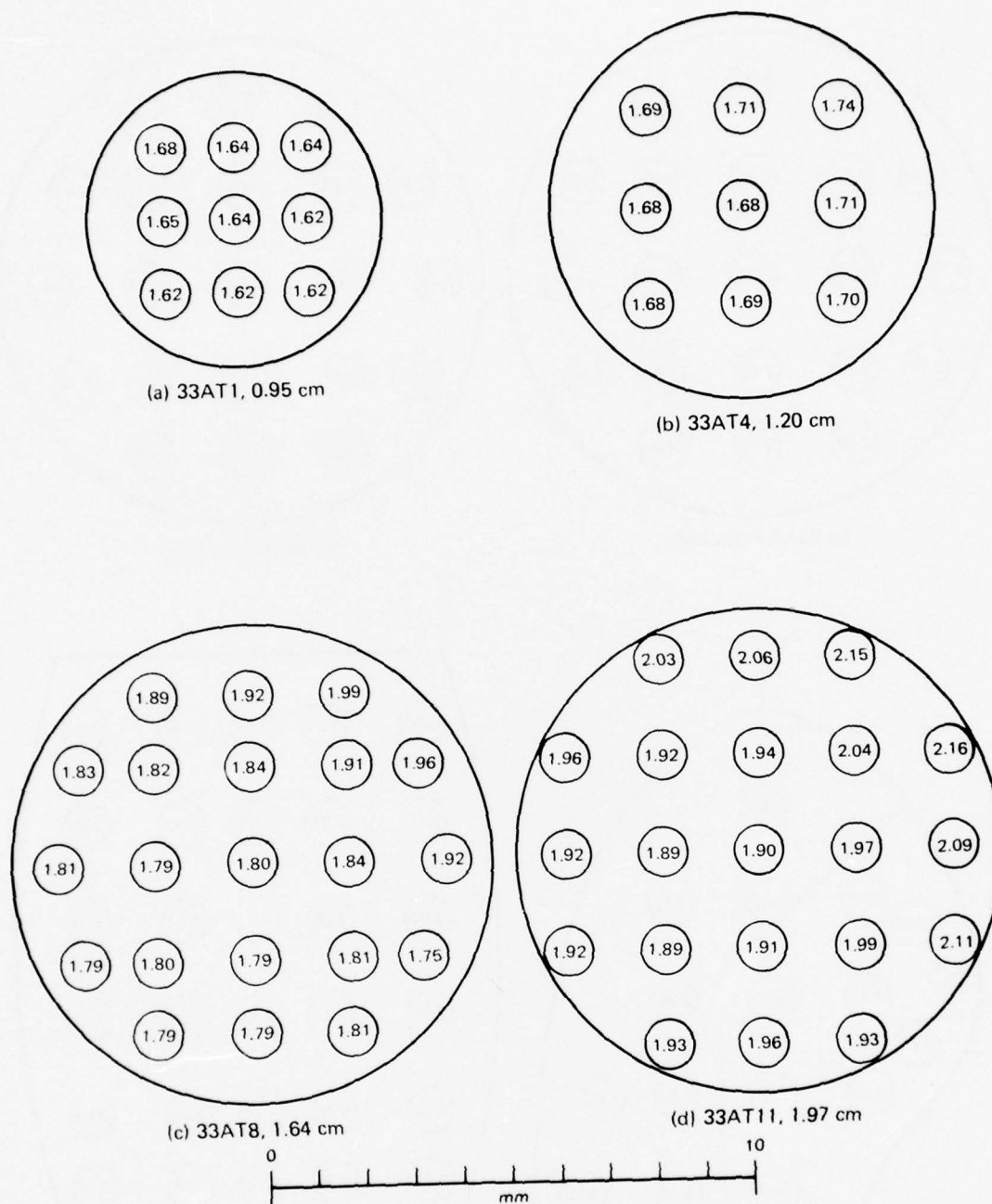


Figure 27 Homogeneity of as-grown HgCdSe 33AT1, 33AT4, 33AT8, and 33AT11 slices; numbers are wavelengths in μm for onset of transmission through the 1 mm diam areas; distances of slices from bottom tip of the crystal are given

TABLE 9 APPROXIMATE x-VALUES CORRESPONDING TO TRANSMISSION-
EDGE WAVELENGTHS FOR $\text{Hg}_{1-x}\text{Cd}_x\text{Se}$ AT 300 K

Wavelength λ (μm)	Mole fraction of CdSe x
2.4	0.33
2.6	0.31
2.8	0.29
3.0	0.27
3.2	0.25
3.4	0.24
3.6	0.23
3.8	0.22
4.0	0.21
4.2	0.20
4.4	0.19
4.6	0.18
4.8	0.17
5.0	0.17
5.2	0.16
5.4	0.16
5.6	0.15
5.8	0.14
6.0	0.14
6.2	0.13
6.4	0.13
6.6	0.13
6.8	0.12
7.0	0.12
7.2	0.11
7.4	0.11

All of the slices of crystal 24A were mapped by the infrared-transmittance method, and the results were used to construct the equal-x contours for two, perpendicular, longitudinal planes through the crystal, as shown in Figure 28. The equal x-contours in the original HgCdSe 24A boule tended to be transverse to the crystal growth direction at the bottom and parallel to the growth direction as recrystallization proceeded. The irregular, higher-x contours along one side of 24A indicate that the crystal growth from the initial bottom tip proceeded preferentially up one side of the ingot. The relative uniformity of the contours in the longitudinal direction above the tapered, bottom section implies that there was very little mixing of the melt in the vertical direction during crystal growth, for otherwise the contours would be transverse and x would steadily decrease towards the top of the ingot.

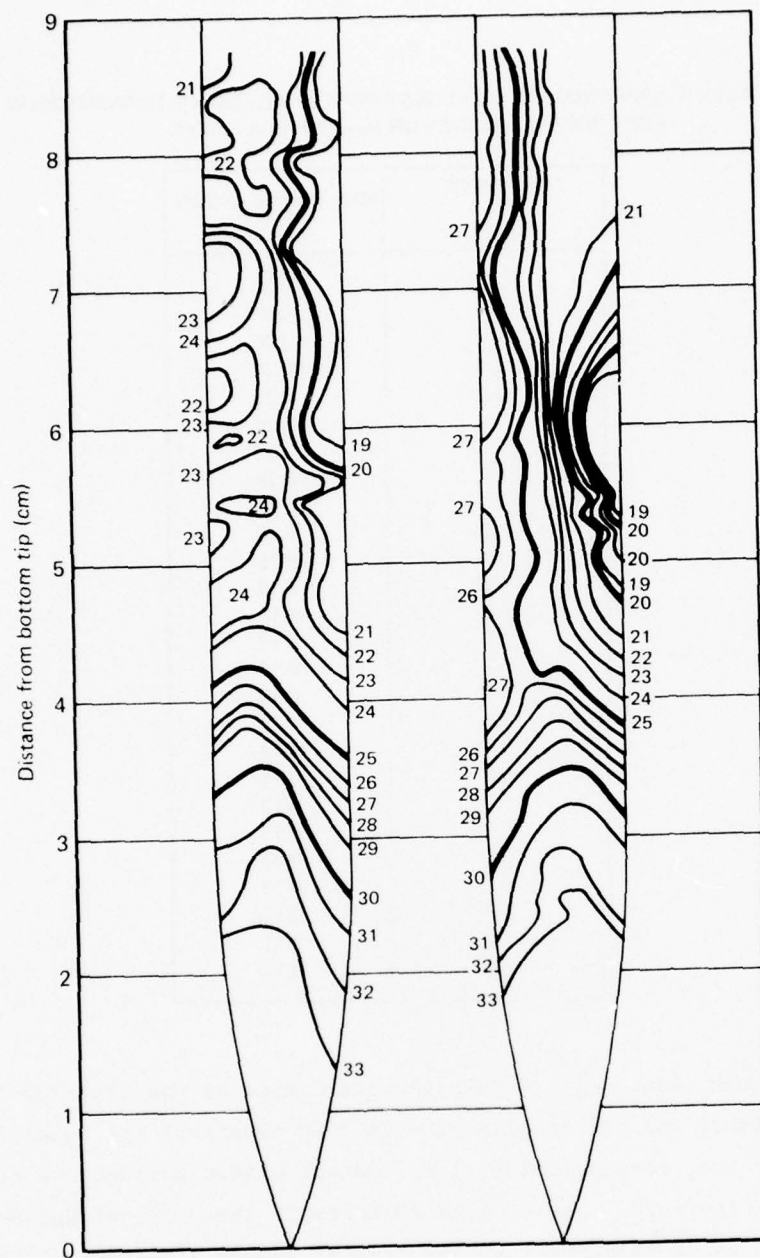


Figure 28. Equal-x contours in perpendicular longitudinal planes of HgCdSe 24A; numbers are x-values in hundredths

The contours shown in Figure 28 provide an explanation for the erroneous conclusion formed during preliminary work that the composition of Bridgman-grown crystals of $\text{Hg}_{1-x}\text{Cd}_x\text{Se}$ does not vary significantly in the longitudinal direction. The equal-x contours are nearly vertical for two-thirds of the crystal length, and the average x-value as calculated from the mass density varies little from transverse-slice to slice.

The crystal HgCdSe 33A, which was grown in the Bridgman furnace after the sodium-vapor, isothermal furnace-liners had been added to reduce temperature gradients, had a much greater radial homogeneity than 16D, 16E, or 24A.

5.6 Vacuum Annealing of $\text{Hg}_{1-x}\text{Cd}_x\text{Se}$

Vacuum annealing of $\text{Hg}_{1-x}\text{Cd}_x\text{Se}$ alloys at temperatures between 200° and 300°C typically reduces the extrinsic electron concentration by an order of magnitude and approximately doubles the low-temperature electron mobility. All alloy specimens selected for material characterization measurements were first subjected to a vacuum anneal, which is performed by heating the specimens in a quartz furnace tube that is continuously evacuated and maintained at a pressure of $\approx 10 \mu\text{Pa}$ (1×10^{-7} Torr).

The lowest electron concentration achieved by vacuum annealing was in sample 24AA1, for which $x = 0.352$. After this 0.33 mm thick sample was annealed in vacuum at 260°C for 67 h and 240°C for an additional 93 h, its electron concentration was 8.4×10^{15} electrons/cm³ and was independent of temperature between 4.2 and 300 K.

5.7 Selenium-Vapor Annealing of $\text{Hg}_{1-x}\text{Cd}_x\text{Se}$

A study was made of the effectiveness of annealing $\text{Hg}_{1-x}\text{Cd}_x\text{Se}$ specimens in Se vapor to reduce the extrinsic-electron concentrations in the specimens. Before being annealed, the specimens were cleaned in methanol and lightly etched. They were then placed in a quartz boat within a quartz capsule, together with sufficient Se in a separate boat to produce a saturated Se vapor at the annealing temperature. The quartz capsule was then evacuated to a pressure of $\approx 1 \text{ mPa}$ (1×10^{-5} Torr) and heated to 250°C to drive off contaminants that may have been absorbed on the Se pellet and specimen surfaces. The capsule was then evacuated to $\approx 10 \mu\text{Pa}$ (1×10^{-7} Torr),

back-filled with He gas to ≈ 100 Pa (1 Torr), and sealed. The capsule and its contents were then heated in a furnace, which was controlled to maintain the desired annealing temperature. Se-vapor anneals were terminated by quickly removing the capsule from the furnace and quenching one end in ice water. This was done to condense the Se vapor onto the capsule walls and to avoid coating the $\text{Hg}_{1-x}\text{Cd}_x\text{Se}$ specimens. The He gas in the capsule effected a rapid cooling of the specimens.

Five $\text{Hg}_{1-x}\text{Cd}_x\text{Se}$ samples were annealed in Se vapor at 200°C for 85 h, at 250°C for 70 h, and subsequently, at 350°C for 17 h. These samples were cut from the same piece of ingot and had $x \approx 0.29$. The extrinsic electron concentrations and mobilities in the samples as-grown and as-annealed are listed in Table 10. Equilibrium between the samples and Se vapor at 200°C apparently was not achieved, but the near uniformity of the properties of the samples after the higher-temperature anneals indicates that equilibrium was achieved at the higher temperatures.

TABLE 10 ELECTRICAL CHARACTERISTICS OF $\text{Hg}_{0.71}\text{Cd}_{0.29}\text{Se}$ ANNEALED IN Se VAPOR

Sample No.		AT2				AT4				AT5				AT3	AT6
Thickness (mm)		0.630				0.497				0.388				0.628	0.462
Temperature of Se-vapor anneal ($^\circ\text{C}$)		AG*	200	250	350	AG	200	250	350	AG	200	250	350	250	250
Duration of Se-vapor anneal (h)			85	70	17		85	70	17		85	70	17	70	70
Electron concentration (4.2 - 300 K) (10^{17}cm^{-3})		1.47	1.12	1.02	1.11	1.21	1.03	0.96	0.99	1.22	0.90	0.95	0.96	1.07	0.96
Electron mobility ($\text{m}^2/\text{V s}$)	(4.2 K)	—	1.91	2.01	2.01	1.56	1.76	1.92	1.85	1.50	1.73	1.93	1.96	1.94	1.92
	(80 K)	1.07	1.28	1.34	1.30	1.10	1.11	1.26	1.23	1.04	1.16	1.28	1.27	1.26	1.27
	(300 K)	0.260	0.275	0.284	0.275	0.259	0.271	0.276	0.270	0.247	0.254	0.277	0.264	0.259	0.278
Ratio of 4.2 K to 300 K mobilities		—	6.99	7.19	7.35	6.10	6.59	6.94	6.93	6.09	6.86	6.98	7.55	7.67	6.91

$\text{Hg}_{1-x}\text{Cd}_x\text{Se}$ remains n-type upon being annealed in Se vapor, and the equilibrium conduction-electron concentration is slightly larger for a 350°C anneal than for a 250°C anneal. Prolonged annealing of $\text{Hg}_{1-x}\text{Cd}_x\text{Se}$ in Se vapor cannot effect electron concentrations as low as those that are readily achieved by annealing in vacuum.

For a given conduction-electron concentration, the ratio of the electron mobility at 4.2 K to that at 300 K is indicative of the degree of crystalline perfection. As Table 10 shows, the $\mu_n(4.2\text{ K})/\mu_n(300\text{ K})$ ratio of $\text{Hg}_{1-x}\text{Cd}_x\text{Se}$ increases when the alloy is annealed in Se vapor, and this implies that the annealing reduces the concentration of point defects that were present in the as-grown alloy.

5.8 Trace Impurity Analyses

Samples were submitted to two testing laboratories, identified here as Lab A and Lab B, for trace impurity analyses. Lab A did a mass spectrographic analysis of a single-crystal slice 16ECI. Both laboratories performed atomic emission spectrographic analyses on identically-prepared, pulverized, specimens 16DAK and 16DCF. Lab B also performed atomic emission spectrographic analyses on pulverized specimens 16DAF, 16EC3, 16EE6, and 16ET2.

The analyses are tabulated in Table 11. Because of conflicting mass lines from the major elements Hg, Cd, and Se, the mass spectrograph could not be analyzed for the elements Er, Eu, Fe, Gd, Ir, Mn, Os, Pd, Pt, Re, Rh, Ru, Si, Sm, Tb, Th, Tm, U, or V. The mass spectrographic analysis showed that the O, S, and Te impurity levels are low. The emission spectrographic analyses of 16DAK and 16DCF were significantly different for the two laboratories. Lab B found 7-10 ppm In and 7-10 ppm Ni, and Lab A detected none. Lab A found 2-20 ppm Fe, and Lab B found 0.1 ppm Fe.

The elements used to prepare the alloys had less than 1-5 ppm impurities according to the analysis of the vendor. The major contaminant that could be introduced during reaction and crystal growth of the alloys is Si from the quartz tubing. Some contamination could have been introduced during pulverization of the samples. However, the total impurity content of 30-50 ppm that is indicated by the analyses is unaccountably large, and it is probable that most of the impurities were present in the Hg, Cd, and Se starting materials.

TABLE 11. TRACE IMPURITY ANALYSES OF HgCdSe 16D AND 16E.
NUMBERS ARE PARTS PER MILLION BY WEIGHT. NO ENTRY
MEANS ELEMENT NOT DETECTED.

Element	Mass spectrographic analysis	Atomic emission spectrograph analysis							
	Lab A	Lab A	Lab B	Lab A	Lab B	Lab B			
	16EC1	16 DAK	16 DAK	16 DCF	16 DCF	16 DAF	16 EC3	16 EE6	16 ET2
Ag	0.5			<1		1		0.7	
Al	10	3.7	5	5-10	5	5	10	10	10
As	0.2								
Au	<0.2								
B	<0.05								
Ba	<0.1								
Be									
Bi	<0.2								
Br	<1								
C	(2)								
Ca	5						1	1	2
Ce	<0.1								
Cl	0.1								
Co	<0.05								
Cr	0.2								
Cs	<0.1								
Cu	0.5	<1	0.3	1.3	0.1	0.5	0.5	0.3	1
Dy	<2								
F	<2								
Fe	*	2	0.1	20	0.1	0.1	0.5	0.5	0.5
Ga	<0.5								
Ge	<0.1								
Hf	<0.5								
Ho	<1								
I	<0.1								
In	<0.5		7		10	20	20	5	20
K	10								
La	<0.1								
Li	<0.01								
Lu	<0.2								
Mg	2	2	6	2	7	5	8	4	10
Mn	*			3					
Mo	1								
N	(2)								
Na	1								
Nb	<0.5								
Nd	<0.5								
Ni	<0.2			7-10					
O	(0.2)								
P	<0.1								
Pb	<0.5			3.5					
Pr	<0.1								
Rb	<0.1								
S	5								
Sb	<0.2	5	20	5	7	20	10	40	30
Sc	<0.02								
Si	*	5-7	2	5-7	2	3	5	5	5
Sn	0.5								
Sr	<1								
Ta	<0.2								
Te	<0.2								
Ti	0.2								
Tl	<1								
W	<2								
Y	<0.5								
Yb	<2								
Zn	0.2								
Zr	<2								

* Element not analyzable by mass spectrography because of conflicting Hg, Cd, or Se mass lines

6. ELECTRICAL PROPERTIES OF $\text{Hg}_{1-x}\text{Cd}_x\text{Se}$ ALLOYS

6.1 Galvanomagnetic Measurements

$\text{Hg}_{1-x}\text{Cd}_x\text{Se}$ alloys are invariably n-type, with conduction electron concentrations from 3×10^{18} electrons/cm³ in as-grown HgSe ($x = 0$) to as low as 1.3×10^{16} electrons/cm³ in as-grown alloys with $x \leq 0.4$. Annealing the alloys in Hg vapor causes an increase in the electron concentration, and annealing in vacuum decreases the electron concentration. The conduction electrons are apparently a result of Hg in excess of stoichiometry.

Galvanomagnetic measurements were made to determine the temperature dependences of the conduction-electron concentration, n , and electron mobility, μ_n , of $\text{Hg}_{1-x}\text{Cd}_x\text{Se}$ specimens with various x -values. These quantities are calculated from the measured Hall coefficient, R_H , and the electrical conductivity, σ , in accordance with the relations

$$n = -1/R_H e \quad (38)$$

and

$$\mu_n = R_H \sigma, \quad (39)$$

where e is the magnitude of the charge of an electron.

Most of the electrical conductivity and Hall coefficient measurements were made on circular or irregularly-shaped slices of single crystals by the method of van der Pauw²³. In some cases, rectangular parallelepipeds were cut from crystal slices for the electrical measurements, and these typically measured $1 \times 1 \times 10$ mm.

Potential and Hall-voltage leads were 0.05 mm diam Pt wires, which were spark-welded to the samples. Current leads to the rectangular bars were indium-soldered to the ends of the samples.

The samples were ground, polished, and etched before the electrical leads were attached. The etching was done by immersing the samples in a solution of 1% Br_2 in methanol and then rinsing repeatedly in a 50% ethanol, 50% benzene solution.

The electrical resistivity, Hall coefficient, conduction-electron concentration, and electron mobility at 4.2, 80, and 300 K are listed in Table 12 for $\text{Hg}_{1-x}\text{Cd}_x\text{Se}$ crystals that had x-values from 0.15 to 0.60. Also listed in this table are the electrical measurement technique for each sample, the specimen annealing history, the specimen thickness, and the mole fraction CdSe as determined from the mass density measurements.

The temperature dependences from 4.2 to 300 K of the electrical resistivity, conduction-electron concentration, and electron mobility for the samples listed in Table 12 are shown in Figures 29-66.

The extrinsic electron concentration in most of the samples is too high for the thermal excitation of electrons from the valence band to cause a significant temperature dependence of the electron concentration. The temperature dependence of the electron concentration can be calculated if the Kane energy-band model for InSb ²⁵ is assumed to be valid for the $\text{Hg}_{1-x}\text{Cd}_x\text{Se}$ alloys and if the energy gap, E_G , is assumed to vary linearly with x. The small temperature dependence of n for 16EC8 and 16EC12, Figures 30 and 32, is in accord with that calculated from Kane's model.

For $\text{Hg}_{1-x}\text{Cd}_x\text{Se}$ crystals with large x, for which the energy gap is large, the electron concentration as a function of temperature sometimes exhibits a minimum, as in the case of 33AT1 in Figure 66. Such behavior can be explained only if there are both acceptor and donor states lying between the valence-band and conduction-band energies.

TABLE 12 RESULTS OF GALVANOMAGNETIC MEASUREMENTS AT 4.2, 80, AND 300 K ON Hg_{1-x}Cd_xSe CRYSTALS

Hg _{1-x} Cd _x Se sample no.	Mole fraction of CdSe, x	Thickness (μm)	Measurement technique*	Electrical resistivity, ρ (μΩ-cm)			Hall coefficient, -R _H (cm ³ /C)			Conduction-electron concentration, n (10 ¹⁶ cm ⁻³)			Electron mobility, μ _n (m ² /V-s)			Comments**
				4.2 K	80 K	300 K	4.2 K	80 K	300 K	4.2 K	80 K	300 K	4.2 K	80 K	300 K	
16EC8	0.153	400	V	785	1 870	18 600	213	213	116	2.94	2.94	5.37	27.1	11.4	0.628	VA 48 h @ 230°C
16EC12	0.153	393	V	704	1 260	11 700	111	109	82.8	5.65	5.71	7.55	15.7	8.67	0.707	VA 288 h @ 203°C
16DAH	0.162	147	V	273	432	3 790	38.6	36.3	32.2	16.2	17.2	19.4	14.1	8.41	0.848	AG
16EB12	0.194	727	V	—	3 700	35 200	—	218	185	—	2.87	3.38	—	5.88	0.524	VA 48 h @ 239°C
16EB12S	0.194	691	C	1 180	2 380	19 700	146	144	133	4.29	4.35	4.70	12.3	6.05	0.675	VA 48 h @ 239°C
16EB7	0.207	1035	V	3 350	6 310	50 800	255	255	231	2.45	2.45	2.70	7.62	4.04	0.455	VA 48 h @ 239°C
16EB7S	0.207	750	C	4 060	7 580	49 300	214	212	197	2.92	2.95	3.17	5.27	2.80	0.399	VA 48 h @ 239°C
16DCD	0.209	132	V	658	905	3 240	11.9	11.9	11.9	52.4	52.4	52.4	1.81	1.32	0.369	AG
24AC15	0.216	581	V	2 630	6 080	54 300	257	256	231	2.43	2.44	2.71	9.79	4.20	0.425	VA 142 h @ 232°C
16EB4.1	0.225	380	V	—	—	3 180	—	—	11.7	—	—	53.3	—	—	0.368	AG
16ED4.2	0.225	380	V	—	6 640	50 400	—	210	189	—	2.98	3.30	—	3.16	0.375	VA 48 h @ 239°C
16EA6	0.228	104	V	3 310	5 950	36 700	167	167	150	3.75	3.75	4.18	5.04	2.80	0.407	VA 48 h @ 239°C
24AB14	0.251	20	V	1 430	2 590	17 500	55.8	51.2	45.3	11.2	12.2	13.8	3.91	1.98	0.259	VA 93 h @ 240°C
24AC13	0.297	583	V	18 100	27 600	175 000	492	492	492	1.27	1.27	1.27	2.73	1.79	0.282	AG
24AB16.1	0.326	8	V	5 630	8 240	25 100	63.2	61.3	40.9	9.89	10.2	15.3	1.12	0.742	0.162	VA 93 h @ 240°C
24AB16.2	0.328	8	V	25 200	29 900	72 700	125	131	65.7	5.02	4.77	9.51	0.494	0.438	0.0903	VA 93 h @ 240°C
24AA1.1	0.352	669	V	39 100	48 200	254 000	613	613	613	1.02	1.02	1.02	1.57	1.27	0.240	VA 67 h @ 260°C
24AA1.2	0.352	334	V	58 200	62 000	310 000	741	741	741	0.843	0.843	0.843	1.27	1.20	0.239	VA 67 h @ 260°C, 93 h @ 240°C
24AA1.3	0.352	5	V	39 400	45 600	173 000	386	386	257	1.62	1.62	2.43	0.978	0.847	0.149	VA 67 h @ 260°C, 93 h @ 240°C
24AA3-S	0.366	683	C	3 990	4 780	11 300	20.2	20.2	20.2	31.0	31.0	31.0	0.505	0.421	0.178	AG
33AT1	0.600	400	V	269 000	65 500	132 000	190	182	137	3.29	3.44	4.58	0.0703	0.278	0.104	AG

* V = van der Pauw method, C = conventional method

** AG = as grown, VA = vacuum annealed, SA = Se-vapor annealed

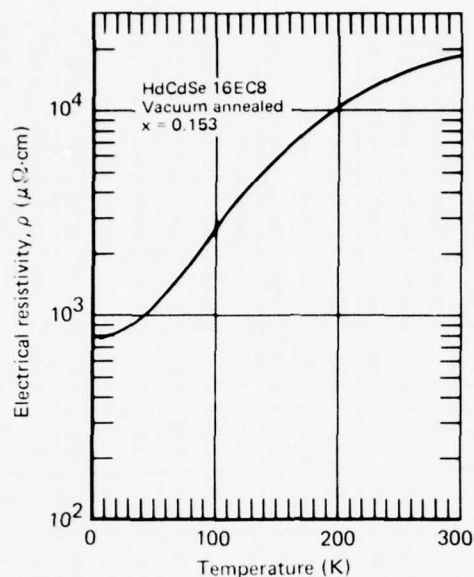


Figure 29 Electrical resistivity as a function of temperature for $\text{Hg}_{0.847}\text{Cd}_{0.153}\text{Se}$ (16EC8) annealed at 239°C in vacuum for 48 h

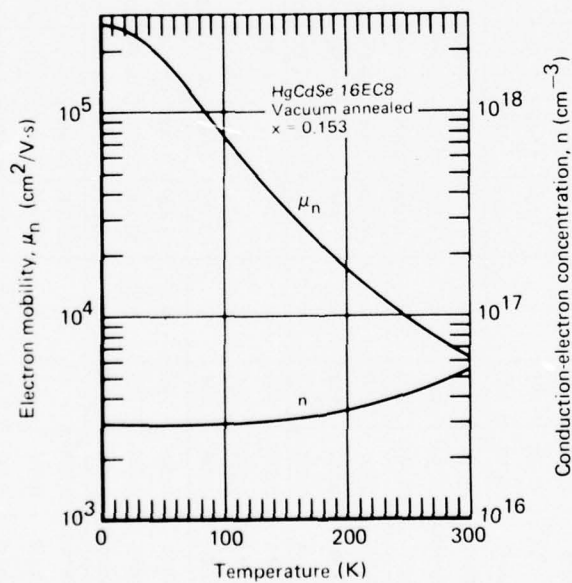


Figure 30 Conduction-electron concentration and mobility as functions of temperature for $\text{Hg}_{0.847}\text{Cd}_{0.153}\text{Se}$ (16EC8) annealed at 239°C in vacuum for 48 h

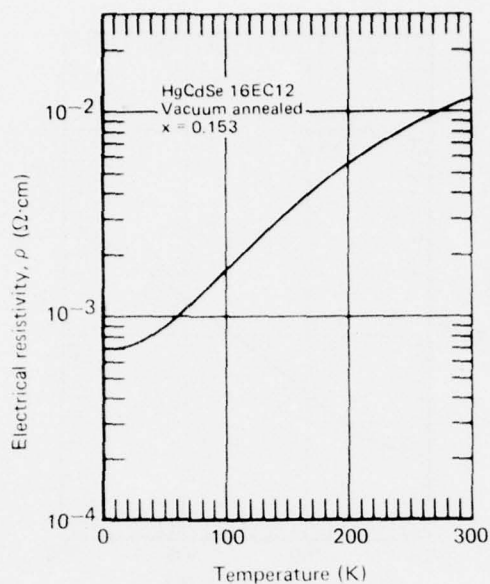


Figure 31 Electrical resistivity as a function of temperature for $\text{Hg}_{0.847}\text{Cd}_{0.153}\text{Se}$ (16EC12) annealed in vacuum at 203°C for 288 h

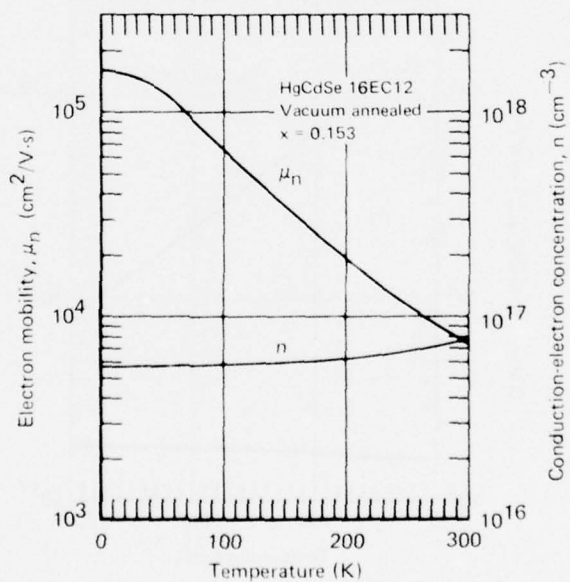


Figure 32 Conduction-electron concentration and mobility as functions of temperature for $\text{Hg}_{0.847}\text{Cd}_{0.153}\text{Se}$ (16EC12) annealed at 203°C in vacuum for 288 h

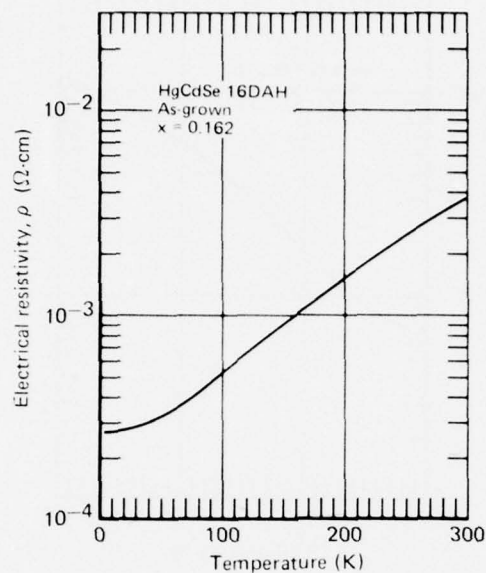


Figure 33 Electrical resistivity as a function of temperature for $\text{Hg}_{0.838}\text{Cd}_{0.162}\text{Se}$ (16DAH) as-grown

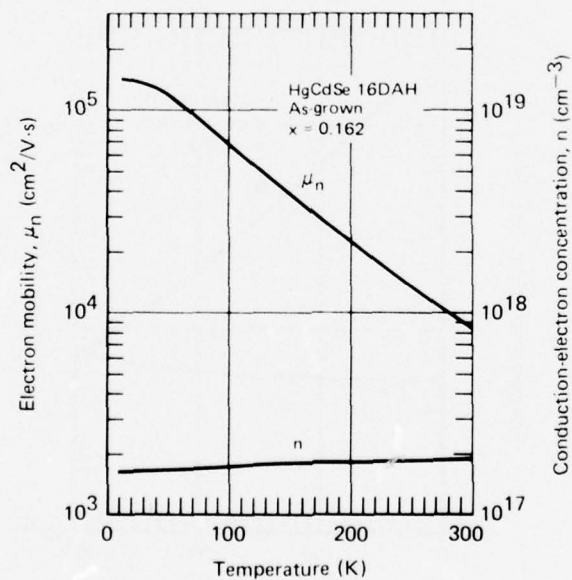


Figure 34 Conduction-electron concentration and mobility as functions of temperature for $\text{Hg}_{0.838}\text{Cd}_{0.162}\text{Se}$ (16DAH) as-grown

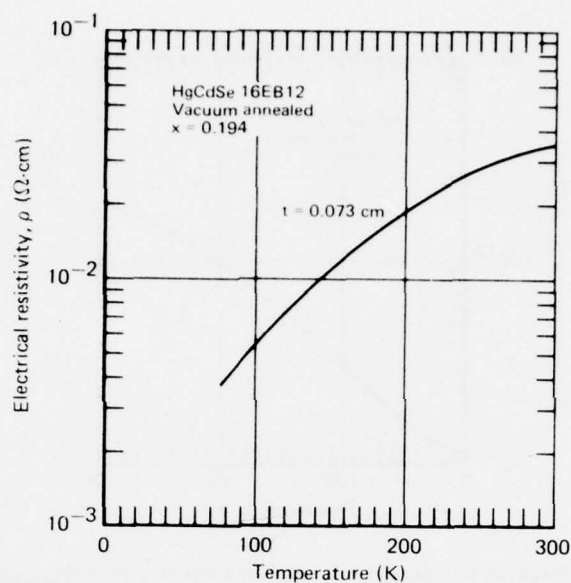


Figure 35 Electrical resistivity as a function of temperature for $\text{Hg}_{0.806}\text{Cd}_{0.194}\text{Se}$ (16EB12) annealed in vacuum at 239°C for 48 h

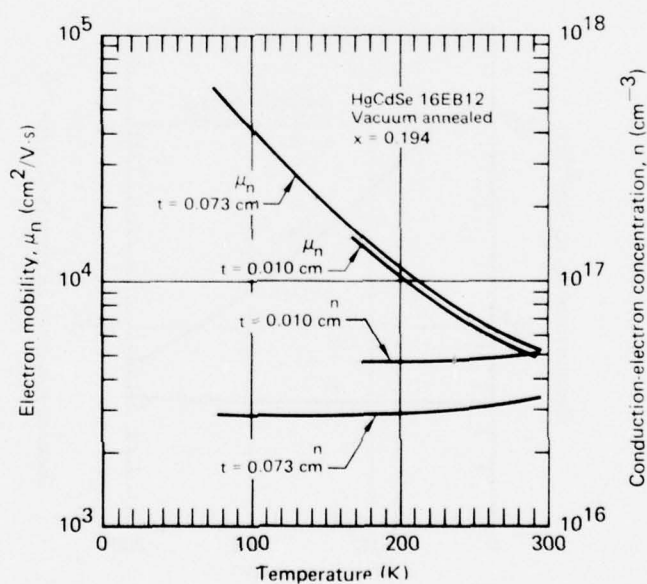


Figure 36. Conduction-electron concentration and mobility as functions of temperature for $\text{Hg}_{0.806}\text{Cd}_{0.194}\text{Se}$ (16EB12) annealed in vacuum at 239°C for 48 h

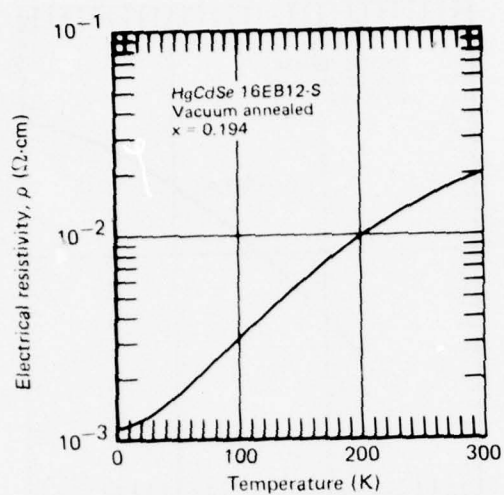


Figure 37 Electrical resistivity as a function of temperature for $\text{Hg}_{0.806}\text{Cd}_{0.194}\text{Se}$ (16EB12-S) annealed in vacuum at 239°C for 48 h

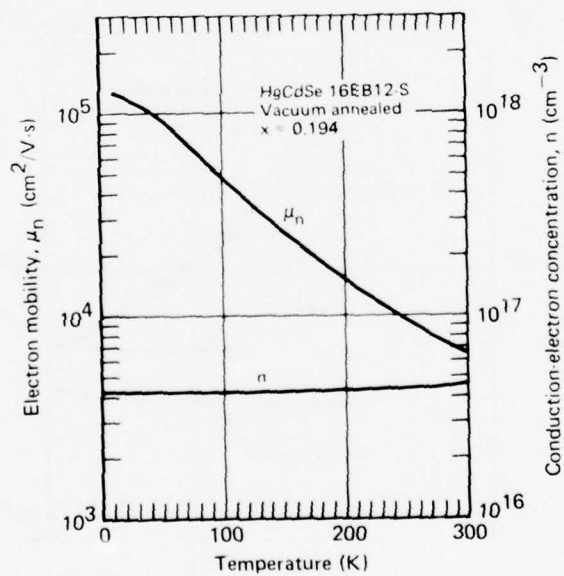


Figure 38 Conduction-electron concentration and mobility as functions of temperature for $\text{Hg}_{0.806}\text{Cd}_{0.194}\text{Se}$ (16EB12-S) annealed in vacuum at 239°C for 48 h

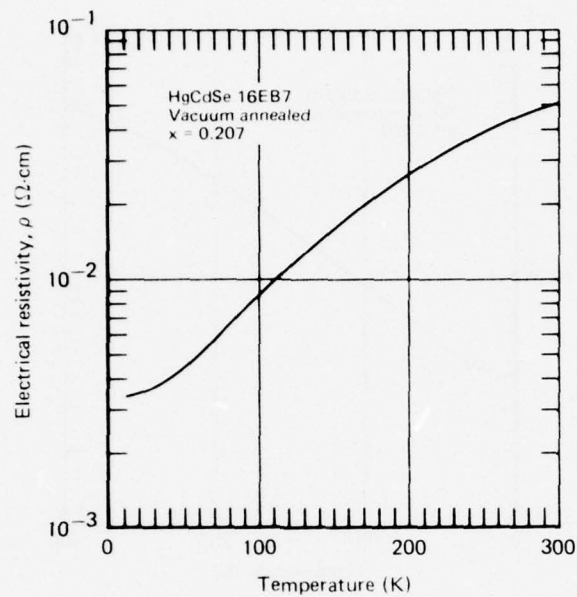


Figure 39 Electrical resistivity as a function of temperature for $\text{Hg}_{0.793}\text{Cd}_{0.207}\text{Se}$ (16EB7) annealed in vacuum at 239°C for 48 h

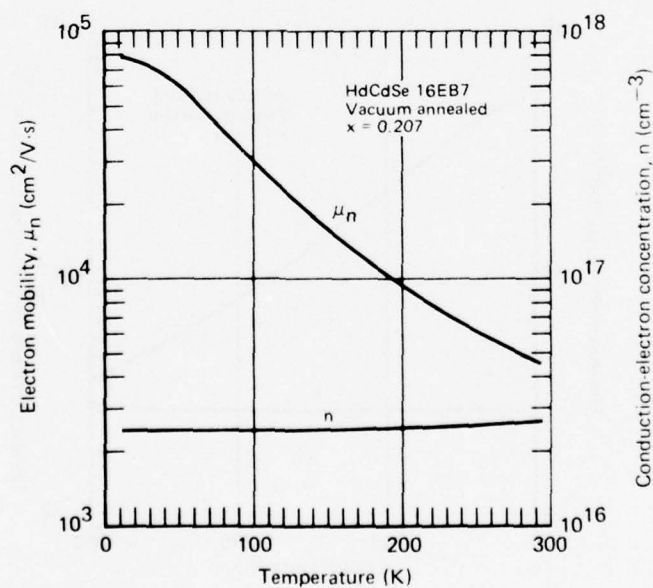


Figure 40. Conduction-electron concentration and mobility as functions of temperature for $\text{Hg}_{0.793}\text{Cd}_{0.207}\text{Se}$ (16EB7) annealed in vacuum at 239°C for 48 h

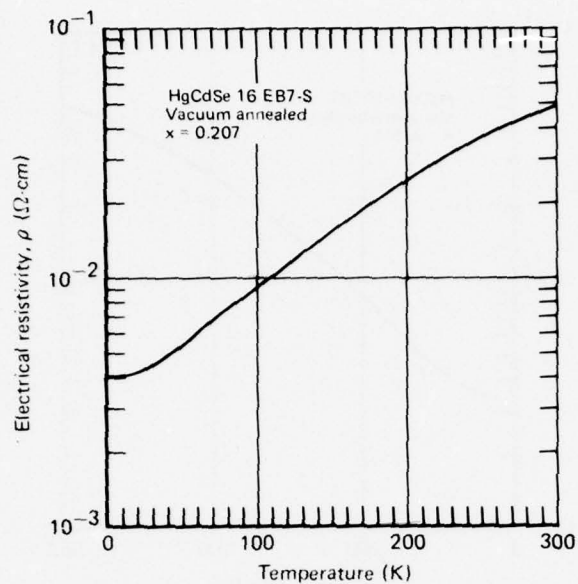


Figure 41 Electrical resistivity as a function of temperature for $\text{Hg}_{0.793}\text{Cd}_{0.207}\text{Se}$ (16EB7-S) annealed in vacuum at 239°C for 48 h

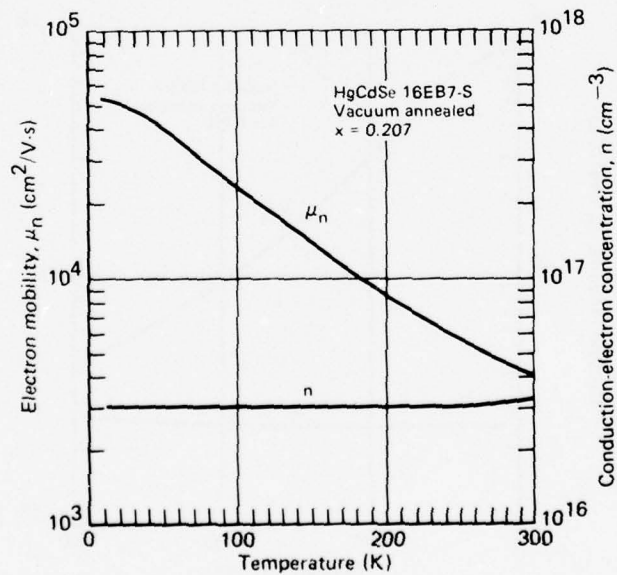


Figure 42. Conduction-electron concentration and mobility as functions of temperature for $\text{Hg}_{0.793}\text{Cd}_{0.207}\text{Se}$ (16EB7-S) annealed in vacuum at 239°C for 48 h

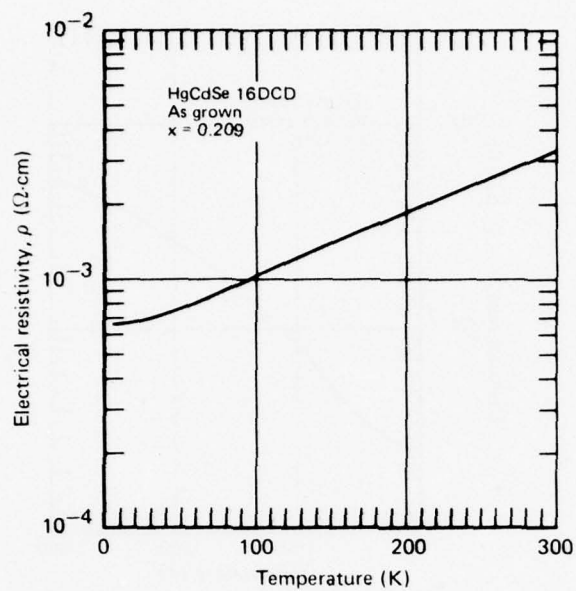


Figure 43 Electrical resistivity as a function of temperature for $\text{Hg}_{0.791}\text{Cd}_{0.209}\text{Se}$ (16DCD) as-grown

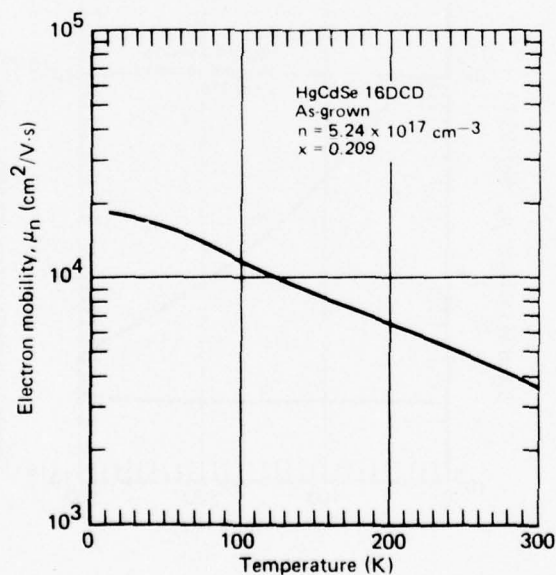


Figure 44. Conduction-electron mobility for $\text{Hg}_{0.791}\text{Cd}_{0.209}\text{Se}$ (16DCD) as-grown

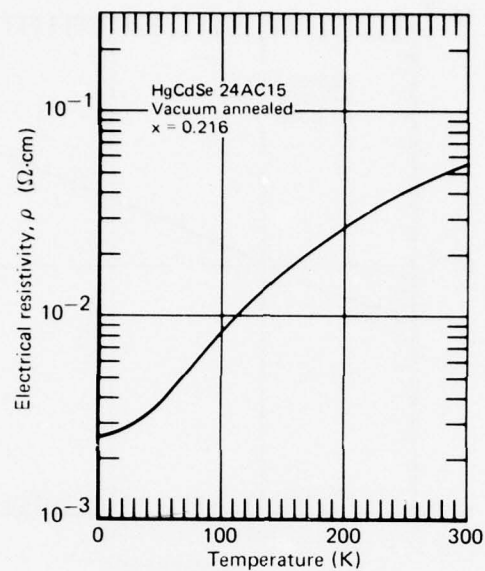


Figure 45 Electrical resistivity as a function of temperature for $\text{Hg}_{0.784}\text{Cd}_{0.216}\text{Se}$ (24AC15) annealed in vacuum at 232°C for 142 h

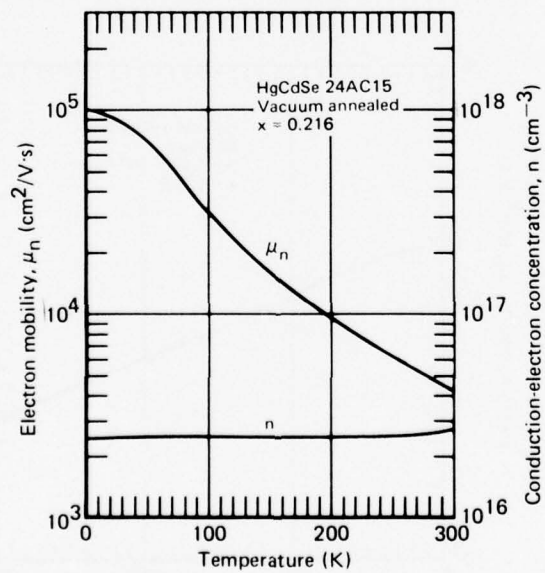


Figure 46 Conduction-electron concentration and mobility for $\text{Hg}_{0.784}\text{Cd}_{0.216}\text{Se}$ (24AC15) annealed in vacuum at 232°C for 142 h

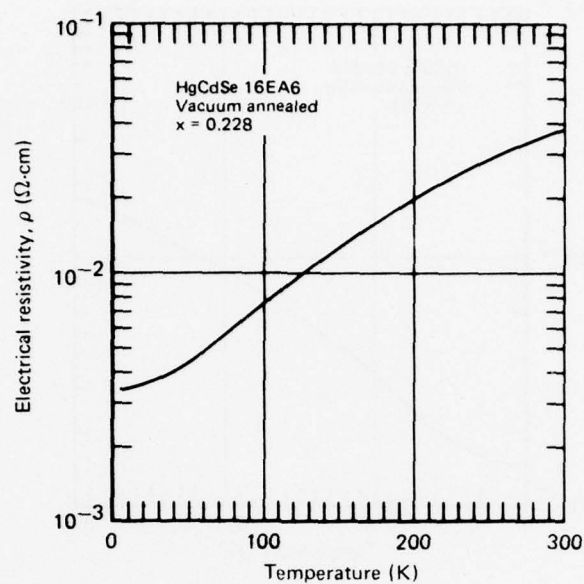


Figure 47 Electrical resistivity as a function of temperature for $\text{Hg}_{0.772}\text{Cd}_{0.228}\text{Se}$ (16EA6) annealed in vacuum at 239°C for 48 h

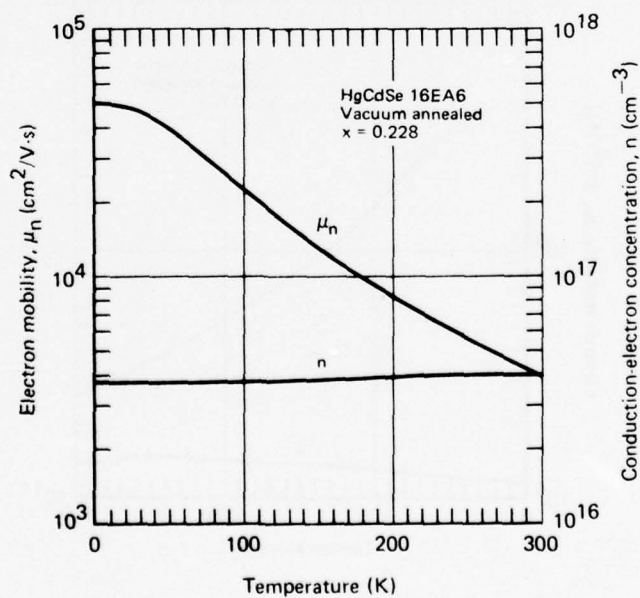


Figure 48 Conduction-electron concentration and mobility as functions of temperature for $\text{Hg}_{0.772}\text{Cd}_{0.228}\text{Se}$ (16EA6) annealed at 239°C in vacuum for 48 h

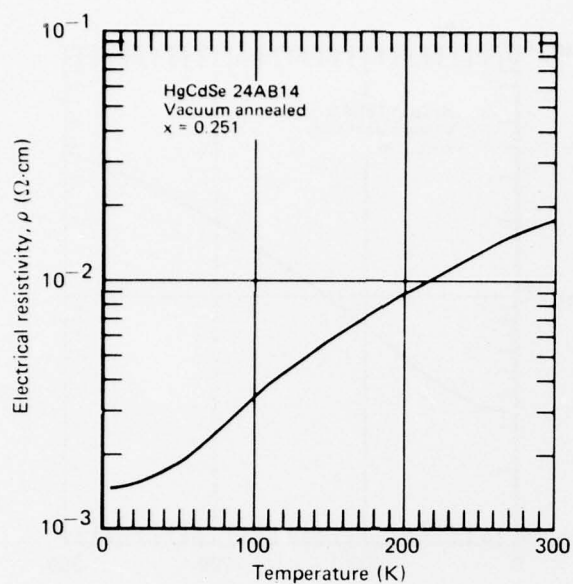


Figure 49 Electrical resistivity as a function of temperature for $\text{Hg}_{0.749}\text{Cd}_{0.251}\text{Se}$ (24AB14) annealed in vacuum at 240°C for 93 h

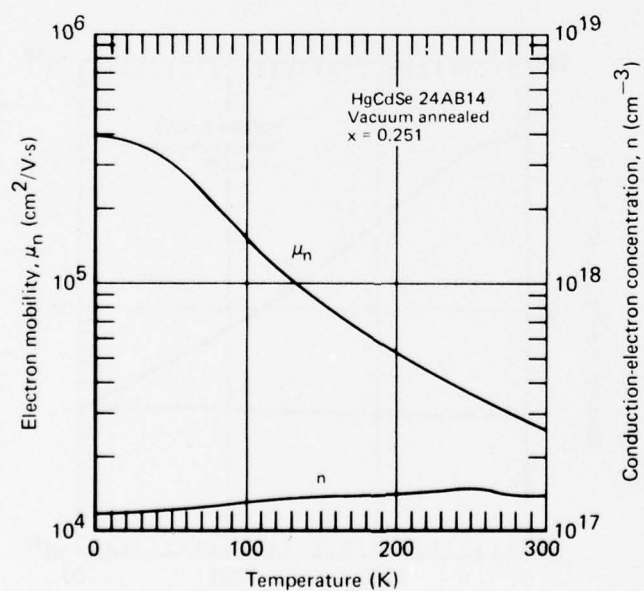


Figure 50 Conduction-electron concentration and mobility as functions of temperature for $\text{Hg}_{0.749}\text{Cd}_{0.251}\text{Se}$ (24AB14) annealed in vacuum at 240°C for 93 h

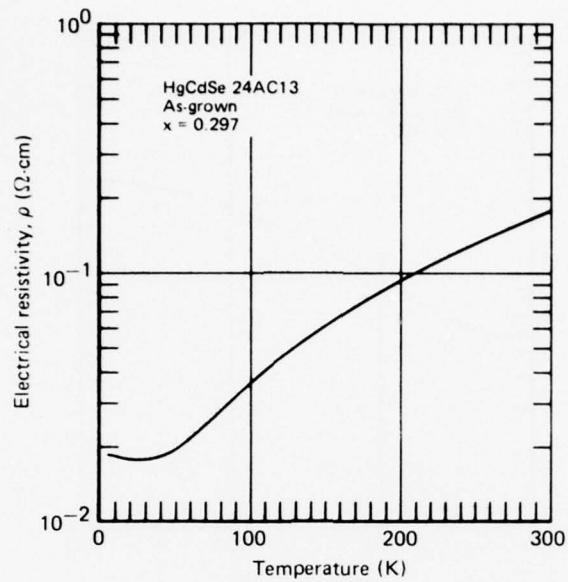


Figure 51 Electrical resistivity as a function of temperature for $\text{Hg}_{0.703}\text{Cd}_{0.297}\text{Se}$ (24AC13) as-grown

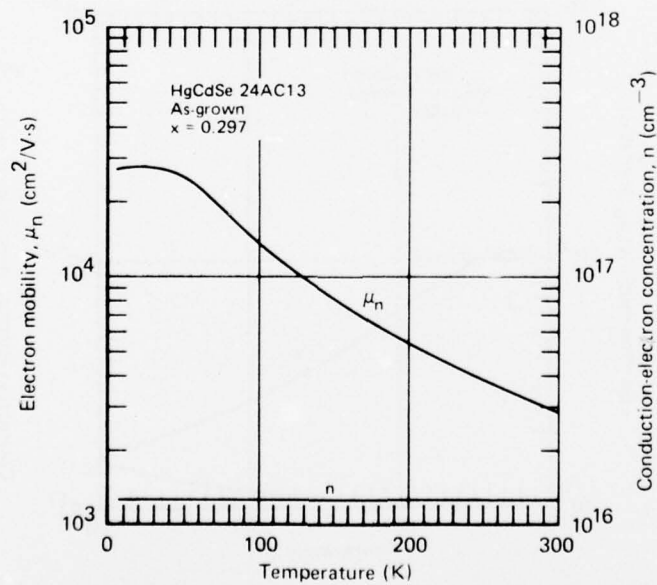


Figure 52 Conduction-electron concentration and mobility as functions of temperature for $\text{Hg}_{0.703}\text{Cd}_{0.297}\text{Se}$ (24AC13) as-grown

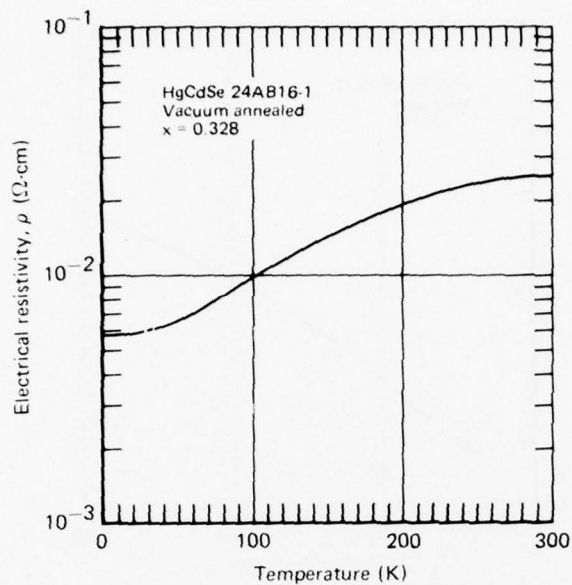


Figure 53 Electrical resistivity as a function of temperature for $\text{Hg}_{0.672}\text{Cd}_{0.328}\text{Se}$ (24AB16-1) annealed in vacuum at 240°C for 93 h

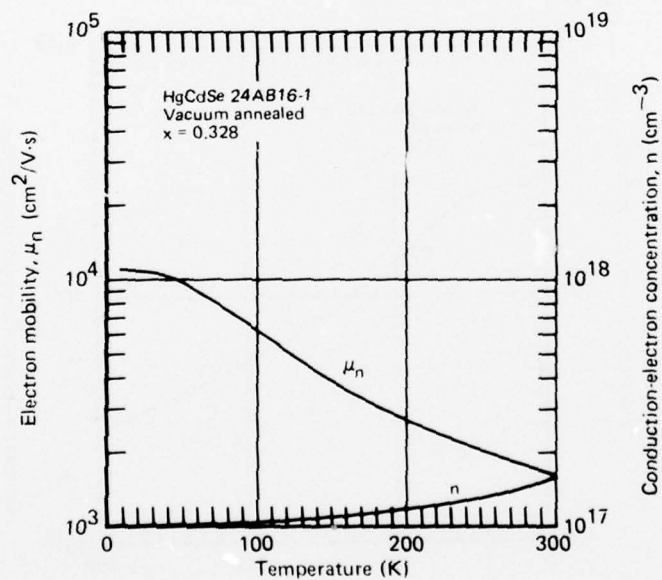


Figure 54 Conduction-electron concentration and mobility as functions of temperature for $\text{Hg}_{0.672}\text{Cd}_{0.328}\text{Se}$ (24AB16-1) annealed in vacuum at 240°C for 93 h

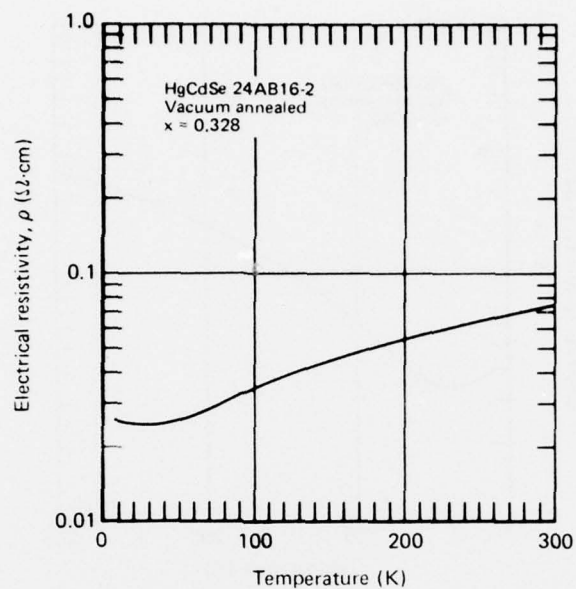


Figure 55 Electrical resistivity as a function of temperature for $\text{Hg}_{0.672}\text{Cd}_{0.328}\text{Se}$ (24AB16-2) annealed in vacuum at 240°C for 93 h

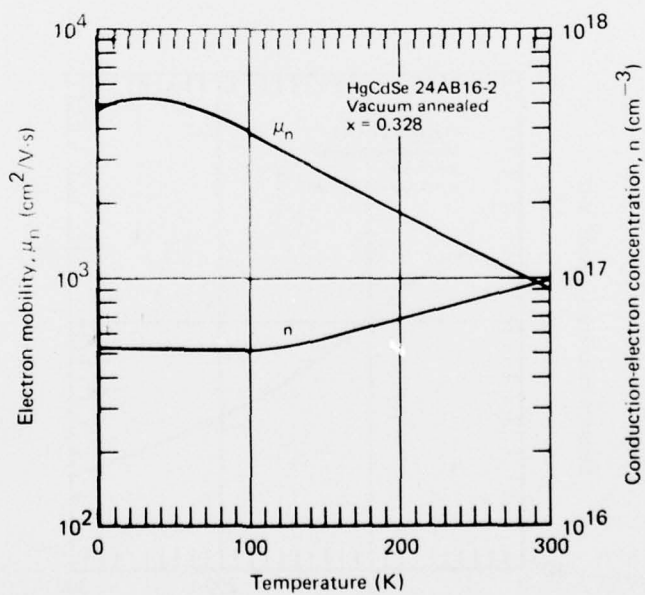


Figure 56 Conduction-electron concentration and mobility as functions of temperature for $\text{Hg}_{0.672}\text{Cd}_{0.328}\text{Se}$ (24AB16-2) annealed in vacuum at 240°C for 93 h; polished after anneal

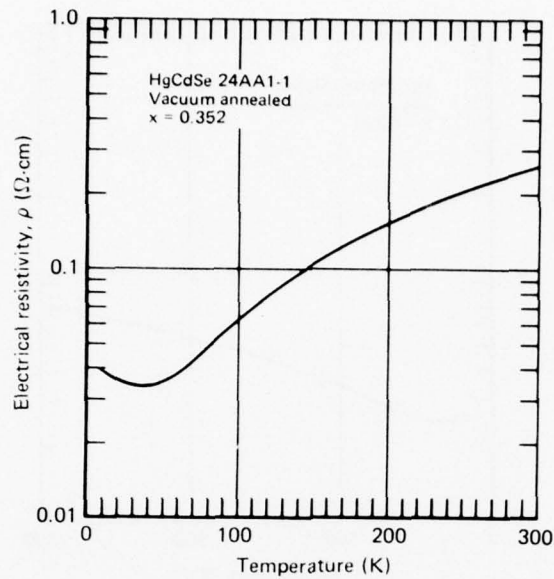


Figure 57 Electrical resistivity as a function of temperature for $\text{Hg}_{0.648}\text{Cd}_{0.352}\text{Se}$ (24AA1-1) annealed in vacuum at 260°C for 67 h

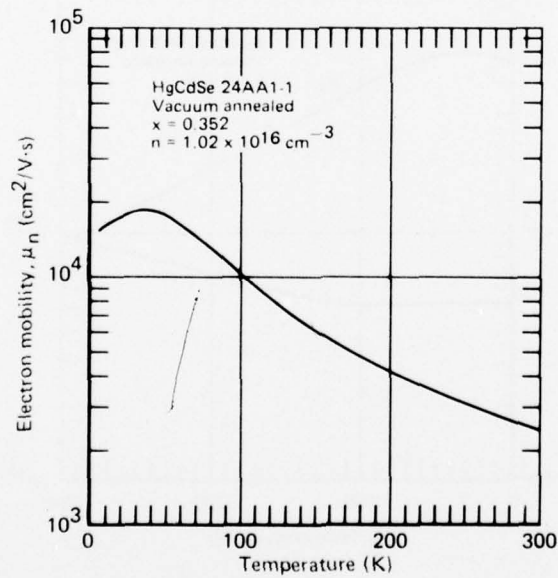


Figure 58 Conduction-electron mobility as a function of temperature for $\text{Hg}_{0.648}\text{Cd}_{0.352}\text{Se}$ (24AA1-1) annealed in vacuum at 260°C for 67 h

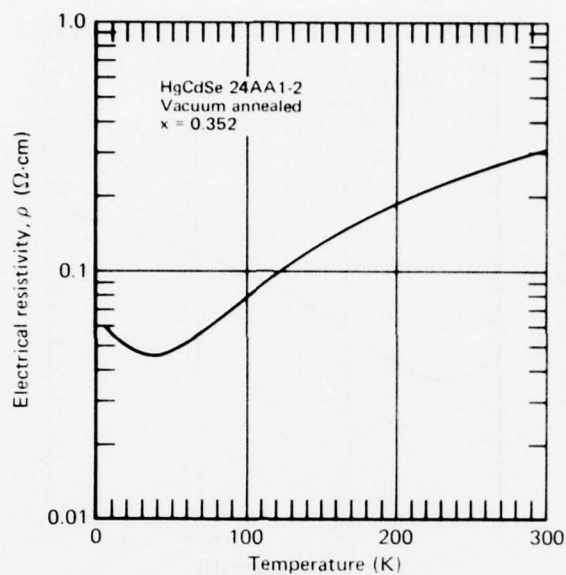


Figure 59 Electrical resistivity as a function of temperature for $\text{Hg}_{0.648}\text{Cd}_{0.352}\text{Se}$ (24AA1-2) annealed in vacuum at 260°C for 67 h and 240°C for 93 h

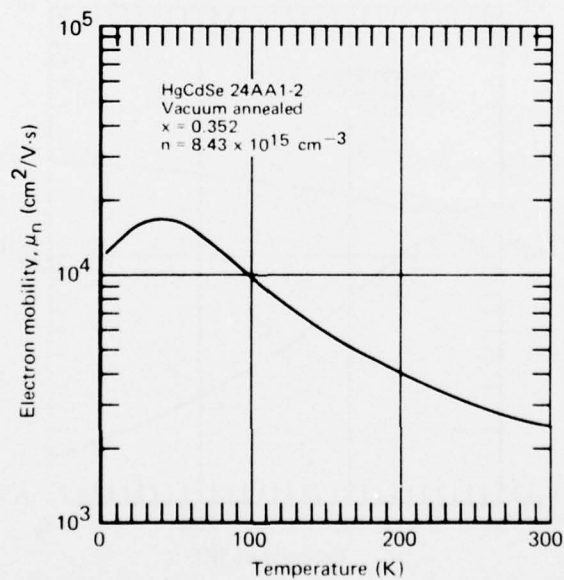


Figure 60 Conduction-electron mobility as a function of temperature for $\text{Hg}_{0.648}\text{Cd}_{0.352}\text{Se}$ (24AA1-2) annealed in vacuum at 260°C for 67 h and 240°C for 93 h

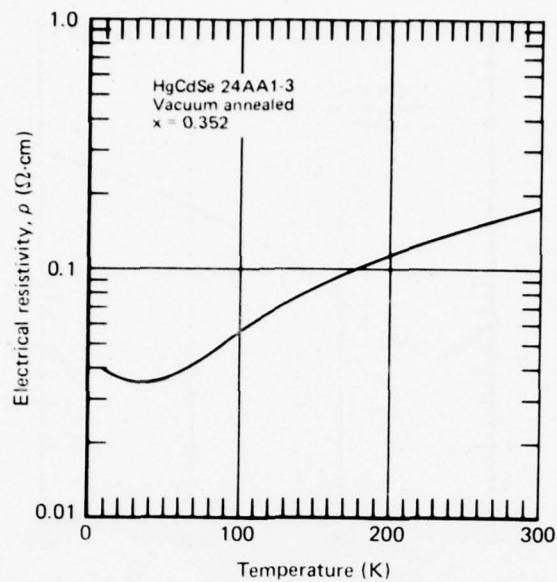


Figure 61 Electrical resistivity as a function of temperature for $\text{Hg}_{0.648}\text{Cd}_{0.352}\text{Se}$ (24AA1-3) annealed in vacuum at 260°C for 67 h and at 240°C for 93 h

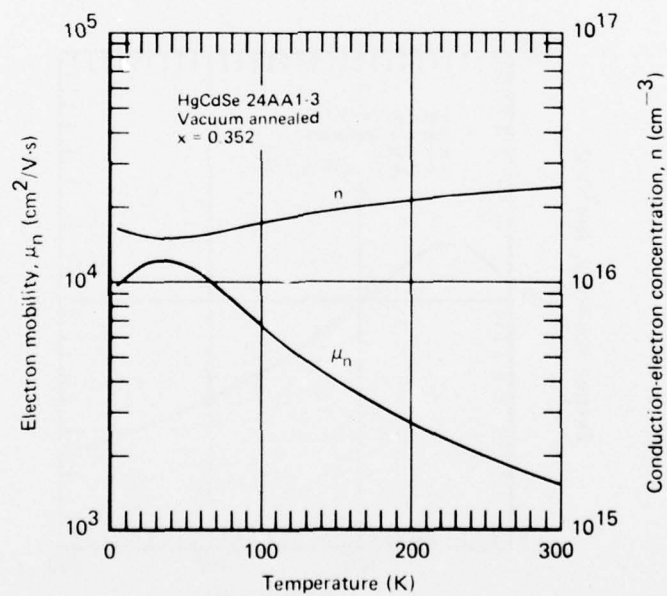


Figure 62 Conduction-electron concentration and mobility as functions of temperature for $\text{Hg}_{0.648}\text{Cd}_{0.352}\text{Se}$ (24AA1-3) annealed in vacuum at 260°C for 67 h and 240°C for 93 h; polished after anneal

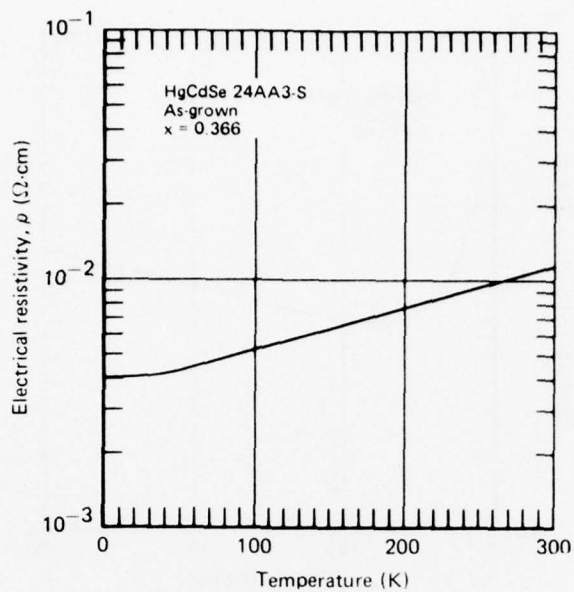


Figure 63 Electrical resistivity as a function of temperature for $\text{Hg}_{0.634}\text{Cd}_{0.366}\text{Se}$ (24AA3-S) as-grown

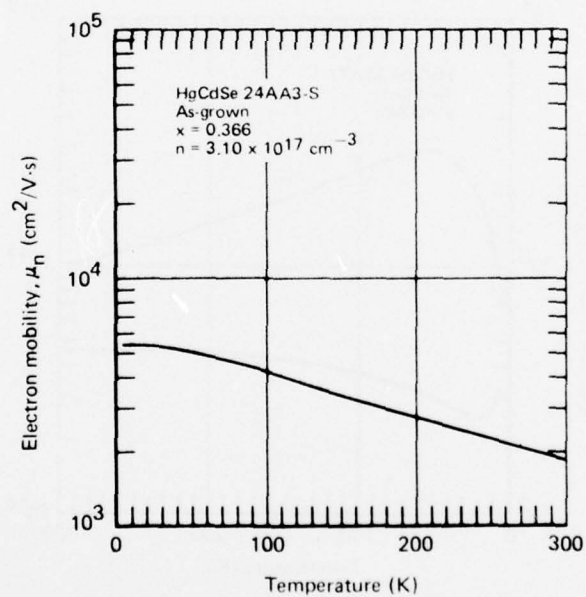


Figure 64 Conduction-electron mobility as a function of temperature for $\text{Hg}_{0.634}\text{Cd}_{0.366}\text{Se}$ (24AA3-S) as-grown

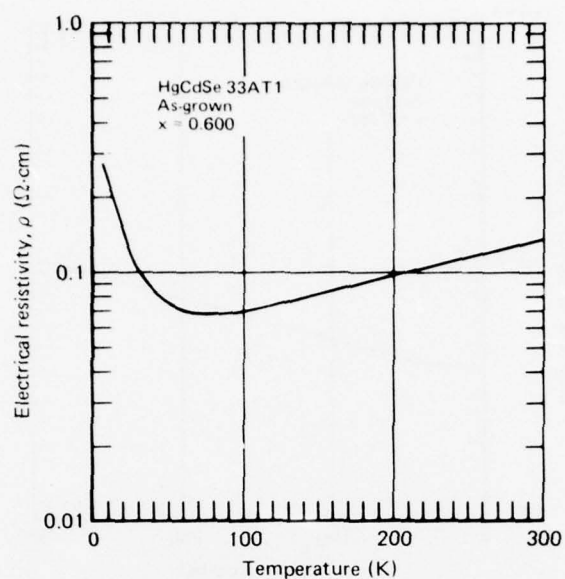


Figure 65 Electrical resistivity as a function of temperature for $\text{Hg}_{0.400}\text{Cd}_{0.600}\text{Se}$ (33AT1) as-grown

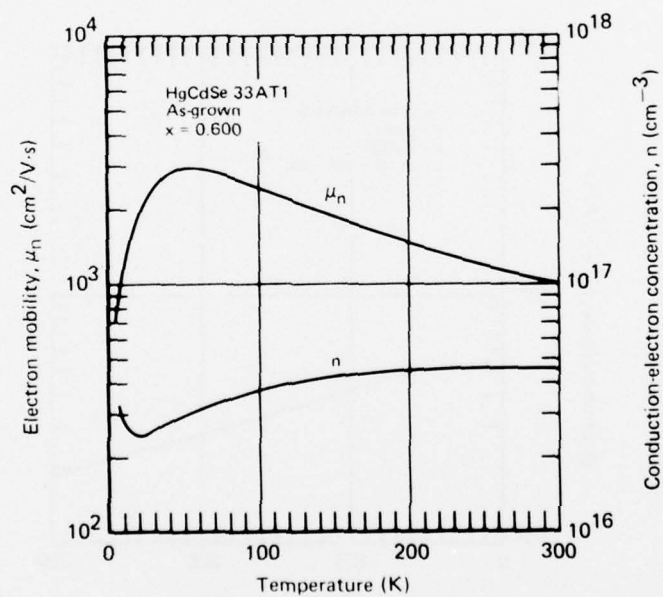


Figure 66 Conduction-electron concentration and mobility as functions of temperature for $\text{Hg}_{0.400}\text{Cd}_{0.600}\text{Se}$ (33AT1) as grown

6.2 Electron Mobility as Function of Alloy Composition

The conduction-electron mobilities at 4.2, 80, and 100 K as functions of x for the $\text{Hg}_{1-x}\text{Cd}_x\text{Se}$ alloys in Table 12 are shown in Figures 67, 68, and 69, respectively.

The conduction-electron mobility is limited at low temperatures by ionized impurities and neutral defects. As the temperature of an alloy is increased above 50 K, the scattering of conduction electrons by optical phonons associated with both Hg and Cd atoms becomes the dominant mobility-limiting factor. Alloy scattering and scattering by acoustic modes also are important at higher temperatures.

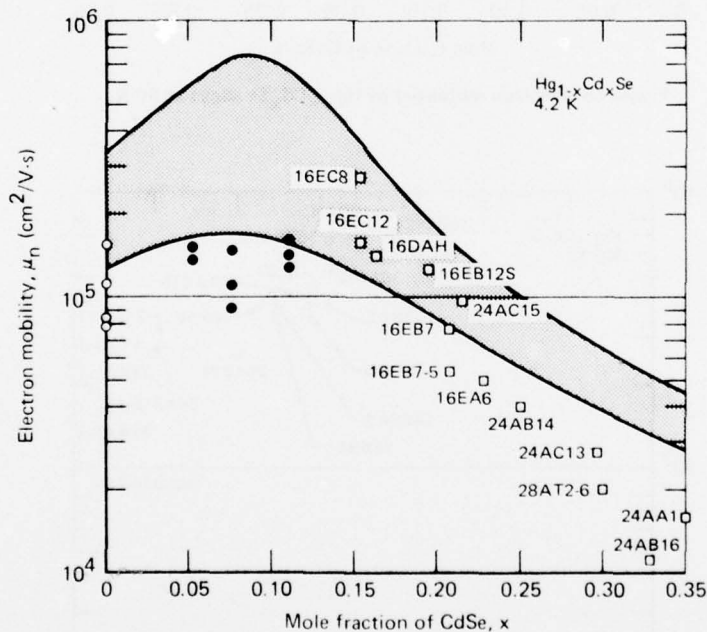


Figure 67 Electron mobilities of $\text{Hg}_{1-x}\text{Cd}_x\text{Se}$ alloys at 4.2 K: (○) Reference 9; (●) Reference 24; (□) this report. Shaded area is calculated range of mobilities.

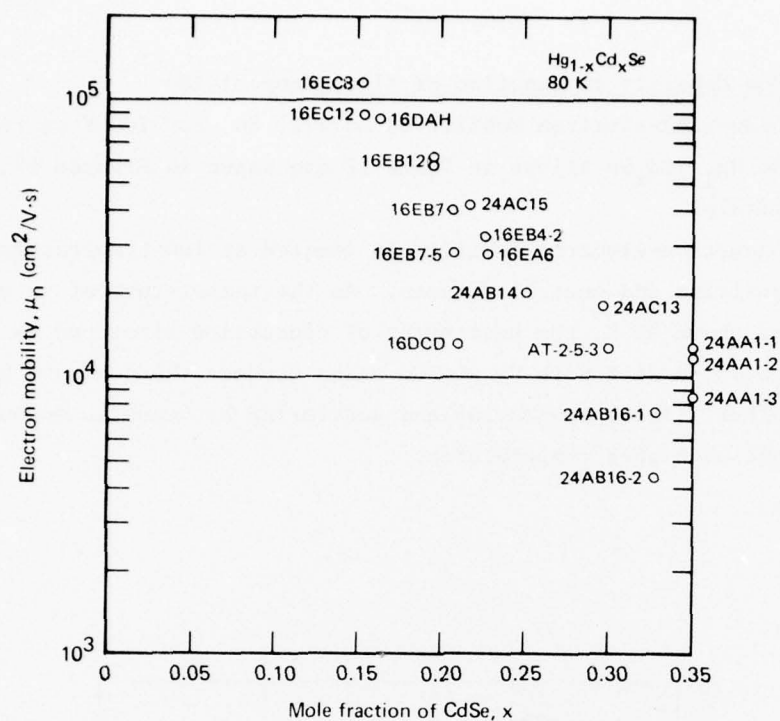


Figure 68 Electron mobilities of $\text{Hg}_{1-x}\text{Cd}_x\text{Se}$ alloys at 80 K

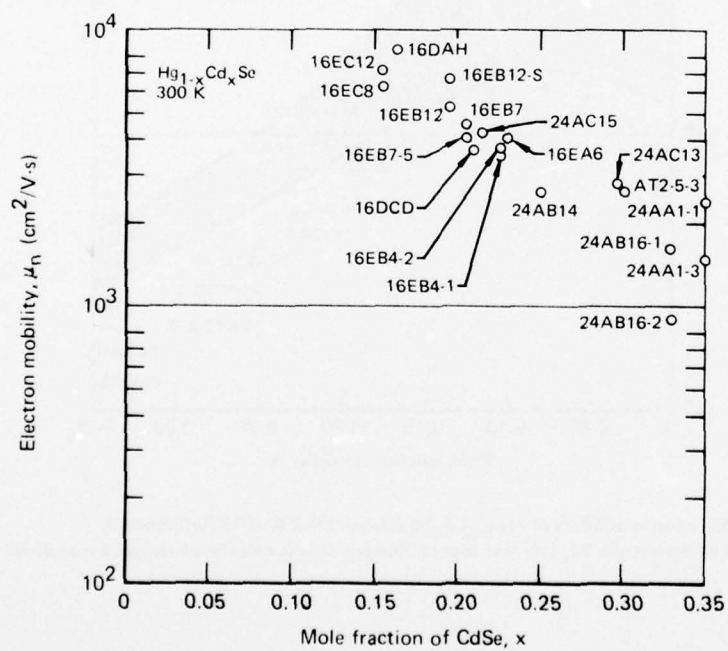


Figure 69 Electron mobilities of $\text{Hg}_{1-x}\text{Cd}_x\text{Se}$ alloys at 300 K

The ionized-impurity limited mobility of the $\text{Hg}_{1-x}\text{Cd}_x\text{Se}$ alloys at 4.2 K was calculated by the method of Reference 9. For these calculations, a relaxation-time approximation was employed, and complete degeneracy of the conduction electrons was assumed. The calculations therefore are valid only for very low temperatures (< 10 K). The expression for the conduction electron mobility is

$$\mu_{nI} = \frac{3\pi\epsilon_0^2 \hbar^3 n}{2N_I e^3 m^{*2} \phi}, \quad (40)$$

where $\epsilon = \epsilon_0$ for $E_G \geq 0$, $\epsilon = \epsilon_0 + (8e^2 m_0^* / \pi \hbar^2 k)$ for $E_G < 0$, k is the wave-number of electrons that have the Fermi energy, and m_0^* is the zone-center effective mass of a conduction electron. The conduction-band symmetry enters into this expression through the scattering function, ϕ , which is given explicitly in Reference 9. The static dielectric constant, ϵ_0 , is assumed to vary linearly between the values of 25.6 for HgSe^{26} and 9.7 for CdSe^{27} . In Equation (40), N_I is the concentration of ionized impurities, which are assumed to be singly ionized, and m^* is the conduction-electron effective mass at the Fermi level. The variation of the energy gap with x is implicit in Equation (40) because of the terms m_0^* and m^* . For the calculation of electron mobilities, E_G was assumed to vary linearly between the values of -0.22 eV for HgSe^{28} and 1.84 eV for CdSe^{29} .

The range of calculated electron mobilities for $\text{Hg}_{1-x}\text{Cd}_x\text{Se}$ alloys having N_I between 3×10^{16} and $3 \times 10^{17} \text{ cm}^{-3}$ is shown by the shaded region in Figure 67. Plotted in Figure 67 are values from Table 12 for the measured mobilities at 4.2 K of $\text{Hg}_{1-x}\text{Cd}_x\text{Se}$ specimens that had electron concentrations between 3×10^{16} and $3 \times 10^{17} \text{ cm}^{-3}$. Also shown in Figure 67 are mobilities at 4.2 K measured by Lehoczky, Broerman, Whitsett, and Nelson⁹ and by Stankiewicz, Girit, and Dobrowski²⁴ for HgSe crystals that had electron concentrations between 3×10^{16} and $3 \times 10^{17} \text{ cm}^{-3}$. The measured mobilities systematically fall below the calculated range as x increases. This departure of the measured mobilities from the calculated range implies that electron-scattering agents other than ionized impurities may be important in the $\text{Hg}_{1-x}\text{Cd}_x\text{Se}$ alloys, although the discrepancy may be partly caused by different behaviors of ϵ_0 and E_G than were assumed in the calculations and by the Hg-Cd disorder in the crystal lattice.

7. INFRARED ABSORPTION AND DEPENDENCE OF ENERGY

GAP ON COMPOSITION OF $\text{Hg}_{1-x}\text{Cd}_x\text{Se}$ ALLOYS

7.1 Infrared Optical Absorption

The dependence of the fundamental energy gap on composition and temperature were determined from infrared transmission measurements on $\text{Hg}_{1-x}\text{Cd}_x\text{Se}$ alloys with x-values from 0.153 to 0.366. The functional relation between energy gap, composition, and temperature can be used to calculate the compositional dependence of the intrinsic carrier concentration and the radiative and Auger lifetimes, on which the responsivity and noise of a detector element are dependent. From such calculations, the ultimate detector performance that can be achieved with this alloy system can be predicted as a function of wavelength, temperature, and background-radiation flux.

Optical absorption occurs when an incident photon has sufficient energy to excite an electron from a filled valence-band state into an empty state in the conduction band. If the electron energy band-gap of an alloy crystal is denoted by E_G and the Fermi energy of the conduction electrons is denoted by E_F , the condition for a photon of energy E to be absorbed in the crystal at 0 K is $E \geq E_F + E_G$. Infrared radiation with photon energies less than $E_F + E_G$ (or with wavelengths greater than $hc/(E_F + E_G)$, where h is Planck's constant and c is the speed of light) will be transmitted through the material. On this basis, the infrared transmittance spectra will be a step-function curve, having finite values for $E < E_F + E_G$ and being zero for $E \geq E_F + E_G$. However, even in ideal materials, there are band-edge tail effects, which stretch the wavelength interval of transition from finite to zero transmittance. Furthermore, as the temperature and the conduction-electron concentration are increased, the departure from degeneracy of the electrons causes further rounding of the infrared transmittance transition-region. In the specific case of the $\text{Hg}_{1-x}\text{Cd}_x\text{Se}$ alloys, slight inhomogeneities in the composition will cause a range of values of E_G in a single specimen, and this will additionally round the transmission edge. To quantitatively separate the various factors which affect the transmittance curve, it is necessary to select samples that are homogeneous and to perform detailed analyses to separate the various contributions to the optical absorption.

7.2 Preparation of Samples for Optical Measurements

Samples for this study were cut from single-crystal HgCdSe ingots 16E and 26A. The 1-mm thick samples were annealed in vacuum at temperatures from 200 to 250°C for periods up to 200 h. The annealing improved the uniformity of the material and reduced the extrinsic electron concentration. Equal amounts of material were ground and polished from each side of a sample until its thickness was 400 - 500 μm . At this thickness the compositional uniformity of each slice could be assessed easily by the infrared-transmission scanning method described in Section 5.5. Specimens were cut from homogeneous regions of each slice, and their compositions were determined by mass-density measurements. The temperature dependences of the electron concentration and mobility from 4.2 to 300 K were then measured for each sample. Samples that had compositional homogeneity and normal electrical properties were then further reduced in thickness for optical-transmission measurements. For the final grinding and polishing, the specimens were bonded to a polishing holder with a low-temperature thermoplastic, and grinding and polishing were performed in steps with successively finer abrasive grits. The layer thickness removed at each step was 4-10 times the diameter of the abrasive grit used in the preceding step, and the final-step grit was 0.03 μm diam alumina powder. This procedure was used on both sides of the sample, and x-ray topographs and the optical absorption measurements showed that the surface damage was very small. Grinding and polishing must be carefully performed because surface damage can have a significant effect on the shape of the optical-transmission edge, particularly at low absorption-coefficient values. The ratio of final polishing-grit size to sample thickness must be as small as practicable.

The thickness of each sample was measured after its transmission spectra were obtained. A calibrated, electronic, thickness gauge was used to measure the thicknesses, and the accuracy of thickness measurements was $\pm 3\%$ for sample thicknesses between 10 and 100 μm .

7.3 Infrared Transmittance Spectra

The infrared transmittance spectra from 400 to 5000 cm^{-1} wavenumbers (2 to 25 μm wavelengths) were obtained at several temperatures from 5 to 300 K for $\text{Hg}_{1-x}\text{Cd}_x\text{Se}$ specimens that had x-values from 0.153 to 0.366. The spectra are shown in Figures 76-78.

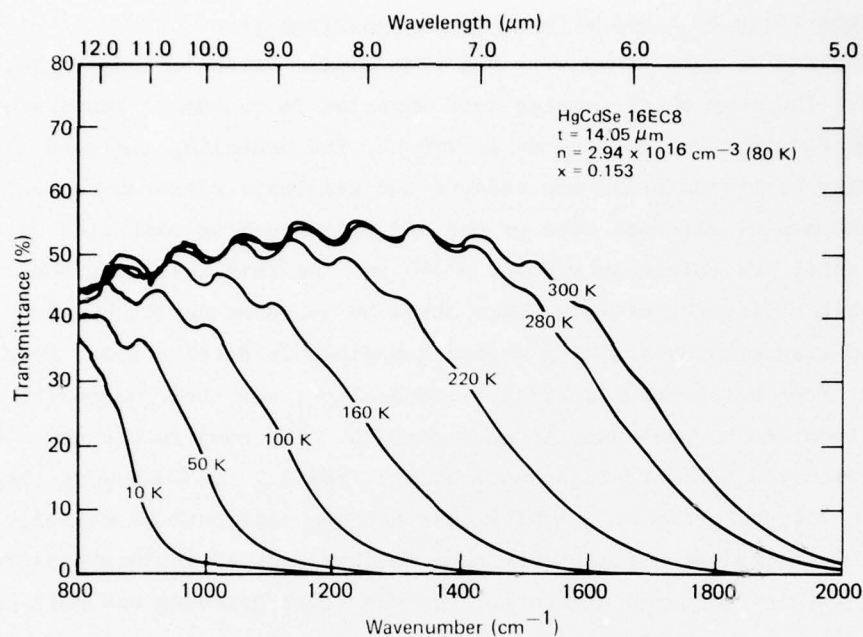


Figure 70 Infrared transmittance spectra at different temperatures for $\text{Hg}_{0.847}\text{Cd}_{0.153}\text{Se}$ (16EC8) annealed in vacuum at 239°C for 48 h

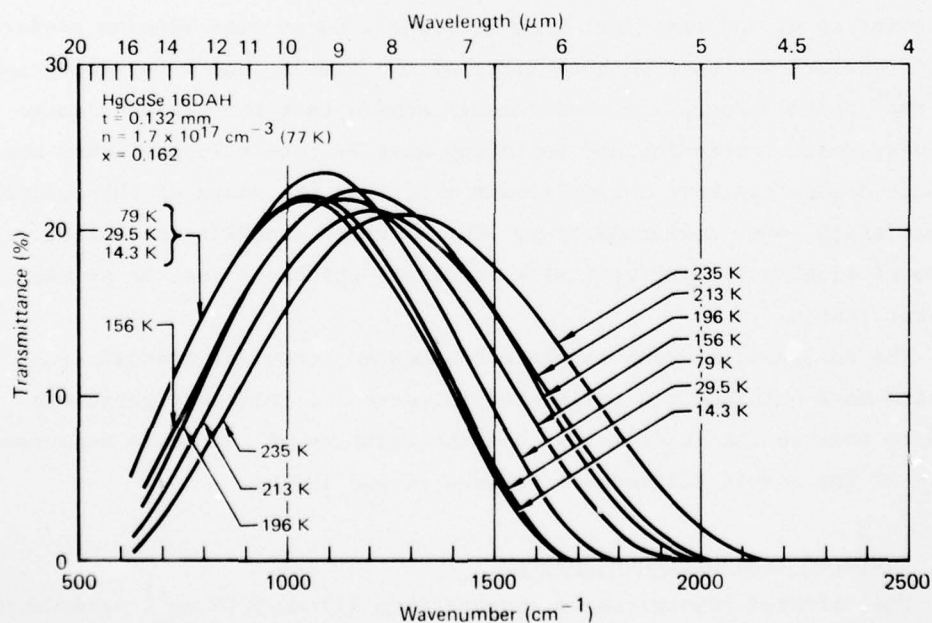


Figure 71 Infrared transmittance spectra at different temperatures for as-grown $\text{Hg}_{0.838}\text{Cd}_{0.162}\text{Se}$ (16DAH)

AD-A041 534

MCDONNELL DOUGLAS RESEARCH LABS ST LOUIS MO
DEVELOPMENT OF THE HGCDSE ALLOY SYSTEM FOR INFRARED SENSOR APPL--ETC(U)
FEB 77 C R WHITSETT, C J SUMMERS

F/G 17/5

F33615-74-C-5167

UNCLASSIFIED

AFAL-TR-76-112

NL

2 OF 2
ADA
041534



END

DATE
FILMED
7-77

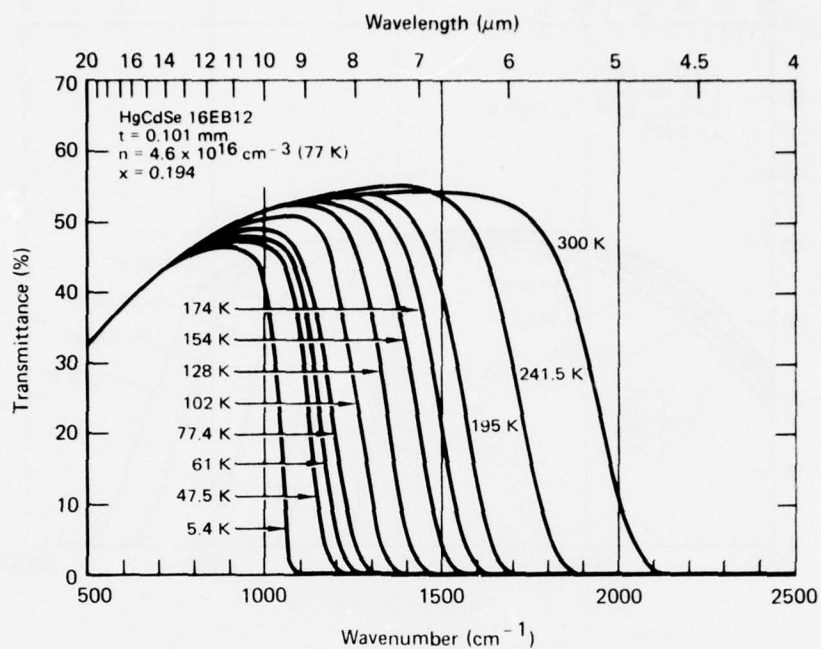


Figure 72 Infrared transmittance spectra at different temperatures for $\text{Hg}_{0.806}\text{Cd}_{0.194}\text{Se}$ (16EB12) annealed at 239°C in vacuum for 48 h

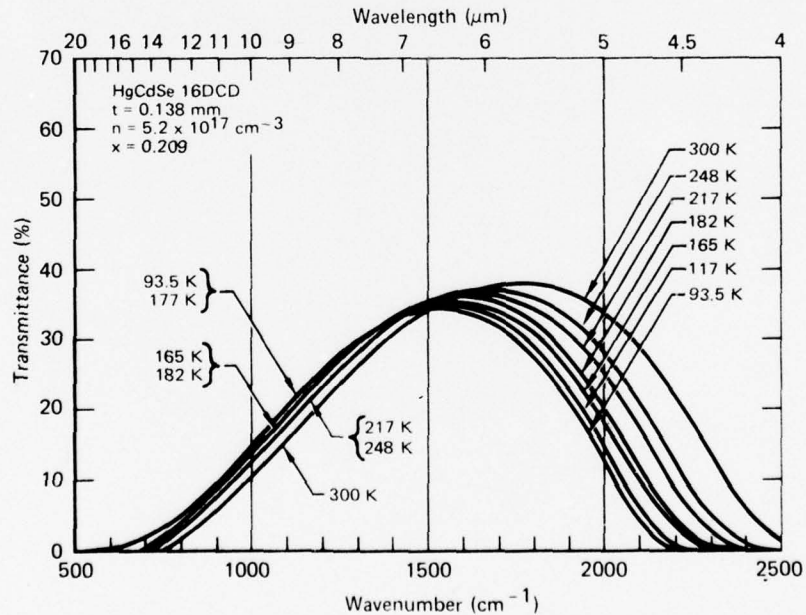


Figure 73 Infrared transmittance spectra at different temperatures for as-grown $\text{Hg}_{0.791}\text{Cd}_{0.209}\text{Se}$ (16DCD)

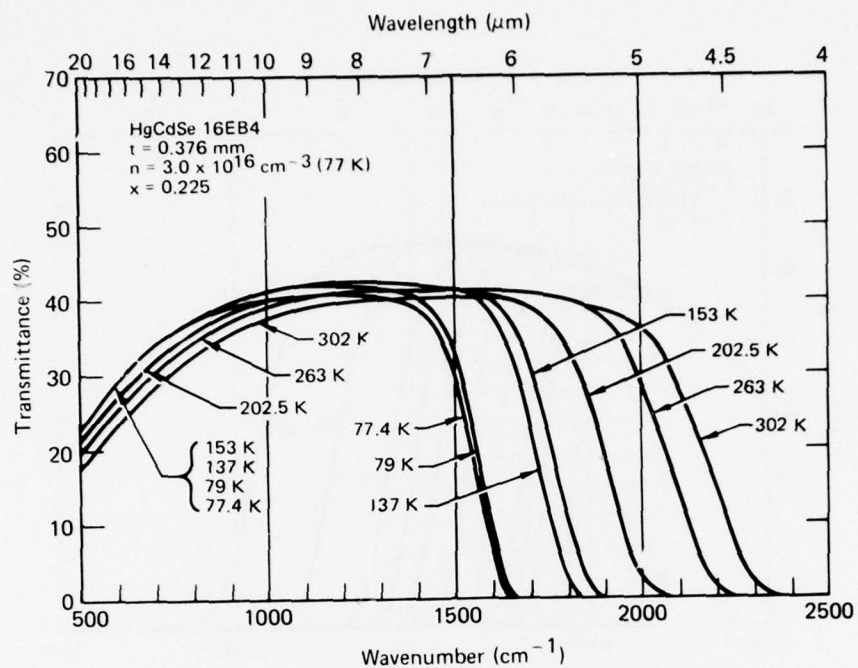


Figure 74 Infrared transmittance spectra at different temperatures for
 $\text{Hg}_{0.775}\text{Cd}_{0.225}\text{Se}$ (16EB4) annealed at 239°C in vacuum for 48 h

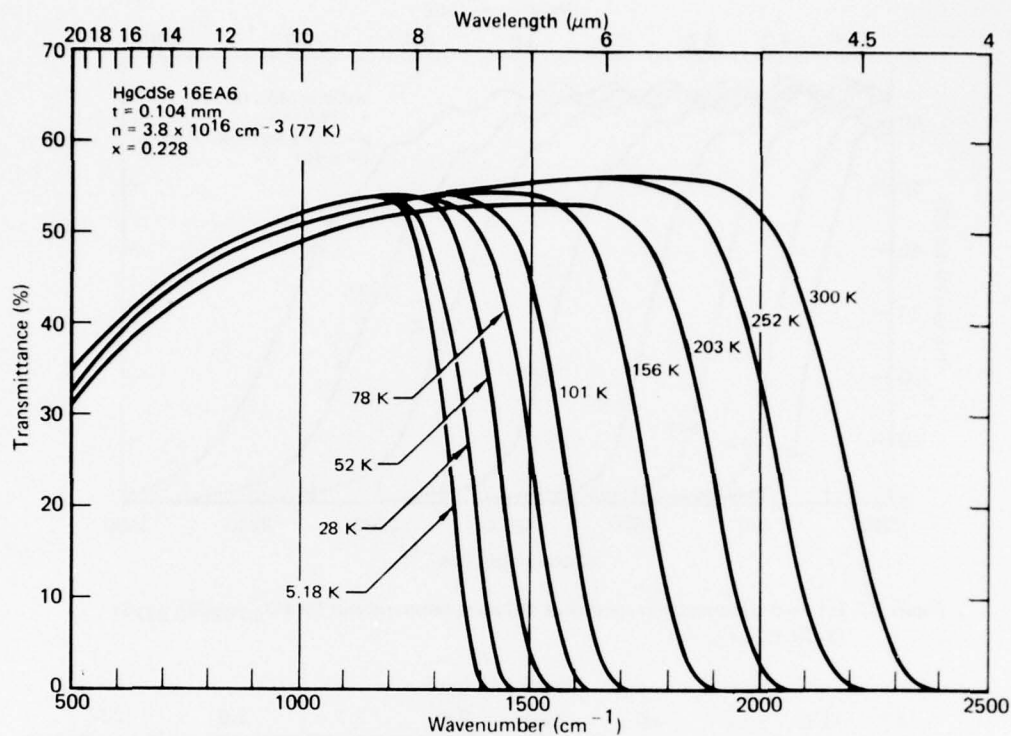


Figure 75 Infrared transmittance spectra at different temperatures for $\text{Hg}_{0.772}\text{Cd}_{0.228}\text{Se}$ (16EA6) annealed at 239°C in vacuum for 48 h

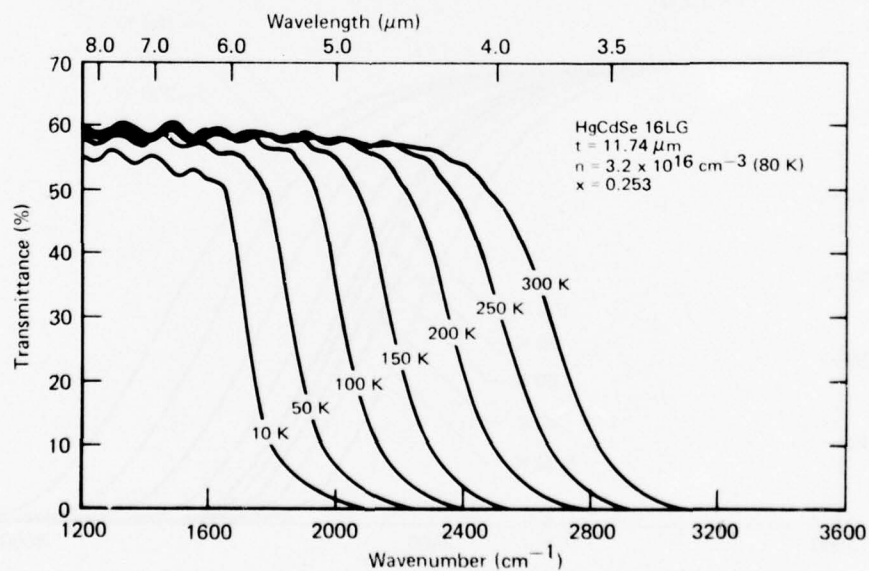


Figure 76 Infrared transmittance spectra at different temperatures for $\text{Hg}_{0.747}\text{Cd}_{0.253}\text{Se}$ (16LG) annealed in vacuum at 240°C for 48 h

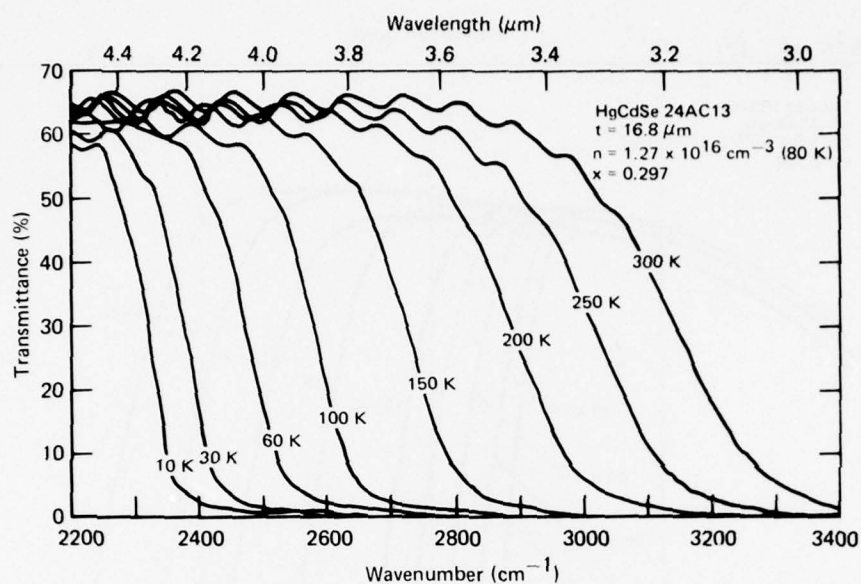


Figure 77 Infrared transmittance spectra at different temperatures for $\text{Hg}_{0.703}\text{Cd}_{0.297}\text{Se}$ (24AC13) as-grown

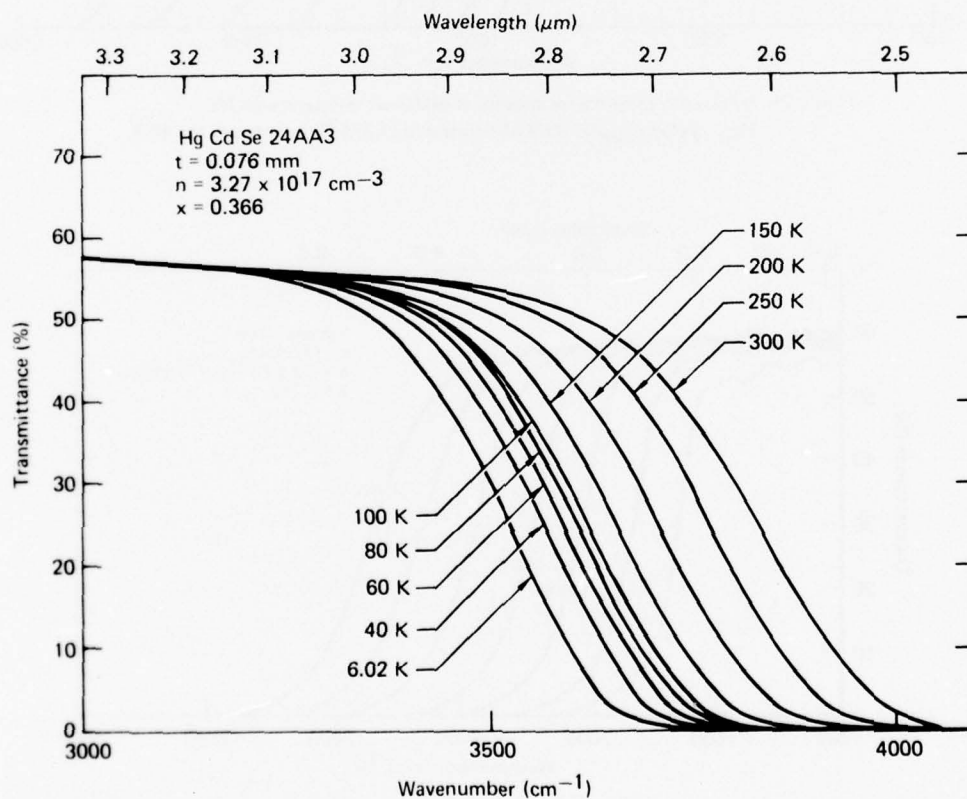


Figure 78 Infrared transmittance spectra at different temperatures of as-grown $\text{Hg}_{0.634}\text{Cd}_{0.366}\text{Se}$ (24AA3)

As shown in Figures 71 and 73, the infrared transmittance of the as-grown specimens, 16DAH and 16DCD, falls to zero at long wavelengths. This is a consequence of the relatively high electron concentrations in these samples (Figures 34 and 44), which causes a large free-carrier absorption. The broadness of the transition to zero transmission at short wavelengths was determined to be caused by compositional inhomogeneities in these samples.

On the basis of the homogeneity screening described in Section 5.5, selected areas of 16EC8, 16EB12, 16EB4, 16EA6, 16LG, 24AC13, and 24AA3 slices were used for infrared-transmission measurements because of their high degree of homogeneity. The transmittance spectra for these samples after they were annealed at 239°C in vacuum for 48 h are shown in Figures 70, 72, and 74-78. The transmission edges for these samples are much narrower than those for 16DAH and 16DCD, and the rounding of the transmission edges is caused by band-edge tailing and non-degeneracy of the electron distribution. The transmittance spectra of these samples have well-defined interference fringes, which for clarity of presentation are not shown in Figures 72, 74, 75, and 78.

7.4 Index of Refraction

The index of refraction, n^* , can be calculated from the spacing of the interference fringes of the transmittance spectra from the relation

$$n^* = \frac{m}{2d} \frac{1}{\nu_{n+m} - \nu_n}, \quad (41)$$

where ν_n and ν_{n+m} are the wavenumbers at n^{th} and $(n+m)^{\text{th}}$ interference peaks, m is the number of fringes between these peaks, and d is the sample thickness. This determination of n^* is precise, but as Moss³⁰ noted, it is insensitive to any linear dependence of n^* on wavelength. The index of refraction was determined by this method from the interference fringes in the transmittance spectra of HgCdSe 16EC8, 16EB12, 16EA6, 16LG, and 24AC13; the results are summarized in Table 13. In this table, the values given are interpolations between data points if spectra were not obtained for a sample at temperatures that coincide with those listed.

TABLE 13. INDEX OF REFRACTION OF $\text{Hg}_{1-x}\text{Cd}_x\text{Se}$ ALLOYS AT DIFFERENT TEMPERATURES; BASED ON TRANSMITTANCE-SPECTRA INTERFERENCE FRINGES

Temperature (K)	Index of refraction, n^*				
	16EC8 $x = 0.153$	16EB12 $x = 0.194$	16EA6 $x = 0.228$	16LG $x = 0.253$	24AC13 $x = 0.297$
10	4.90	3.79	3.70	3.45	3.21
25	4.68	3.75	3.71	3.42	3.21
50	4.42	3.69	3.64	3.35	3.20
75	4.42	3.62	3.55	3.34	3.20
100	4.29	3.57	3.37	3.34	3.20
125	4.23	3.50	3.36	3.30	3.18
150	4.18	3.45	3.37	3.27	3.16
175	4.10	3.40	3.54	3.24	3.14
200	4.03	3.40	3.43	3.23	3.13
250	3.95	3.43	3.38	3.13	3.11
300	3.86	3.39	3.41	3.11	3.09

The index of refraction can also be estimated from the transmittance of a specimen in the spectral region above the transmission edge. In this spectral region, the absorptance, α , is nearly zero. In general, the transmittance is related to the absorptance according to

$$\mathcal{T} = \frac{(1-R)^2 e^{-\alpha d}}{1-R^2 e^{-2\alpha d}}, \quad (42)$$

where \mathcal{T} is the transmittance of the sample, α is the absorption coefficient, d is the sample thickness, and R represents reflection losses. R is calculated from the expression

$$R = \left(\frac{n^* - 1}{n^* + 1} \right)^2. \quad (43)$$

When $\alpha \approx 0$, Equation (43) reduces to

$$\mathcal{T} = \frac{1 - R}{1 + R} \quad (\alpha = 0), \quad (44)$$

or

$$R = \frac{1 - \mathcal{F}}{1 + \mathcal{F}} \quad (\alpha = 0). \quad (45)$$

If Equations (43) and (45) are solved simultaneously for n^* , the result is

$$n^* = \frac{1 + (1 - \mathcal{F}^2)^{1/2}}{\mathcal{F}} \quad (\alpha = 0). \quad (46)$$

Except for 16EC8, for which n^* is markedly dependent on temperature, the n^* values calculated from Equation (46) are within 1-3% of the values determined from the interference fringes and given in Table 13. The n^* values calculated from Equation (46) compared with the values in Table 13 for 16EC8 ranged from 7% larger at 10 K to 11% smaller at 300 K.

Implicit in the derivations given here is the assumption that n^* is independent of wavelength. The determination of the dependence of n^* on wavelength requires reflectance spectra, which were not obtained for this study.

As can be seen from Table 13, the index of refraction generally decreases as the temperature increases for all compositions of $\text{Hg}_{1-x}\text{Cd}_x\text{Se}$ for which $0.15 < x < 0.30$, and the rate of decrease is larger for smaller x .

7.5 Absorptance Spectra Calculations

The infrared transmittance spectra shown in Figures 70-78 demonstrate the strong dependences of the absorption on composition and temperature for the $\text{Hg}_{1-x}\text{Cd}_x\text{Se}$ alloys. The absorptance, α , was calculated from the transmittance by using Equation (42) and the values for n^* given in Section 7.4. The absorptance was calculated at wavenumber increments of 2 cm^{-1} for each of the transmittance spectra to obtain absorptance spectra.

The absorptance spectra were analyzed to obtain the energy gap, E_G , and Fermi energy, E_F , as functions of x and temperature for the $\text{Hg}_{1-x}\text{Cd}_x\text{Se}$ alloys. The analyses were performed by fitting a theoretical expression for the absorptance to the experimental spectra. The theory is presented in Section 7.7. The energy gap, E_G , the interband momentum-matrix-element, P , the conduction-band to light-hole-band lifetime, $\tau_{c, \ell h}$, and the conduction-band to heavy-hole-band lifetime, $\tau_{c, h h}$, were treated as

parameters and adjusted to give the best fit of the theoretical absorptance to the experimental spectra. For high photon energies, P dominates the magnitude of the absorptance, and its value may thus be obtained by fitting the data for short wavelengths. For all samples and temperatures, a value for P of $8.0 \times 10^{-8} \text{ eV} \cdot \text{cm}^{-1}$ gives a good fit to the data. At lower energies, E_G , $\tau_{c, \ell h}$ and $\tau_{c, hh}$ were adjusted to give the best fits. For temperatures lower than 80 K, E_G is the dominant parameter, and small changes in the value of E_G cause large shifts of the theoretical absorption edge.

Representative examples of the data fitting are shown in Figures 79-81 for HgCdSe 16LG. The fit at 30 K (Figure 79) was obtained with $E_G = 0.200$ eV and $E_F = 0.0207$ eV. The value obtained for E_G is significantly below the energy at which the absorptance is appreciable. This is because the sample is degenerate at 30 K, and the Fermi energy lies in the conduction band. The sum of E_G and E_F is the minimum energy for which optical transitions are possible.

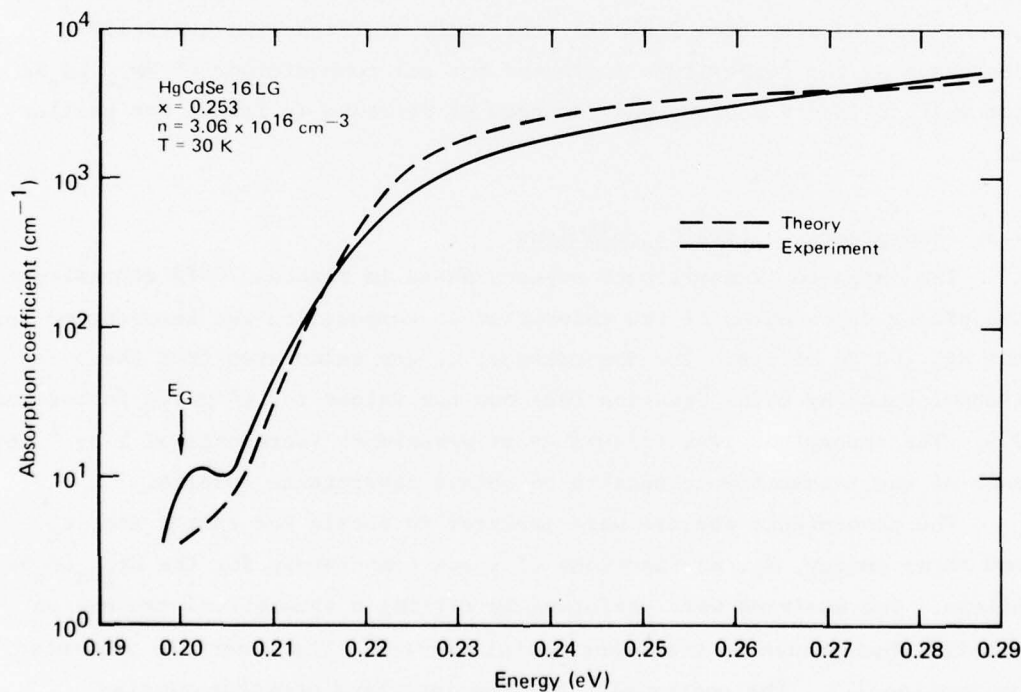


Figure 79 Theoretical and experimental absorption coefficient spectra at 30 K for $\text{Hg}_{0.747}\text{Cd}_{0.253}\text{Se}$ (16LG)

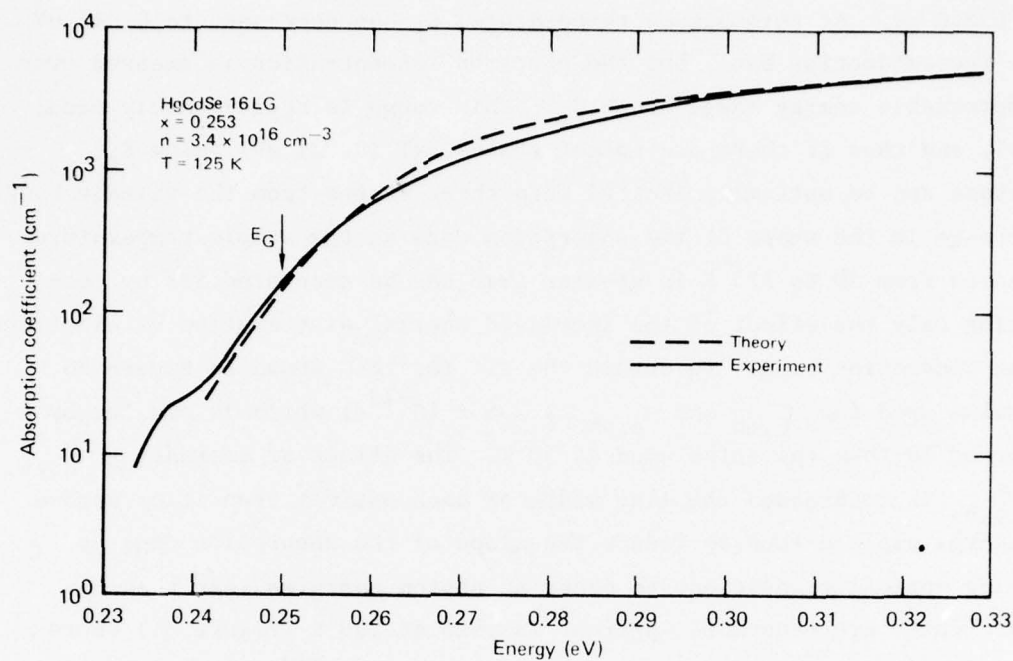


Figure 80 Theoretical and experimental absorption coefficient spectra at 125 K for Hg_{0.747}Cd_{0.253}Se (16LG)

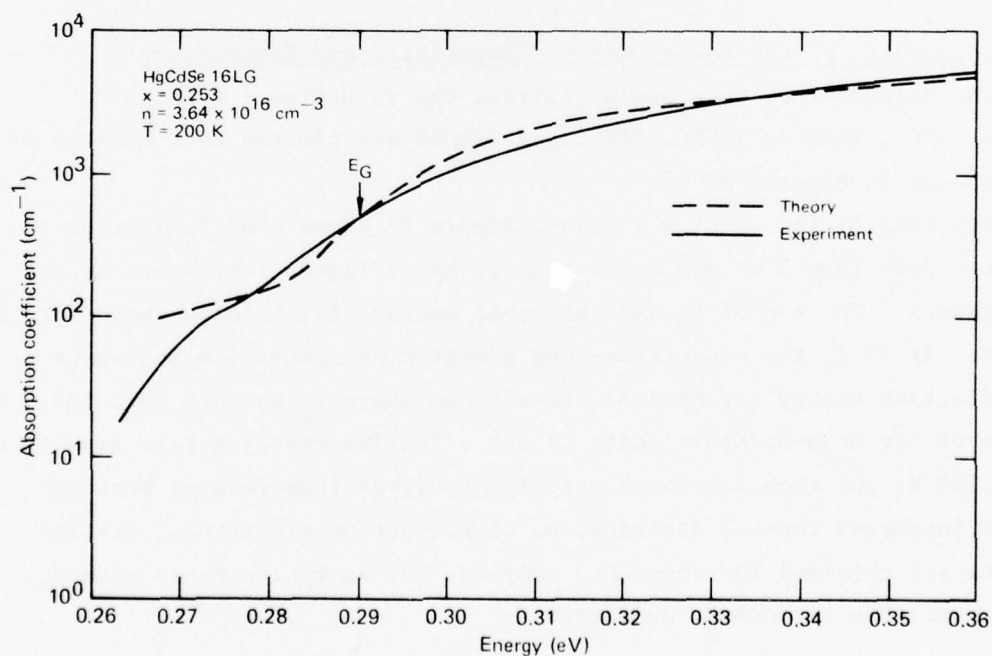


Figure 81 Theoretical and experimental absorption coefficient spectra at 200 K for Hg_{0.747}Cd_{0.253}Se (16LG)

At 125 K (Figure 80), a good fit to the data for 16LG is obtained with $E_G = 0.250$ eV. At this higher temperature, E_F has decreased to 0.011 eV above the conduction band, but the electron concentration is smeared over an appreciable energy range about E_F . This range is approximately equal to $4kT$, and thus if there are vacant states $2kT$ (0.021 eV) below E_F , electrons can be optically excited into these states from the valence band. The change in the shape of the absorption edge as the sample temperature increases from 30 to 125 K is greater than can be accounted for by considering only the effect of the increased thermal distribution of electrons in the conduction band. To obtain the fit for 16LG shown in Figure 80, the value used for $\tau_{c,\ell h}$ and $\tau_{c,hh}$ is 7.6×10^{-13} s, which is smaller by a factor of 10 than the value used at 30 K. The effect of decreasing $\tau_{c,\ell h}$ and $\tau_{c,hh}$ is to broaden the line width of each optical transition across the energy gap and thus to reduce the slope of the absorption edge by allowing optical transitions to occur at photon energies less than E_G . These effects are even more apparent in 16LG at 200 K (Figure 81) where values of $E_G = 0.290$ eV and $\tau_{c,hh} = \tau_{c,\ell h} = 2.1 \times 10^{-13}$ s are required to fit the data. The decrease in the values of $\tau_{c,hh}$ and $\tau_{c,\ell h}$ with increasing temperature is attributed to an increase in the electron-phonon interaction.

7.6 Dependence of the Energy Gap on Composition and Temperature

The values of E_G obtained by fitting the absorptance spectra of HgCdSe 16EC8, 16EB12, 16EA6, 16LG, and 24AC13 are plotted as functions of temperature in Figures 82-86.

For 16EB12, for which $x = 0.194$, Figure 83 shows that E_G increases by about 300% from 5 to 300 K and that it has a linear dependence on temperature. The sum of E_G and the Fermi energy, E_F , is also shown for this sample. At ≈ 5 K, the conduction-band electron-concentration increases the effective energy for optical transitions above E_G by more than 50%. The effect of the Moss-Burstein shift on the effective energy gap is significant up to 120 K, but then decreases rapidly at higher temperatures because of the increased thermal distribution of conduction electrons. Similar results are obtained for the other samples, but as E_G increases with x , its temperature dependence decreases.

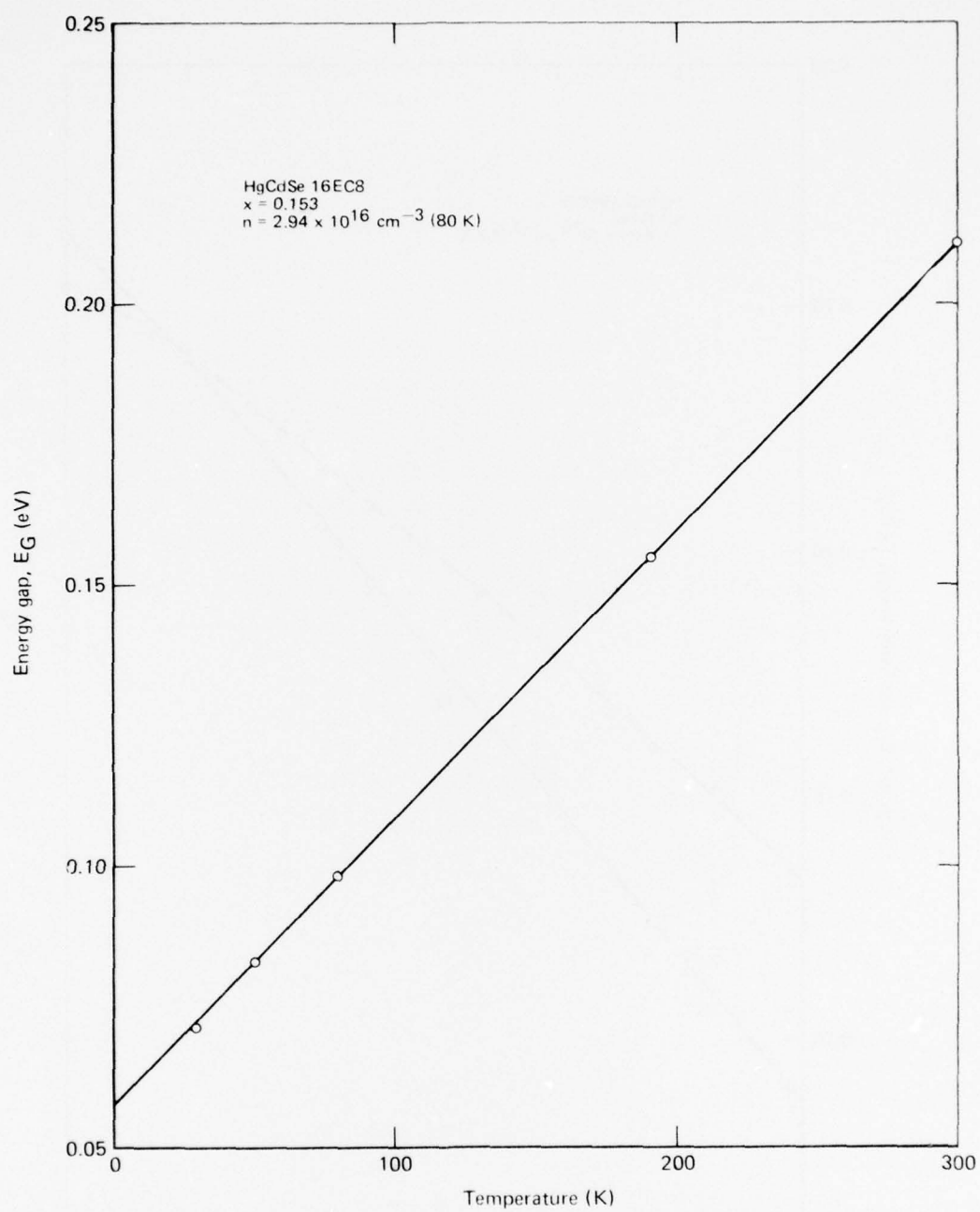


Figure 82 Temperature dependence of optical energy gap for $\text{Hg}_{0.847}\text{Cd}_{0.153}\text{Se}$ (16EC8)

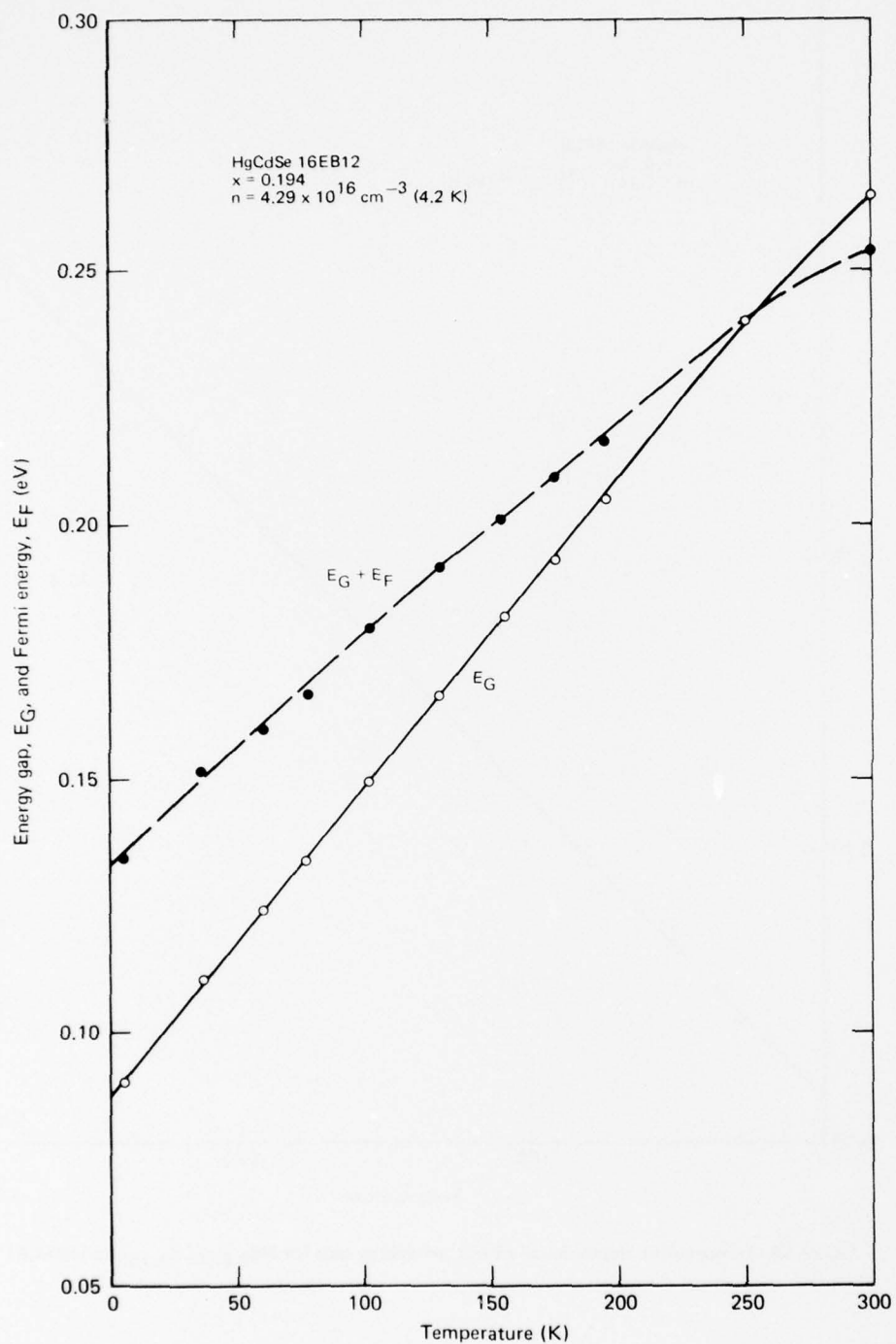


Figure 83 Temperature dependence of optical energy gap and Fermi energy for $\text{Hg}_{0.806}\text{Cd}_{0.194}\text{Se}$ (16EB12)

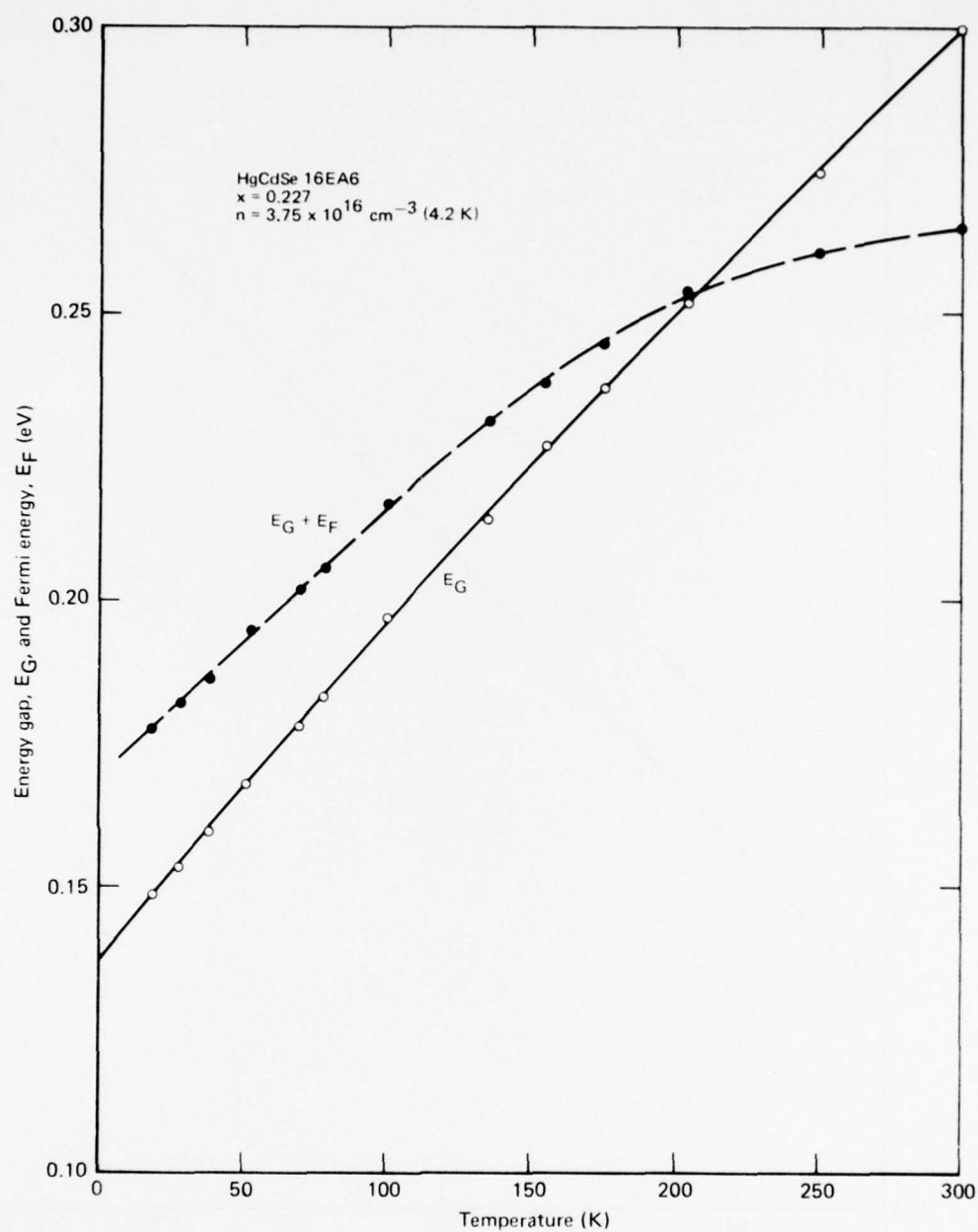


Figure 84 Temperature dependence of optical energy gap and Fermi energy for $\text{Hg}_{0.773}\text{Cd}_{0.227}\text{Se}$ (16EA6)

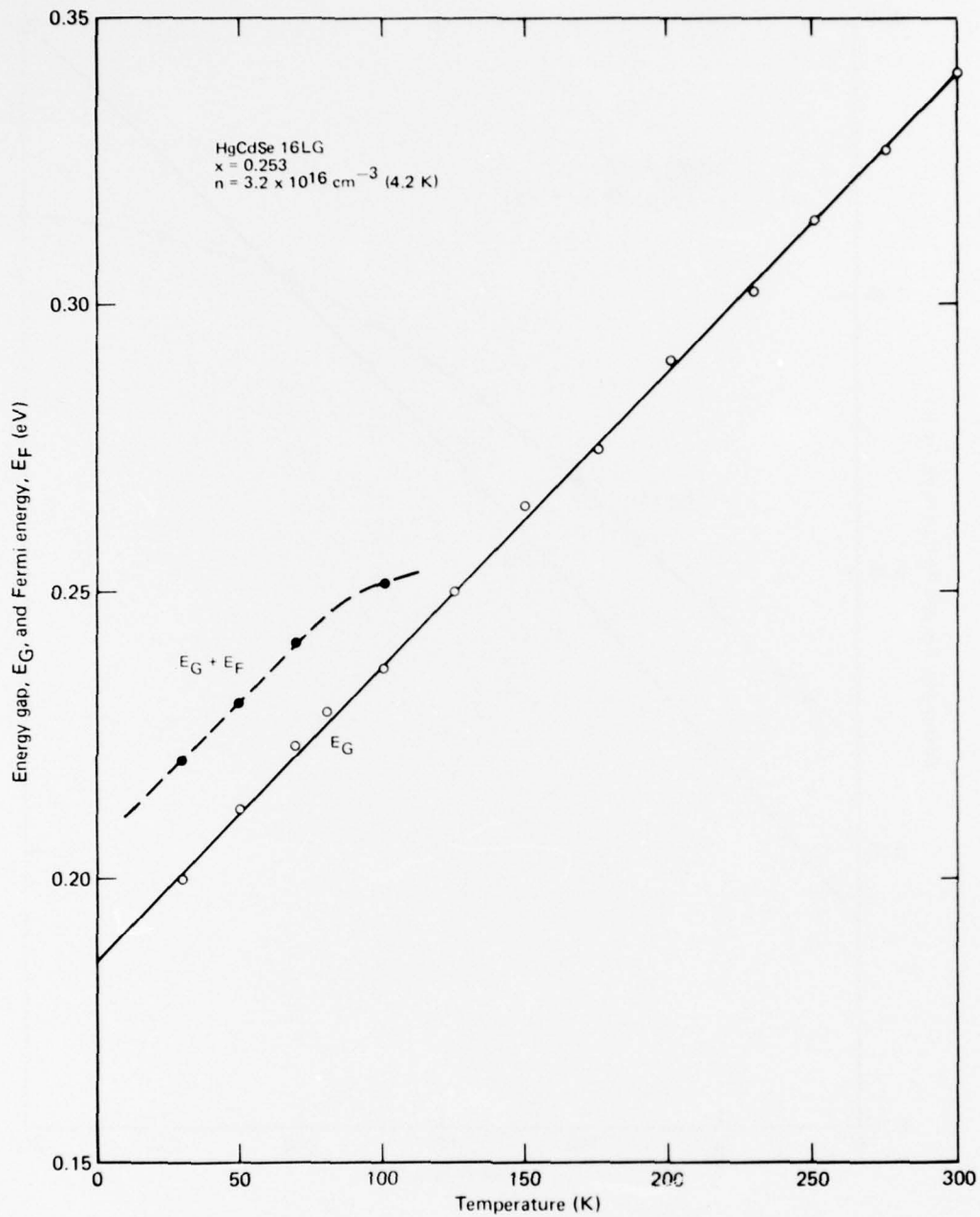


Figure 85 Temperature dependence of optical energy gap and Fermi energy for $\text{Hg}_{0.747}\text{Cd}_{0.253}\text{Se}$

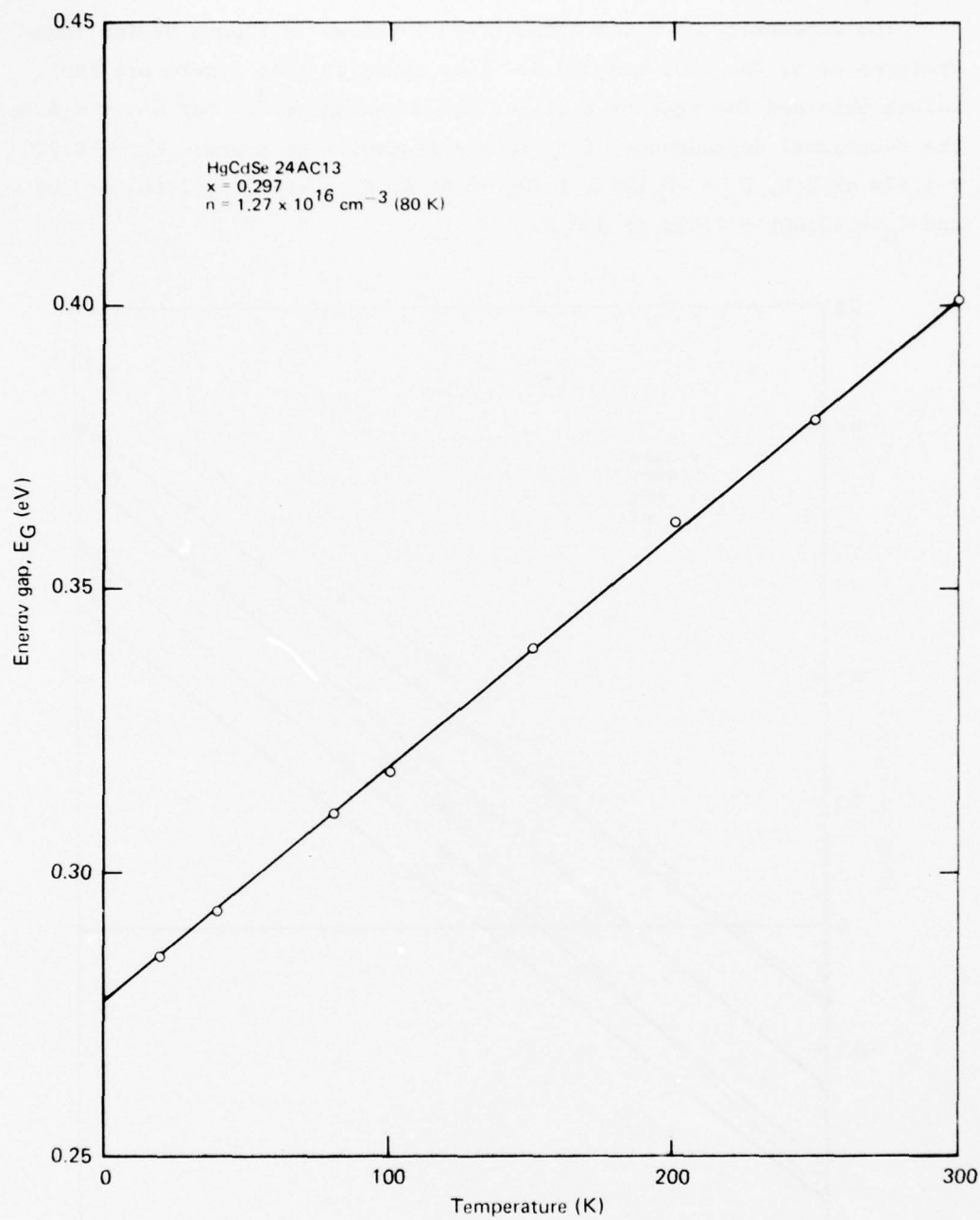


Figure 86 Temperature dependence of optical energy gap for $\text{Hg}_{0.703}\text{Cd}_{0.297}\text{Se}$ (24AC13)

The dependence of E_G on composition is shown in Figure 87 for temperatures of 5, 80, 200, and 300 K. Also shown in this figure are the values obtained for HgSe from electrical measurements⁹. For $0 < x < 0.3$, the functional dependences of E_G in electronvolts on x are: $E_G = -0.220 + 1.60x$ at 5 K, $E_G = -0.195 + 1.70x$ at 80 K, $E_G = -0.128 + 1.66x$ at 200 K, and $E_G = -0.061 + 1.57x$ at 300 K.

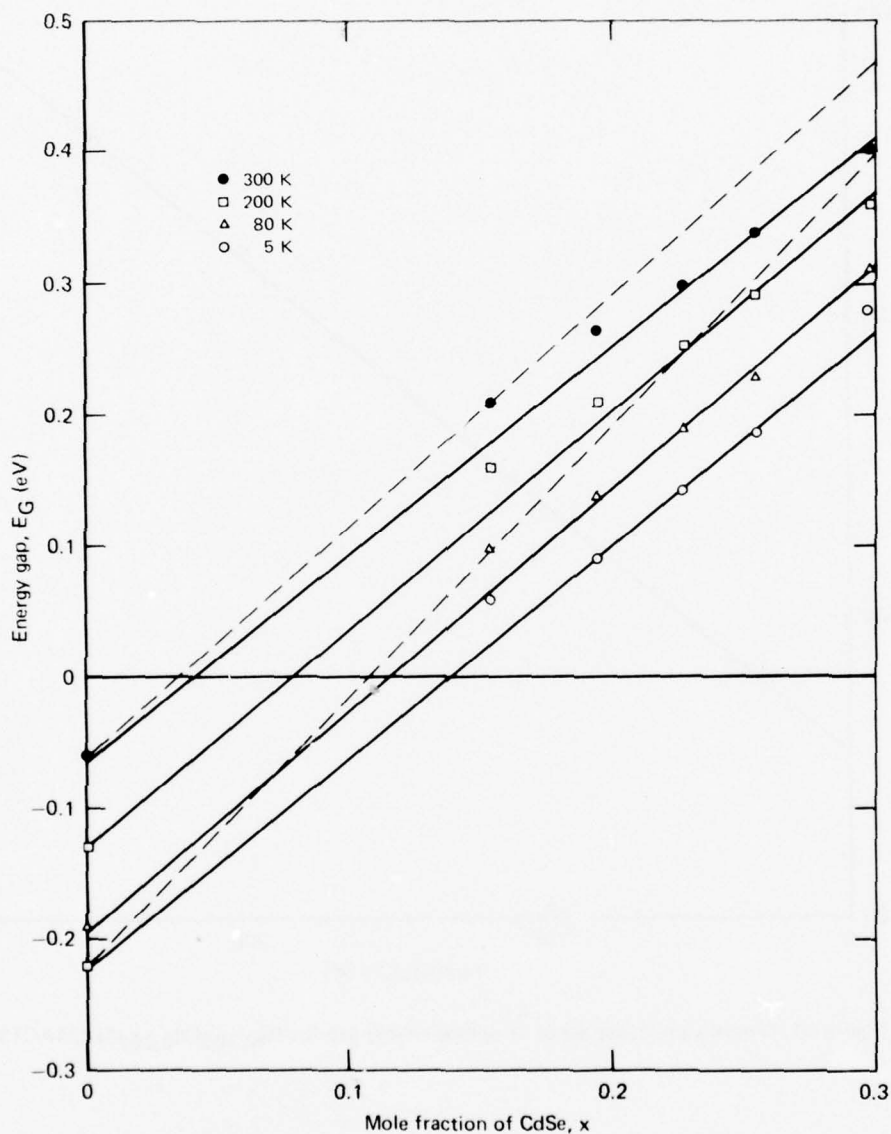


Figure 87 Energy gap as a function of x in $\text{Hg}_{1-x}\text{Cd}_x\text{Se}$ alloys; dotted lines are linear interpolations at 77 and 300 K shown in Figure 4. Data for HgSe ($x = 0$) are from Reference 9.

7.7 Calculation of Absorption Coefficient for Direct Interband Transitions

Because of the presence of extrinsic and thermally-excited electrons in the conduction band of the samples, accurate values of the fundamental band-gap-energy cannot be obtained directly from the experimental data. To obtain this quantity, a theoretical treatment of the absorption coefficient is required that accurately takes into account the temperature dependence of the electron population, the non-parabolicity of the band structure for the small-gap compositions, and the energy dependence of the optical transition probability. The fundamental quantity, from which all other optical properties can be calculated, is the complex dielectric function. This is calculated in the random-phase approximation and is expressed in terms of the fundamental material parameters (fundamental energy-gap, conduction-band/valence-band momentum-matrix-element, and spin-orbit splitting). By fitting the calculated absorption coefficient to the experimental data, numerical values can be obtained for these material parameters.

The theory presented here utilizes a formalism developed by Broerman³¹ for the dielectric function of HgSe. For frequencies larger than that corresponding to the fundamental energy-gap, the complex dielectric function, ϵ , can be expressed as the sum of a lattice part, an interband electronic part, and an intraband electronic part:

$$\epsilon(\omega) = \epsilon(\omega)^{\text{lat}} + \epsilon(\omega)^{\text{inter}} + \epsilon(\omega)^{\text{intra}}. \quad (47)$$

The interband electronic contribution is given by the relation

$$\epsilon(\omega)^{\text{inter}} = -\lim_{q \rightarrow 0} \frac{e^2}{\pi^2 q^2} \times \sum_{\substack{i,j \\ i \neq j}} \int d^3 k \frac{|\langle i, \vec{k} | e^{-i\vec{q} \cdot \vec{r}} | j, \vec{k} + \vec{q} \rangle|^2}{E_{\vec{k}+\vec{q},j}^{\rightarrow} - E_{\vec{k},i}^{\rightarrow} - \hbar\omega - i\hbar/\tau_{ij}} \left[f(E_{\vec{k}+\vec{q},j}^{\rightarrow}) - f(E_{\vec{k},i}^{\rightarrow}) \right], \quad (48)$$

where τ_{ij} are lifetimes associated with $i \rightarrow j$ excitations, $E_{\vec{k},i}^{\rightarrow}$ is the energy of the i^{th} band at crystal momentum \vec{k} , $f(E_{\vec{k},i}^{\rightarrow})$ is the Fermi distribu-

tion function, ω is the angular frequency, and \vec{q} is the momentum transfer. This contribution can be further divided into three parts: a light-hole/conduction-band excitation, a heavy-hole/conduction-band excitation, and a background from all other higher-energy excitations, ϵ_b :

$$\epsilon(\omega)^{\text{inter}} = \epsilon(\omega)^{\text{lh-c}} + \epsilon(\omega)^{\text{hh-c}} + \epsilon_b. \quad (49)$$

Because of the large energy differences between the states contributing to the background, ϵ_b is real and has no frequency dependence in the infrared. The calculation proceeds within the Kane three-band model²⁵, which considers the $\vec{k} \cdot \vec{p}$ interactions between the Γ_6 conduction band, the Γ_8 light-hole-band, and the Γ_7 split-off valence band. The heavy-hole band is considered to be parabolic with mass μ_{hh} , i.e.,

$$E_{\vec{k},hh}^{\text{par}} = - \frac{\hbar^2 k^2}{2\mu_{hh} m_0}, \quad (50)$$

where m_0 is the free electron mass. Within this model, the energies of the conduction, light-hole, and split-off bands are given by the solutions of the secular equation

$$E(E-E_G) (E + \Delta) - k^2 P^2 (E + 2\Delta/3) = 0, \quad (51)$$

where P is the momentum matrix-element, Δ is the valence-band spin-orbit splitting, E_G is the fundamental gap, and the free-electron energy ($\hbar^2 k^2 / 2m$) is taken to be negligible. The light-hole/conduction-band and heavy-hole/conduction-band matrix-elements are then calculated to second order in q to be:

$$|\langle \text{lh}, \vec{k} | e^{-i\vec{q} \cdot \vec{r}} | \text{c}, \vec{k} + \vec{q} \rangle|^2 = \frac{L_2^{\text{lh-c}}}{k} q^2 \cos^2 \theta - \frac{L_0^{\text{lh-c}}}{k^2} q^2 \sin^2 \theta \quad (52)$$

and

$$|\langle \text{c}, \vec{k} | e^{-i\vec{q} \cdot \vec{r}} | \text{hh}, \vec{k} + \vec{q} \rangle|^2 = \frac{(b_c + \sqrt{2}c_c)^2}{4} \frac{q^2 \sin^2 \theta}{k^2}. \quad (53)$$

In Equations (52) and (53), θ is the angle between \vec{k} and \vec{q} , and the functions appearing in the expressions are defined as follows:

$$\begin{aligned}
L_2^{\ell h-c} = & 2a_{\ell h}^2 \left(a_c A_{2c} + 2kA_{1c}^2 \right) + 2b_{\ell h}^2 \left(b_c B_{2c} + 2kB_{1c}^2 \right) \\
& + 2c_{\ell h}^2 \left(c_c C_{2c} + 2kC_{1c}^2 \right) + 2a_{\ell h} \left[a_c \left(b_{\ell h} B_{2c} + c_{\ell h} C_{2c} \right) + 4A_{2c} \left(b_{\ell h} b_c + c_{\ell h} c_c \right) \right. \\
& \left. + 4kA_{1c} \left(b_{\ell h} B_{1c} + c_{\ell h} C_{1c} \right) \right] + 2b_{\ell h} c_{\ell h} \left[b_c C_{2c} + c_c B_{2c} + 4kB_{1c} C_{1c} \right], \quad (54)
\end{aligned}$$

$$\begin{aligned}
L_O^{\ell h-c} = & \frac{1}{2} \left[2 \left(a_{\ell h} a_c \right) \left(b_{\ell h} b_c + c_{\ell h} c_c \right) + \frac{3}{2} \left(b_{\ell h} b_c \right)^2 + \sqrt{2} \left(b_{\ell h} b_c \right) \left(b_{\ell h} c_c + c_{\ell h} b_c \right) \right. \\
& \left. + 4 \left(b_{\ell h} c_c \right) \left(c_{\ell h} c_c \right) - \left(b_{\ell h} c_c + c_{\ell h} b_c \right)^2 + 2 \left(c_{\ell h} c_c \right)^2 \right], \quad (55)
\end{aligned}$$

$$a_c = \frac{\left[E_c \quad E_c + \Delta \quad E_c + 2\Delta/3 \right]^{1/2}}{N_c}, \quad (56)$$

$$b_c = \frac{\sqrt{2}\Delta \left(E_c - E_G \right)^{1/2}}{3N_c}, \quad (57)$$

$$c_c = \frac{\left(E_c - E_G \right)^{1/2} \left(E_c + 2\Delta/3 \right)}{N_c}, \quad (58)$$

$$N_c = \left[E_c \left(E_c + \Delta \right) \left(E_c + 2\Delta/3 \right) + \frac{2\Delta^2}{9} \left(E_c - E_G \right) + \left(E_c - E_G \right) \left(E_c + 2\Delta/3 \right)^2 \right]^{1/2}, \quad (59)$$

$$\left\{ A_{1c}, B_{1c}, C_{1c} \right\} = k \frac{d}{d(k^2)} \left\{ a_c, b_c, c_c \right\}, \quad (60)$$

$$\left\{ A_{2c}, B_{2c}, C_{2c} \right\} = 2k^3 \frac{d^2}{d(k^2)^2} \left\{ a_c, b_c, c_c \right\}, \quad (61)$$

$$a_{\ell h} = \frac{\left[-E_{\ell h} \left(E_{\ell h} + \Delta \right) \left(E_{\ell h} + 2\Delta/3 \right) \right]^{1/2}}{N_{\ell h}}, \quad (62)$$

$$b_{\ell h} = \frac{-\sqrt{2}\Delta \left(E_G - E_{\ell h} \right)^{1/2}}{3 N_{\ell h}}, \quad (63)$$

$$c_{\ell h} = \frac{-\left(E_G - E_{\ell h}\right)^{1/2} \left(E_{\ell h} + 2\Delta/3\right)}{N_{\ell h}}, \quad (64)$$

and

$$N_{\ell h} = \left[-E_{\ell h} \left(E_{\ell h} + \Delta\right) \left(E_{\ell h} + 2\Delta/3\right) + \frac{2\Delta^2}{9} \left(E_G - E_{\ell h}\right) + \left(E_G - E_{\ell h}\right) \left(E_{\ell h} + 2\Delta/3\right)^2 \right]^{1/2} \quad (65)$$

Taking the limit as $q \rightarrow 0$ and performing the angular integrations, one then obtains

$$\begin{aligned} \varepsilon(\omega)^{\ell h-c} &= \frac{4e^2}{3\pi} \int_0^{k_{BC}} dk \left[f(E_{k,\ell h}) - f(E_{k,c}) \right] \left[k L_2^{\ell h-c} - 2L_o^{\ell h-c} \right] \\ &\times \left\{ \frac{1}{E_{k,c} - E_{k,\ell h} - \hbar\omega - i\hbar/\tau_{c,\ell h}} + \frac{1}{E_{k,c} - E_{k,\ell h} + \hbar\omega + i\hbar/\tau_{c,\ell h}} \right\} \end{aligned} \quad (66)$$

and

$$\begin{aligned} \varepsilon(\omega)^{hh-c} &= \frac{2e^2}{3\pi P} \\ &\times \int_{E_G}^{E_{BC}} dE G(E) [f(E_{hh}) - f(E)] \left\{ \frac{1}{E - E_{hh} - \hbar\omega - i\hbar/\tau_{c,\ell h}} + \frac{1}{E - E_{hh} + \hbar\omega + i\hbar/\tau_{hh}} \right\} \end{aligned} \quad (67)$$

where

$$G(E) = \frac{\left[2E^3 + (3\Delta - E_G)E^2 + 4/3\Delta(\Delta - E_G)E - 2\Delta^2 E_G/3 \right] \left(E - E_G \right)^{1/2} (E + \Delta)^{3/2}}{E^{1/2} (E + 2\Delta/3)^{3/2} \left[N_c(E) \right]^2}, \quad (68)$$

$$E_{hh} = \frac{\hbar^2}{2\mu_{hh} m_o} \frac{E(E - E_G)(E + \Delta)}{P^2 (E + 2\Delta/3)} \quad (69)$$

and k_{BC} and E_{BC} are the crystal momentum and conduction-band energy at the edge of the Brillouin zones. The expressions A_{ic} , B_{ic} and C_{ic} [Equations (60) and (61)] can be obtained by using the secular equation to express k^2 in terms of $E_{k,c}$ and then differentiating.

The intraband part,

$$\varepsilon(\omega)^{\text{intra}} = - \lim_{q \rightarrow 0} \frac{e^2}{\pi q^2} \times \sum_{i=c, \ell h, hh} \int d^3 k \frac{|\langle i, \vec{k} | e^{-i\vec{q} \cdot \vec{r}} | i, \vec{k} + \vec{q} \rangle|^2}{E_{\vec{k}+\vec{q}, i} - E_{\vec{k}, i} - \hbar\omega - i\hbar/\tau_i} \left[f(E_{\vec{k}+\vec{q}, i}) - f(E_{\vec{k}, i}) \right], \quad (70)$$

is similarly calculated. One obtains the following results:

$$\varepsilon^c(\omega) = - \frac{1}{(\omega + i/\tau_c)^2} \frac{8e^2}{3\pi P k_B T} \times \int_{E_G}^{E_{BC}} dE \frac{\left[E(E - E_G)(E + \Delta) \right]^{3/2} (E + 2\Delta/3)^{1/2}}{\left[2E^3 + (3\Delta - E_G)E^2 + \frac{4}{3}\Delta(\Delta - E_G)E - \frac{2}{3}\Delta^2 E_G \right]} \frac{e^{(E - E_F)/k_B T}}{\left[e^{(E - E_F)/k_B T} + 1 \right]^2}, \quad (71)$$

$$\varepsilon^{\ell h}(\omega) = - \frac{1}{(\omega + i/\tau_{\ell h})^2} \frac{8e^2}{3 P k_B T} \times \int_0^{-E_{B\ell h}} dE \frac{\left[E(E + E_G)(E - \Delta) \right]^{3/2} (E - 2\Delta/3)^{1/2}}{\left[2E^3 - (3\Delta - E_G)E^2 + \frac{4}{3}\Delta(\Delta - E_G)E + \frac{2}{3}\Delta^2 E_G \right]} \frac{e^{(E + E_F)/k_B T}}{\left[e^{(E + E_F)/k_B T} + 1 \right]^2}, \quad (72)$$

and

$$\varepsilon^{hh}(\omega) = \frac{4\pi N_{hh} e^2}{\mu_{hh} m_o (\omega + i/\tau_{hh})^2}, \quad (73)$$

where E_F is the Fermi energy, N_{hh} is the density of heavy holes, T is the temperature, k_B is the Boltzmann constant, and $E_{B\ell h}$ is the energy of the light-hole band at the edge of the Brillouin zone.

To evaluate these expressions for the electronic part of the dielectric function, one must have values for the Fermi energy, E_F . These are found by solving numerically the charge neutrality condition,

$$N_e - N_{lh} - N_{hh} = N_D, \quad (74)$$

where N_e , N_{lh} , N_{hh} , and N_D are respectively the densities of electrons, light holes, heavy holes, and donors. The following expressions for the charge-carrier densities are obtained from the secular equations:

$$N_e = \frac{1}{2\pi^2 P^3} \times \int_{E_G}^{E_{BC}} dE f(E, Z) \frac{\left[2E^3 + (3\Delta - E_G)E^2 + 4\Delta/3 (\Delta - E_G)E - 2\Delta^2 E_G/3 \right] \left[E(E - E_G)(E + \Delta) \right]^{1/2}}{(E + 2\Delta/3)^{5/2}}, \quad (75)$$

$$N_{lh} = \frac{1}{2\pi^2 P^3} \times \int_0^{E_{Bhh}} dE f(E, -Z) \frac{\left[2E^3 - (3\Delta - E_G)E^2 + 4\Delta/3 (\Delta - E_G)E + 2\Delta^2 E_G/3 \right] \left[E(E + E_G)(E - \Delta) \right]^{1/2}}{(E - 2\Delta/3)^{5/2}}, \quad (76)$$

and

$$N_{hh} = \frac{1}{2\pi^2} \left(\frac{2\mu_{hh} m_o k_B T}{\hbar^2} \right)^{3/2} F_{1/2}(-Z), \quad (77)$$

where

$$f(E, Z) = \frac{1}{e^{(E/k_B T - Z)} + 1}, \quad (78)$$

$$Z = E_F/k_B T, \quad (79)$$

and $F_{1/2}(Z)$ is the Fermi function of order 1/2.

The lattice modes in the pseudobinary HgTe-CdTe and HgSe-CdSe alloys

conventionally split into two modes slightly shifted from those of the end point compounds. The lattice contribution to the dielectric function is treated classically:

$$\epsilon^{\text{lat}} = \sum_i \epsilon_i^{\text{lat}}, \quad (80)$$

where

$$\epsilon_i^{\text{lat}} = \frac{f_i}{1 - \left(\omega/\omega_{\tau i}\right)^2 - i\omega/\left(\omega_{\tau i}^2 \tau_i\right)}, \quad (81)$$

f_i is the oscillator strength of the i^{th} mode, $\omega_{\tau i}$ is the transverse optical frequency of the i^{th} mode, and τ_i is the damping time.

In order to calculate the observable optical properties, the total dielectric function is divided into its real and imaginary parts,

$$\epsilon = \epsilon_1 + i \epsilon_2, \quad (82)$$

and from these quantities the real and imaginary parts of the index of refraction, n^* and k^* , respectively, are calculated:

$$n^* = \frac{\left[\epsilon_1 + \epsilon_1^2 + \epsilon_2^2 \right]^{1/2}}{\sqrt{2}} \quad (83)$$

and

$$k^* = \frac{\epsilon_2}{2n^*}. \quad (84)$$

The absorptance, α , and the single-surface reflectance, R , are then given by

$$\alpha = 4\pi k^*/\lambda \quad (85)$$

and

$$R = \frac{(n^* - 1)^2 + (k^*)^2}{(n^* + 1)^2 + (k^*)^2}. \quad (86)$$

For the work described in this report, Δ was given the value 0.45 eV and μ_{hh} was given the value 0.50. The value for Δ is that found by Seiler, Galazka, and Becker²⁸ to fit oscillatory magnetoresistance data for HgSe.

No data exist for determining the value of μ_{hh} in the $\text{Hg}_{1-x}\text{Cd}_x\text{Se}$ alloys, and the value used here is an approximation based on the band parameters of other semiconductors; none of the calculations for n-type $\text{Hg}_{1-x}\text{Cd}_x\text{Se}$ depend upon precise values for μ_{hh} . In nearly all cases, the data could be fit by using a value for P of $8.0 \times 10^{-8} \text{ eV}\cdot\text{cm}$, which is within 10% of values found for other semiconductors that have the zincblende crystal structure. For low values of E_G , the theoretical expression for α is sensitive to changes in the value for P ; for this reason the E_G values determined from the absorptance spectra to be less than about 0.10 eV can be in error by as much as 20% but probably by less than 10%. For $\text{Hg}_{1-x}\text{Cd}_x\text{Se}$ alloys that have $E_G \lesssim 0.1 \text{ eV}$, a more comprehensive theoretical treatment is needed that includes the effects of higher conduction bands and of alloy disorder.

8. INFRARED PHOTOCONDUCTIVITY

8.1 Sample Preparation for Photoconductivity Measurements

Photoconductivity samples were ground, polished, and etched as described in Section 7.2, except that after the first surface had been prepared, the sample was immediately epoxy-bonded to a sapphire substrate with Eccobond 24 adhesive. This epoxy is used because it has a low viscosity and can be cured at room temperature to give a thin glue-line ($\approx 3 \mu\text{m}$). It is also flexible enough to be used at low temperatures and for joining materials with different coefficients of thermal expansion.

After the second surface was mechanically polished, the samples were shaped into six-contact, photo-Hall-bar elements by masking them and removing the excess material with an Airbrasive unit. The samples were then etched as described previously, and contacts were made to the sample. Initially, contacts were made with silver paint, but for the more recent studies, indium evaporated onto a freshly-etched surface at room temperature was used. The evaporated indium-films, approximately 200 nm thick, are delineated by a nickel mask placed over the sample during evaporation. Leads were then attached to the indium pads with a conductive epoxy, which can be used down to liquid-helium temperatures. The current-voltage characteristics of the samples were measured for both directions of current to confirm that ohmic contacts had been made. A typical sample before the indium evaporation stage is shown in Figure 88.

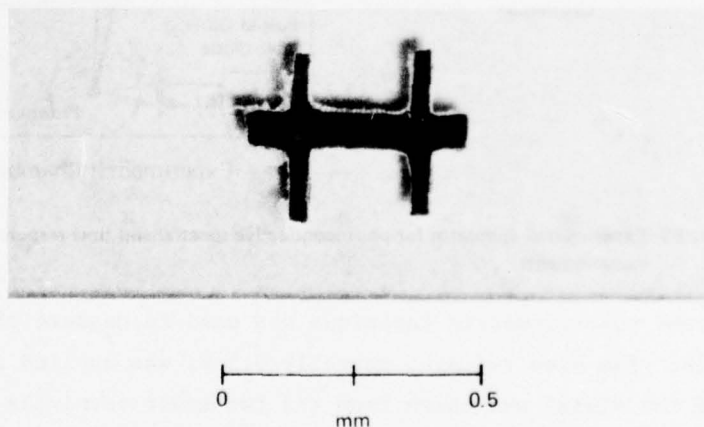


Figure 88 Six-contact photo-Hall bar element before evaporation of indium contacts

8.2 Photoconductivity Spectral-Response Measurements

The photoconductive spectral responses were measured with the apparatus shown in Figure 89. The source, grating, and filter combinations were chosen for the wavelength region of interest and can cover the spectral range from 1.0 to 25 μm . The reference detector is a calibrated triglycine-sulfate (TGS) detector, and its response is independent of wavelength. The entire spectrometer is flushed with dry nitrogen to avoid atmospheric absorption by CO_2 and water vapor. The elements were mounted on a cold finger of the liquid-helium dewar, and their temperatures were measured with a calibrated, silicon-diode sensor. The dewar is fitted with either a cesium iodide or KRS-5 window; the transmission of both of these materials is independent of wavelength between 1-25 μm .

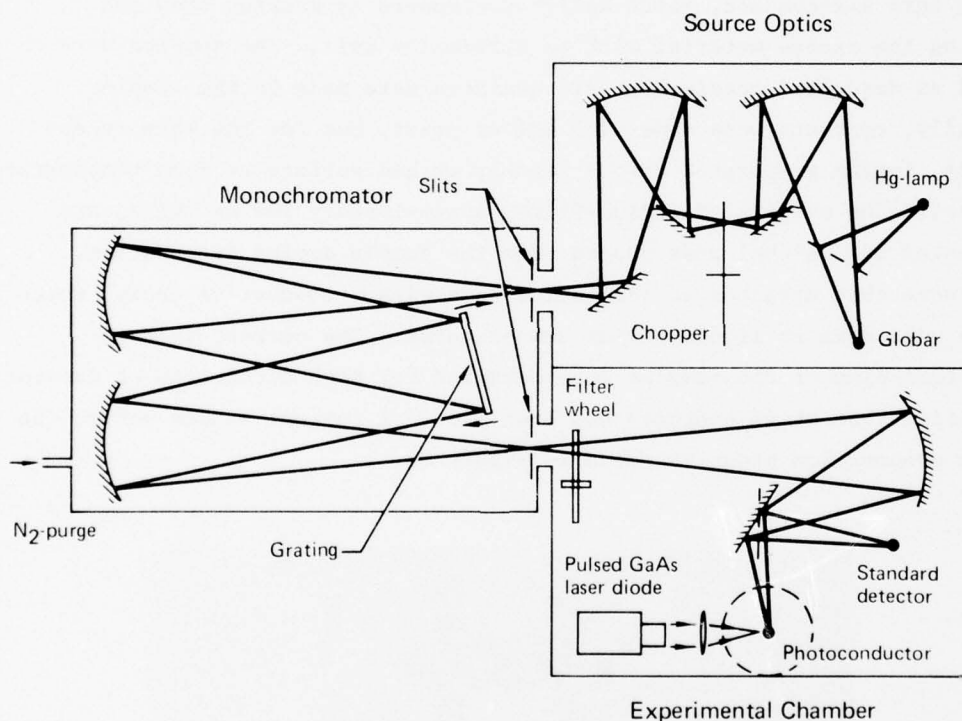


Figure 89 Experimental apparatus for photoconductive spectral and time response measurements

A four-probe potentiometric technique was used to measure the photoconductive signals. The bias voltage, normally 0.5 V, was applied across the end leads, and the signal was taken from the two inner terminals on each photo-Hall-bar specimen. The signal was amplified by a conventional, phase-sensitive amplifier for which the reference signal was generated by

the 104 Hz light-chopper. The output of the amplifier was displayed on an x-y recorder, whose x-axis was driven in synchronism with the wavelength drive of the spectrometer.

In calculating responsivity values for these elements, full account was taken of the area differences between the photoconductive element and the TGS detector and of the transmission loss of the dewar window.

Photoconductivity spectra were obtained for $\text{Hg}_{1-x}\text{Cd}_x\text{Se}$ specimens 24AA1PC1, 24AB16PC1, and 24AB14PC2, which had x-values of 0.35, 0.33, and 0.25, respectively. The normalized photoconductive-response curves at 4.2, 77 and 300 K are shown in Figures 90-92, and the measured responsivity and other experimental parameters are listed in Table 14. The electron concen-

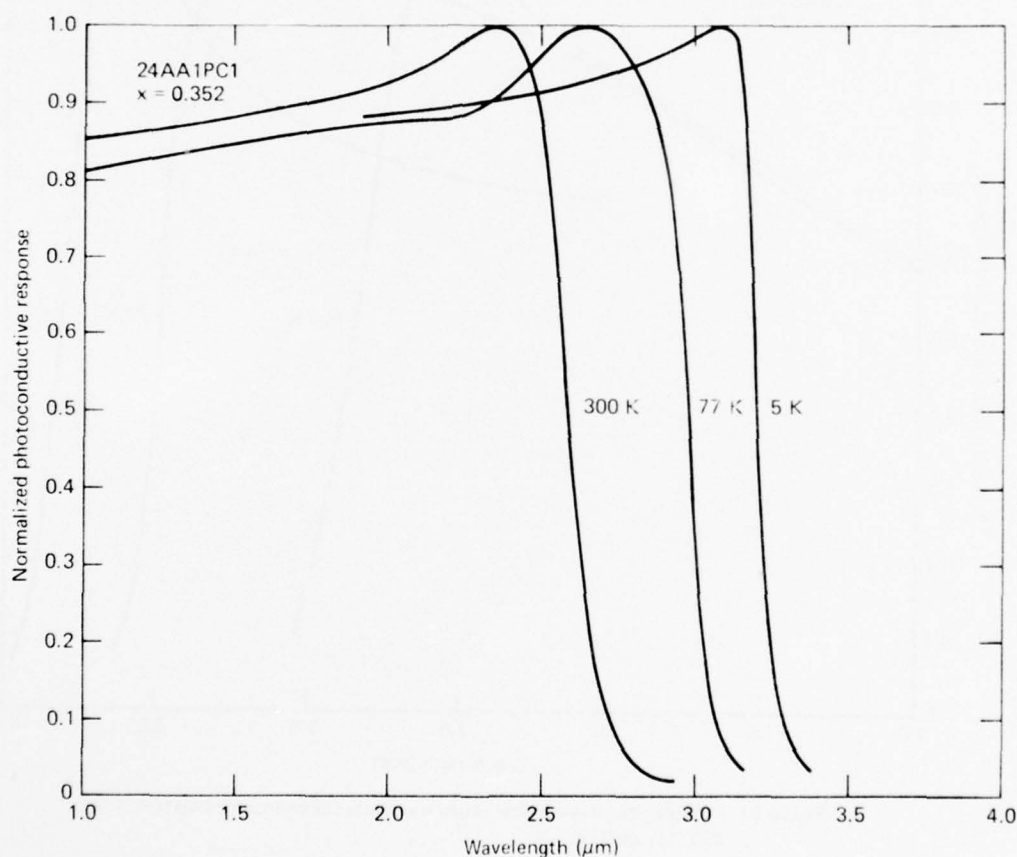


Figure 90. Photoconductive spectral response curves for element 24AA1PC1 at 300, 77, and 5 K

tration and mobility as functions of temperature are plotted in Figures 62, 54, and 50 for samples 24AA1PC1, 24AB16PC1, and 24AB14PC2, respectively. The photoconductivity spectra for each sample were recorded immediately after the sample was polished and etched. The spectra exhibit the expected gradual increase of photoconductive response as the wavelength increases until the wavelength corresponding to the absorption edge is reached. The photoconductive response falls abruptly at the absorption-edge wavelength and is zero at long wavelengths. The magnitude of the peak photoconductive-response increases as the sample temperature decreases from 300 to 4.2 K.

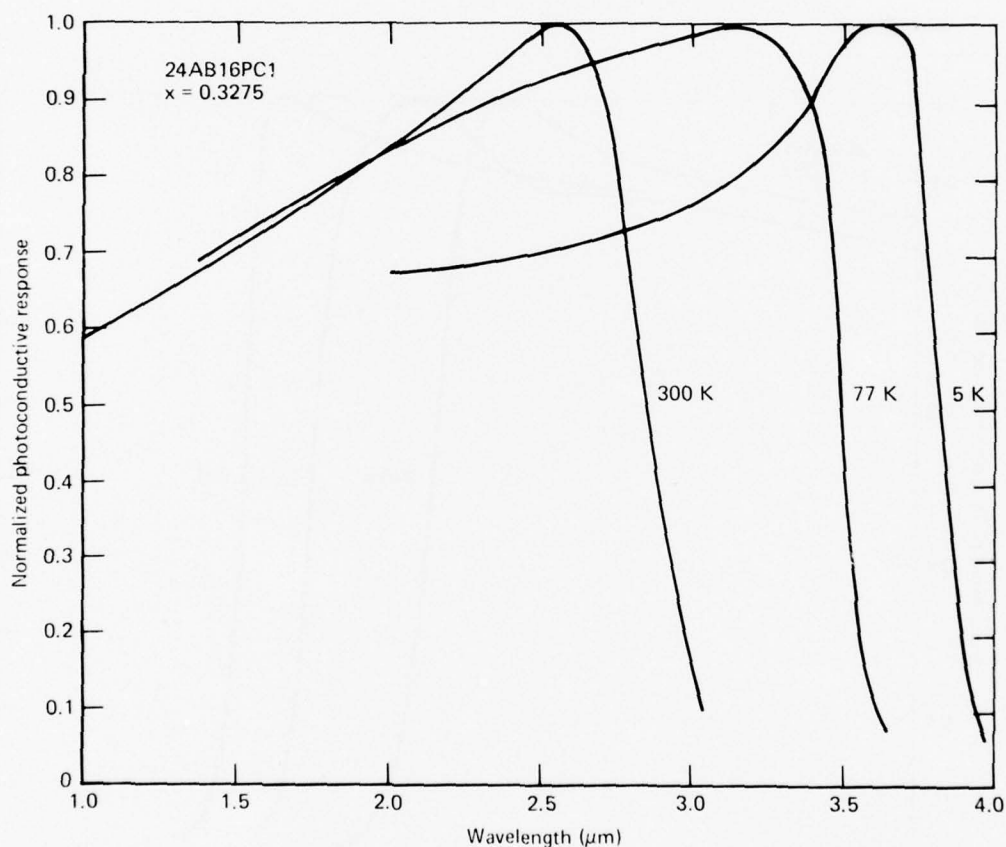


Figure 91 Photoconductive spectral response curves for element 24AB16PC1 at 300, 77, and 5 K

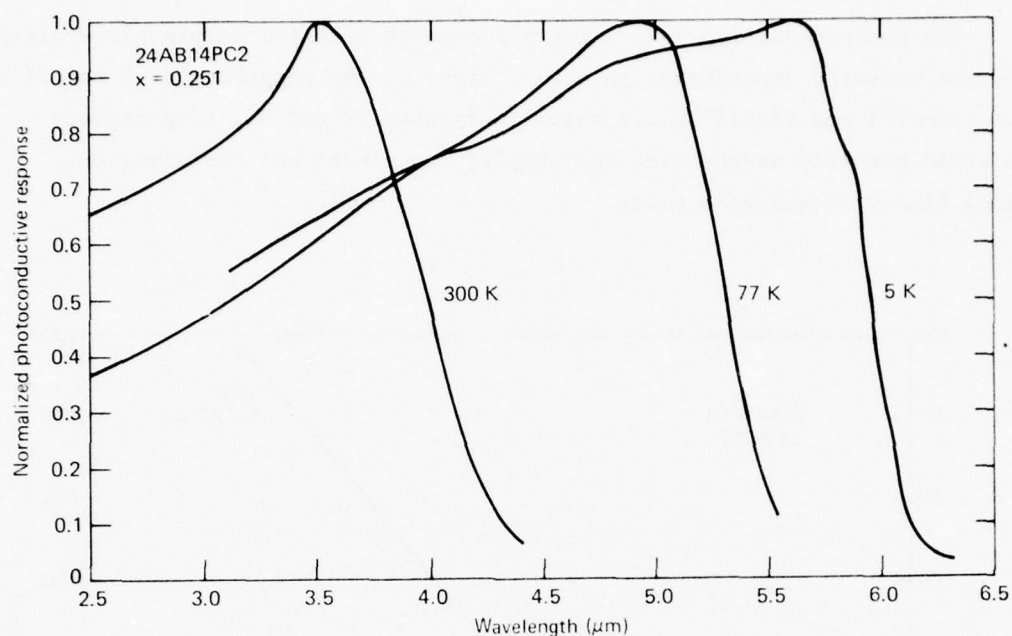


Figure 92 Photoconductive spectral response curves for element 24AB14PC2 at 300, 77, and 5 K

TABLE 14 PHOTOCONDUCTIVE RESPONSE OF $\text{Hg}_{1-x}\text{Cd}_x\text{Se}$ PHOTO-HALL-BAR ELEMENTS WITH 0.5 V BIAS

Sample no. and temperature	Sample thickness (mm)	Mole fraction of CdSe, x	Resistance (Ω)	Wavelength of peak response (μm)	Photo-conductive responsivity (V/W)	Excess carrier lifetime (μs)
24AA1PC1	0.005	0.352	1000	2.35	5.6	0.22
			260	2.65	16.9	0.40
			230	3.08	144	3.0
24AB16PC1	0.0075	0.328	875	2.58	17.6	0.58
			217	3.15	23.3	0.54
			159	3.63	270	5.0
24AB14PC2	0.020	0.251	44.0	3.51	0.25	0.12
			6.0	4.95	0.28	0.073
			3.4	5.65	0.48*	0.14

*Extrapolated value from measurement with 0.125 V bias

The photoconductive responsivity increases with the sample bias-voltage, and the measured dependences on bias voltage of the responses at 5 and 77 K for 24AA1PC1 and 24AB14PC2 are shown in Figures 93 and 94, respectively. To avoid possibly overheating the samples and electrical contacts, only small bias-voltages were used.

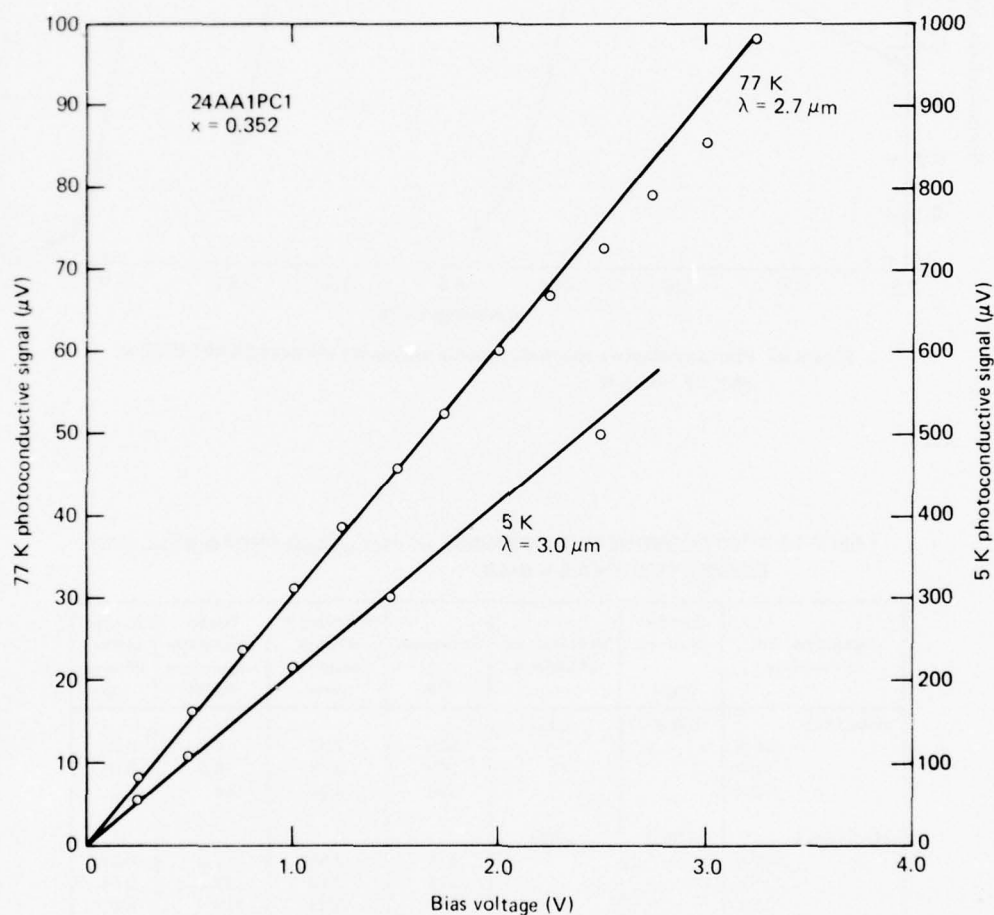


Figure 93 Dependence of photoconductive signal on bias voltage for element 24AA1PC1

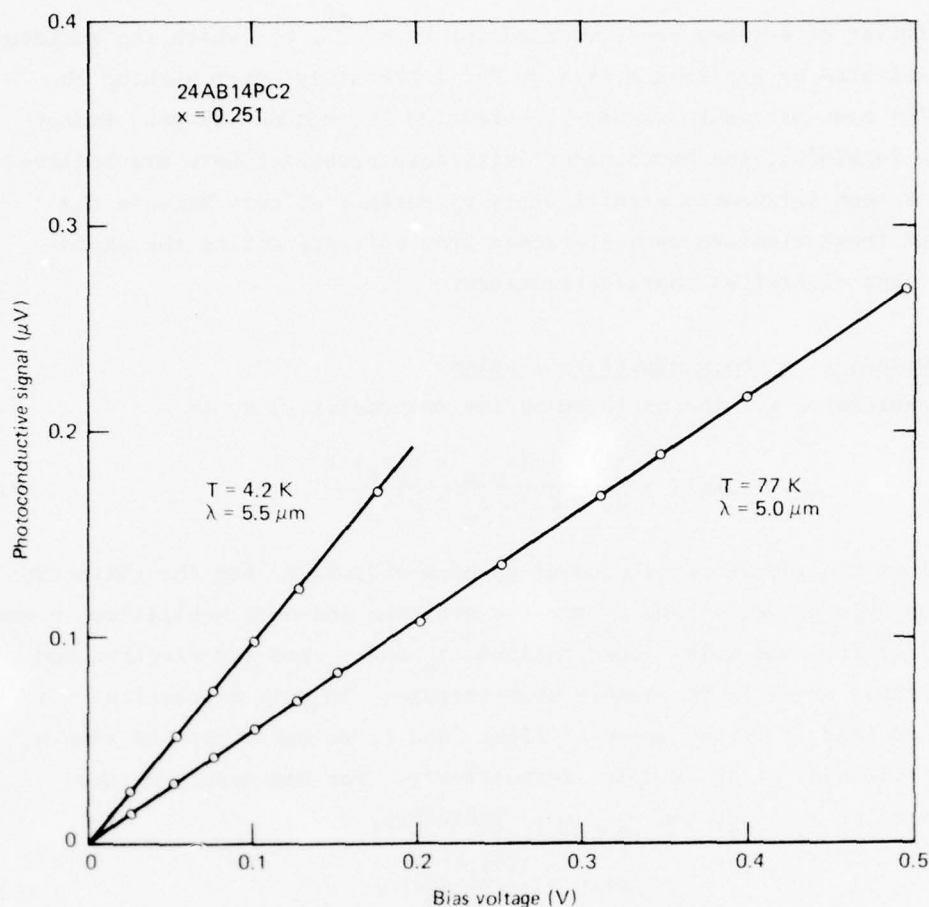


Figure 94 Dependence of photoconductive signal on bias voltage for element 24AB14PC2

During preliminary photoconductive measurements on some $\text{Hg}_{1-x}\text{Cd}_x\text{Se}$ samples, their properties were observed to be sensitive to surface effects, particularly if they had been exposed to moisture. For example, an accidental exposure to moisture of sample 24AA1PC1 decreased both its resistance and photoconductive-response by an order of magnitude. When this sample was re-etched, its original characteristics were restored. Because only a few micrometers of material were removed by re-etching the element, the observed decreases in resistance and responsivity resulting from the exposure to moisture were attributed to surface effects. Moisture probably causes an increase in the surface-carrier concentration and thereby causes the observed drop in sample resistance and acts as a shunt to the photoconductivity sig-

nal. A similar effect has been reported for HgCdTe³², for which the surface can be passivated by applying a film of ZnS immediately after etching the sample. The same procedure should be effective for HgCdSe alloys. Except for sample 24AB16PC1, the photoconductivity data presented here are believed to have not been influenced significantly by surface effects because the surfaces of these elements were protected from moisture during the photoconductive and electrical characterizations.

8.3 Photoconductive Charge-Carrier Lifetime

The expression for the photoconductive responsivity, \mathcal{R} , is

$$\mathcal{R}(\lambda) = \frac{\eta(\lambda) \lambda (\mu_n \tau_n + \mu_p \tau_p) V}{hc \ell wt (n \mu_n + p \mu_p)}, \quad (87)$$

where $\eta(\lambda)$ is the wavelength-dependent quantum-efficiency for the excitation of electron-hole pairs, μ_n and μ_p are the electron and hole mobilities, n and p are the electron and hole concentrations, τ_n and τ_p are the electron and hole lifetimes, and V is the sample bias-voltage. In this expression, h is Planck's constant, c is the speed of light, and ℓ , w , and t are the length, width, and thickness of the sample, respectively. For degenerate n-type material $n \gg p$, $\mu_n > \mu_p$, and $\tau_n \approx \tau_p$. Therefore,

$$\mathcal{R}(\lambda) \approx \frac{\eta(\lambda) \lambda \tau_n V}{hc \ell wt n}. \quad (88)$$

The quantum efficiency, $\eta(\lambda)$, cannot be determined experimentally, and we assume it to be unity. Equation (88) can be used to calculate the conduction-electron lifetime, τ_n , when $\mathcal{R}(\lambda)$, λ , V , and n are known, and the calculated values for the photoconductivity specimens 24AA1PC1, 24AB16PC1, and 24AB14PC2 are listed in Table 14.

8.4 Photoconductivity Time-Response Measurements

The photoconductivity samples were illuminated by a light pulse from a GaAs diode laser, and their responses were displayed on an oscilloscope screen. The laser source was mounted in the spectrometer system shown in Figure 89, and a mounted sample in the dewar could be aligned with the laser optical system by rotating the dewar. The usual practice was to make spectral-response measurements during the cooling cycle and time-response measurements as the sample was warmed from 4.2 K to 300 K. The laser emits light

of wavelength $0.91\ \mu\text{m}$. The laser light-pulse shapes for 100 and 20 ns pulses were measured by a Si photodiode and are shown in Figures 95a and 95b, respectively.

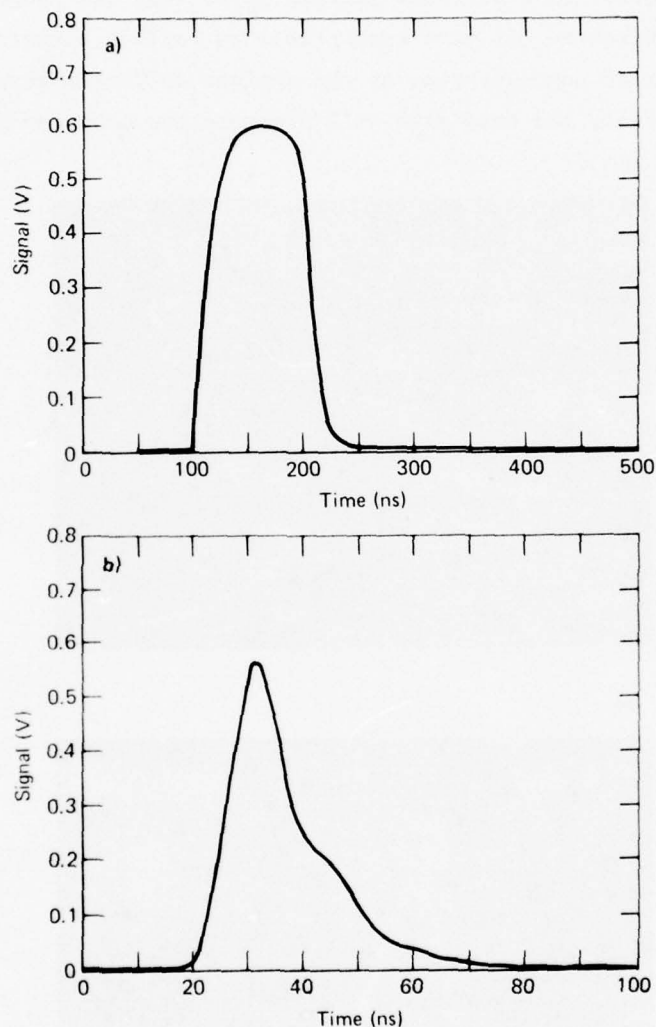
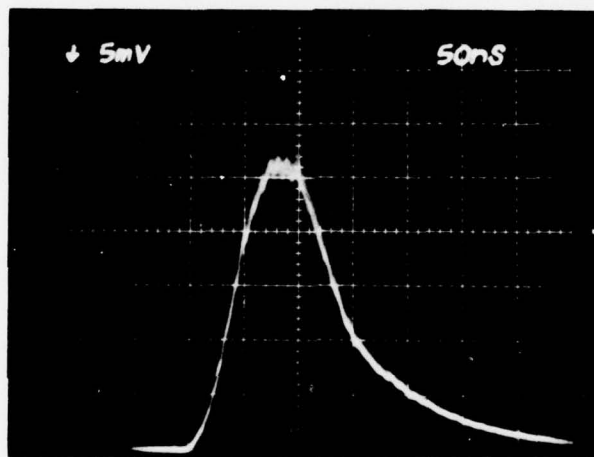


Figure 95 Temporal output of GaAs laser diode used for time response measurements:
a) ≈ 100 ns pulse, b) ≈ 20 ns pulse

The rise and decay of the photoconductive responses at different temperatures of samples 24AB16PC1 and 24AB14PC2 are shown in Figures 96-98. For 24AB16PC1, analyses of the photoconductivity decay curves in Figures 96a and 96b give a carrier lifetime of 360 ns at 287 K and a slightly lower value of 290 ns at 78 K. This decrease of lifetime with temperature is in accord with

the lifetimes calculated from the responsivities and listed in Table 14, but the decay-curve lifetimes are only $\approx 60\%$ of the calculated values. The discrepancies between the measured and calculated lifetimes can be attributed partly to errors in the measurements of R and n . Furthermore, because the absorption coefficient decreases rapidly with wavelength, the $0.91\text{ }\mu\text{m}$ laser radiation is absorbed in a narrower surface layer than the longer wavelength radiation, and therefore, is more susceptible to surface effects. In general, the carrier concentration at the surface is larger than that observed in the bulk material, and this also will decrease the measured lifetime.

(a)



(b)

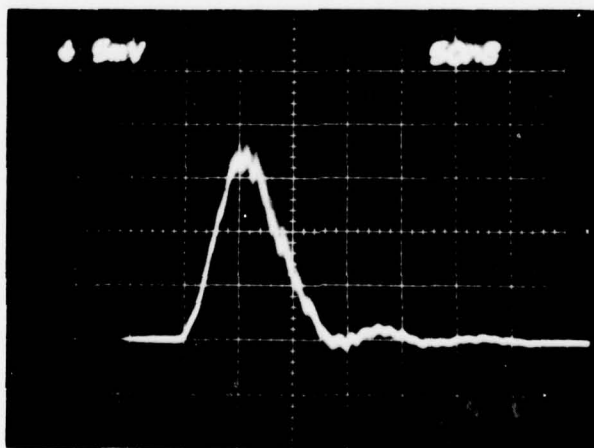
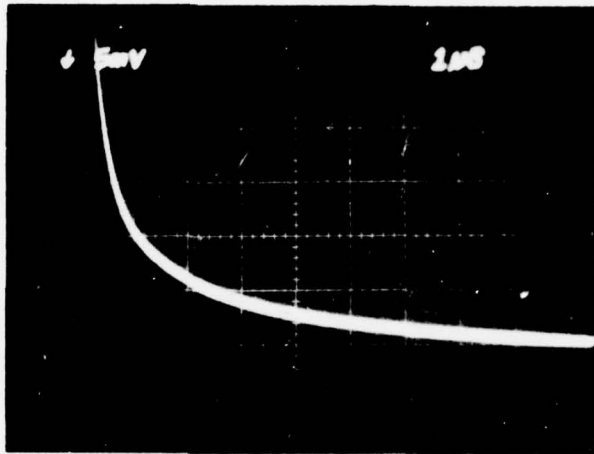


Figure 96 Decay of photoconductive response to GaAs diode laser pulse for element 24AB16PC1 at temperatures of: (a) 287 K and (b) 78 K

(a)



(b)

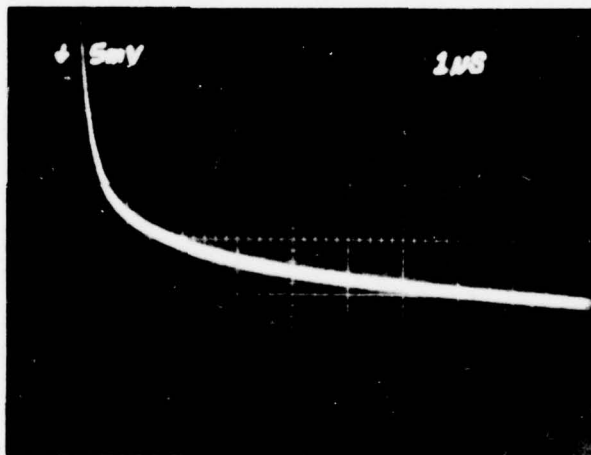
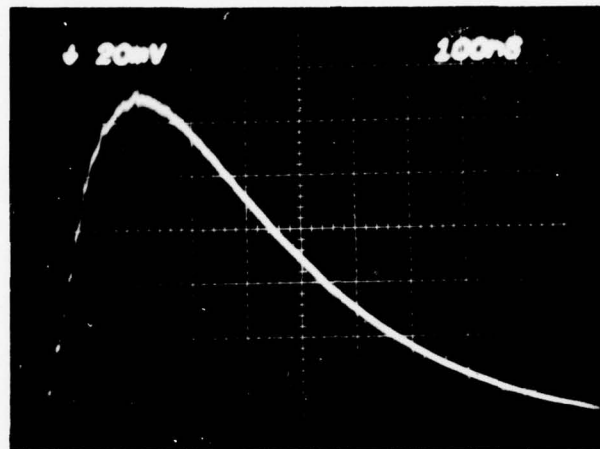


Figure 97 Effect of minority-carrier trapping on photoconductive decay for element 24AB16PC1 at temperatures of: (a) 35 K and (b) 14 K

(a)



(b)

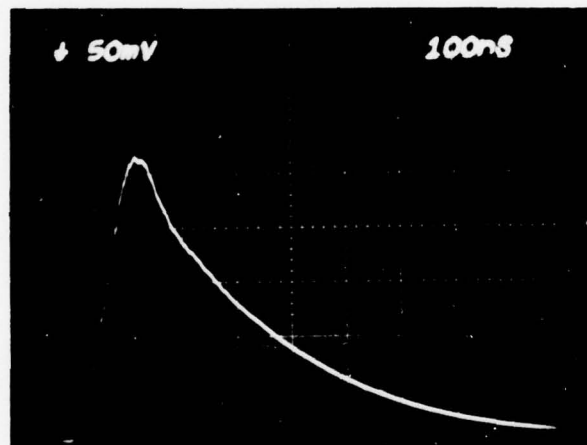


Figure 98 Decay of photoconductive response to GaAs diode laser pulse for element 24AB14PC2 at temperatures of: (a) 280 K and (b) 80 K

The lifetime in sample 24AB16PC1 did not change between 77 and 35 K, but at temperatures lower than 35 K, a long tail is observed in the decay curves. The tail is evident in Figures 97a and 97b, for which the time scale is ten times that in Figures 96a and 96b. The tail lengthens as the temperature is decreased from 35 to 14 K, but it is independent of temperature between 14 and 5 K. The lifetime at 5 K is $\geq 5 \mu\text{s}$, which is in agreement with the value calculated from the responsivity.

The low-temperature tail, which was observed in sample 24AA1PC1 as well as 24AB16PC1, is attributed to trapping of the minority carriers (holes) by shallow impurity or defect states. If the time that the hole is trapped exceeds the normal minority-carrier-lifetime, the number of holes available for electron-hole pair recombination is reduced. The number of electrons in the conduction band affected by this process equals the number of trapped holes and will decrease as the trapped holes are slowly released. The excess electron population caused by the minority-carrier trapping gives rise to an increased photocurrent, or responsivity, as was observed. The maximum number of holes that can be trapped depends on the number of trapping centers and the energy separation, E_T , between the trap levels and the top of the valence band. The magnitude of E_T determines the temperature at which trapping becomes effective and is of the order of 3 meV in sample 24AB16PC1. A larger value for E_T will increase the temperature at which trapping significantly enhances the performance of a detector.

The lifetimes deduced from the decay curves for sample 24AB14PC2 are very short, being 85 ns at 280 K (Figure 97a) and 40 ns at 77 K (Figure 97b). The lifetimes obtained from the decay curves have the same temperature dependences but are smaller than those calculated from the responsivity (Table 14). Time-response data were not taken at liquid-helium temperatures because the low sample-resistance caused ringing in the detection circuit.

At temperatures above 77 K, the majority-carrier-lifetime can be limited by radiative or Auger recombination-mechanisms involving band-to-band transitions. For samples 24AB16PC1 and 24AB14PC2, which have band gaps ≈ 0.3 eV above 77 K, radiative recombination is considered to be the mechanism that limits the electron lifetime in the bulk material. The radiative lifetime, τ_r , depends on the energy gap, carrier concentration, and temperature. The theoretical dependence of τ_r on these quantities has been calculated for samples 24AA1PC1 and 24AB16PC1, and the results are shown in Figures 99 and 100, respectively. The method for calculating τ_r is described in Section 8.5.

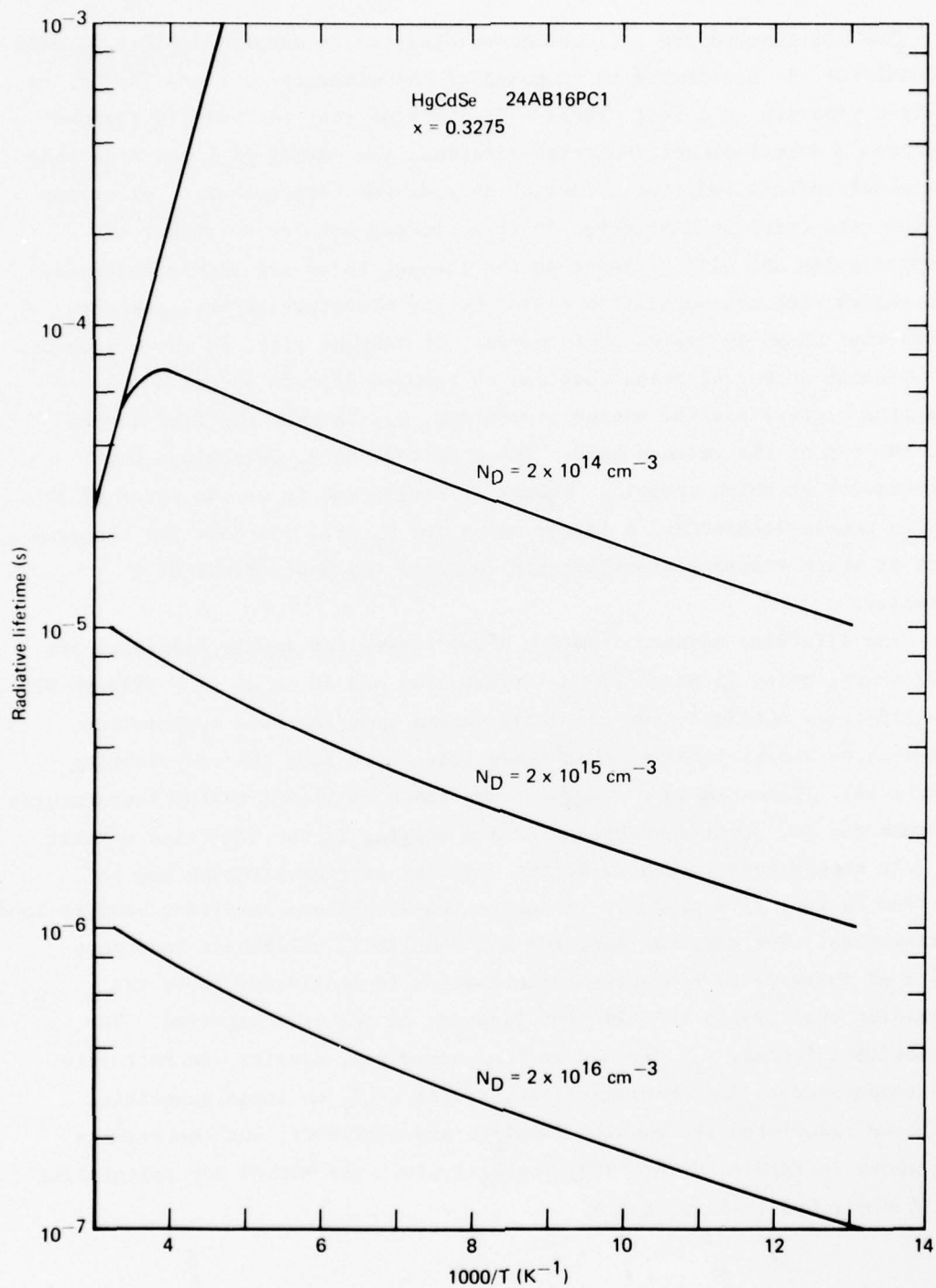


Figure 99 Theoretical estimate of the dependence of the radiative lifetime on temperature and electron concentration for element 24AB16PC1

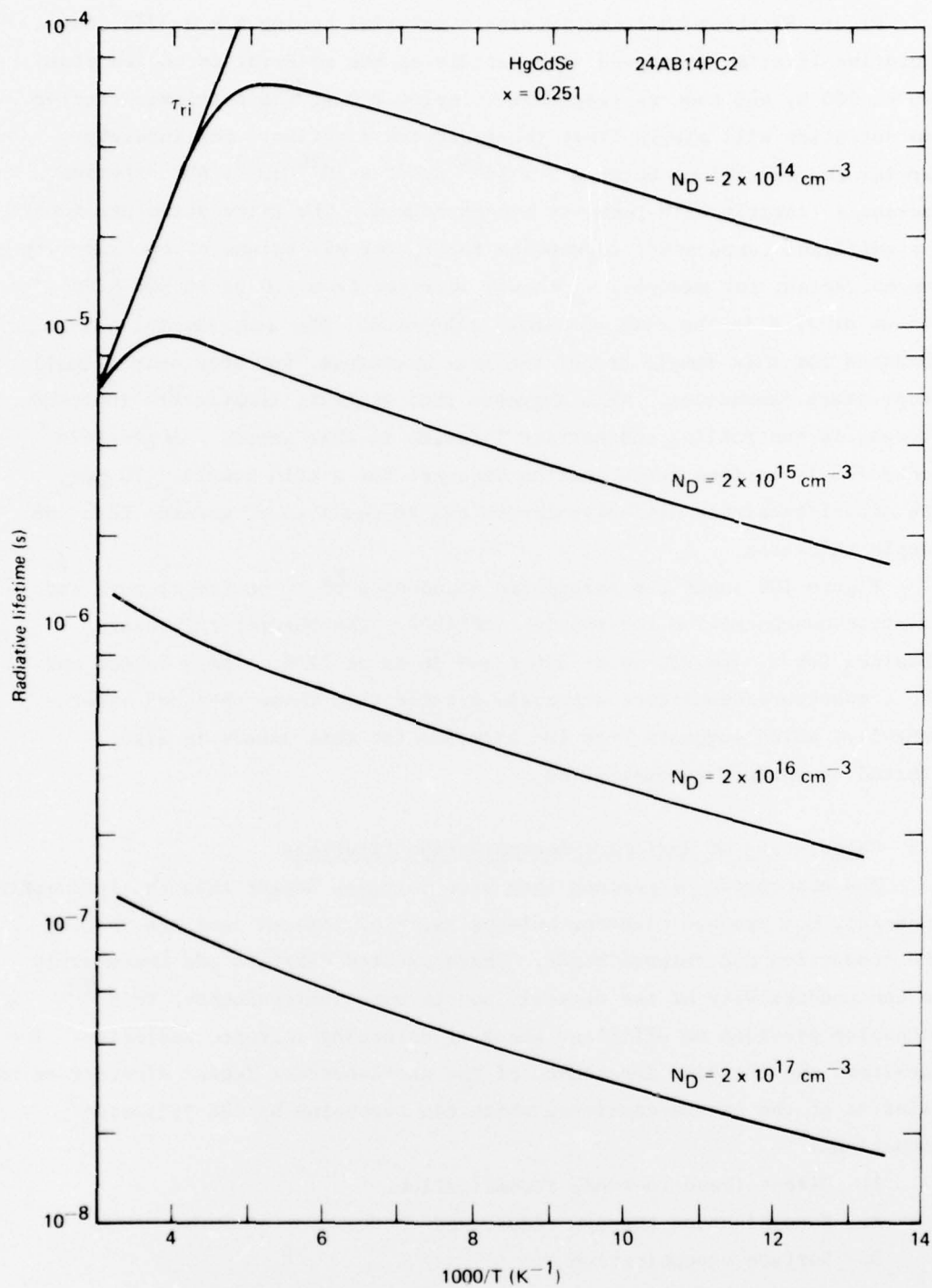


Figure 100 Theoretical estimate of the dependence of the radiative lifetime on temperature and electron concentration for element 24AB14PC2

Figure 99 shows that for intrinsic material having $x = 0.3275$, the radiative lifetime increases very rapidly as the material is cooled from 300 to 200 K, and that at temperatures below 200 K, the extrinsic-carrier concentration will always limit the radiative lifetime. For impurity carrier concentrations between 2×10^{14} and $2 \times 10^{16} \text{ cm}^{-3}$, the lifetime decreases linearly with impurity concentration. The calculation predicts a significant temperature dependence for τ_r for all values of the impurity concentration; for example, τ_r should decrease from 1.0 μs at 300 K to 0.1 μs at 77 K in the case of sample 24AB16PC1. The experimental values obtained for this sample are of the same magnitude, but show only a small temperature dependence. This suggests that another, temperature-independent process is controlling the carrier lifetime in this sample. A possible mechanism is surface recombination because, for a thin sample ($\leq 10 \mu\text{m}$), the minority-carrier diffusion-length can be equal to or greater than the sample thickness.

Figure 100 shows the calculated dependence of τ_r on temperature and electron concentration for sample 24AB14PC2. The theoretical values obtained for τ_r are 250 ns at 300 K and 36 ns at 77 K. These values and the temperature dependence are again greater than those obtained experimentally, which suggests that the lifetime for this sample is also limited by surface recombination.

8.5 Calculation of Radiative-Recombination Lifetimes

The absorption of photons that have energies larger than the fundamental band-gap, E_G , produce electron-hole pairs, i.e., excess carriers in both the conduction and valence bands. These excited carriers add momentarily to the conductivity of the crystal, and in pure semiconductors this mechanism provides an efficient means of detecting infrared radiation. The magnitude and the time dependence of the photo-current depend directly on the lifetime of the excess-carriers, which can recombine by the following mechanisms:

1. Direct (band-to-band) recombination,
2. Recombination through traps, and
3. Surface recombination.

These processes must be understood to evaluate a semiconductor as an infrared-detector material. Processes (2) and (3) are dependent on material growth and processing procedures, and process (1) provides a fundamental limit of the excess-carrier lifetime in a pure, defect-free semiconductor. Band-to-band recombination can result from either radiative or Auger recombination. Radiative decay occurs if an electron-hole pair recombines and a photon is simultaneously emitted that has an energy comparable with the energy gap of the semiconductor. The Auger process involves three carriers and occurs when two electrons collide in such a fashion that one electron drops into an empty valence-band state (hole) and imparts its recombination energy to the second electron, which is excited to a higher empty state in the conduction band. Both the radiative and Auger processes are dependent on temperature, impurity-electron concentration, and the fundamental energy-gap for direct transitions. Generally for semiconductors that have $E_G \geq 0.25$ eV, the radiative process limits the excess-carrier lifetime at temperatures below 200 K. Auger recombination is dominant for small-gap materials and at higher temperatures. Only the radiative process will be discussed here because it is the only process applicable to the HgCdSe alloys with energy gaps ≥ 0.25 eV, for which photoconductivity data are reported here.

We denote the instantaneous electron and hole concentrations in a semiconductor by N and P , respectively. At thermal equilibrium, there is a steady thermal-excitation of electron-hole pairs at a rate G_0 that is balanced by a steady recombination at a rate R_0 . Thus, the thermal-equilibrium electron and hole densities, which we denote by N_0 and P_0 , remain constant. As the semiconductor absorbs radiation, electron-hole pairs are excited, and N and P increase at the same rate. If the photo-excited charge-carriers decay only by recombination, as we assume here, then the rates of decay of N and P are equal. Thus,

$$N - N_0 = P - P_0. \quad (89)$$

We shall assume that the recombination rate is proportional to both N and P , so that

$$R = ANP, \quad (90)$$

where A is a constant. At thermal equilibrium,

$$R_0 = AN_0P_0 = AN_i^2, \quad (91)$$

where N_i is the intrinsic carrier concentration. The rate of decay of the excess electrons is assumed to be proportional to the density of excess electrons:

$$\begin{aligned} \left[\frac{\partial}{\partial t} (N-N_0) \right]_{\text{recombination}} &= \frac{1}{\tau_r} (N-N_0). \\ &= R-R_0. \end{aligned} \quad (92)$$

The proportionality constant has been written as $1/\tau_r$, and τ_r is called the recombination lifetime. It is the time required for the excess electron concentration to decay by a factor $1/e$. If the expressions for R and R_0 from Equations (90) and (91) are substituted into Equation (92), the result after some transpositions is

$$\tau_r = \frac{N_i^2 (N-N_0)}{R_0 (NP-N_i^2)}. \quad (93)$$

Because the excess-electron density is equal to the excess hole density, as was pointed out in Equation (89), Equation (93) can be reduced to the following expression:

$$\tau_r = \frac{N_i^2}{R_0} \left[\frac{1}{(N_0+P_0) + (N-N_0)} \right]. \quad (94)$$

The condition of charge neutrality requires that

$$N_0 - P_0 = N_D - N_A, \quad (95)$$

where N_D and N_A are the concentrations of ionized donors and acceptors, respectively. Equation (95) together with the relation, $N_0P_0 = N_i^2$, can be used to obtain Equation (94) in the following form:

$$\tau_r = \frac{N_i^2}{R_0} \left[\frac{1}{\{4N_i^2 + (N_D - N_A)^2\}^{1/2} + (N-N_0)} \right]. \quad (96)$$

This expression can be simplified for two cases of practical interest. The first case is that for which both $(N-N_0)$ and $(N_D - N_A)$ are much smaller than N_i (near-intrinsic case); then Equation (96) reduces to

$$\tau_{ri} \approx \frac{N_i}{2R_0} \quad (97)$$

The second case is that for which both $(N-N_0)$ and N_i are much smaller than N_D-N_A (extrinsic n-type case); then Equation (96) reduces to

$$\tau_{rn} \approx \frac{N_i^2}{R_0(N_D-N_A)} \quad (98)$$

The equilibrium radiative-recombination rate, R_0 , can be obtained by utilizing the principle of detailed balance, which requires that the absorption of photons to produce electron-hole pairs be exactly balanced by the emission of photons when electron-hole pairs recombine. Then,

$$R_0 = G_0 = \int_0^{\infty} \frac{c}{n^*} \alpha(\nu) Q(\nu) d\nu \quad (99)$$

In this expression, c is the speed of light in vacuum, ν is the photon frequency, n^* is the semiconductor refractive-index, α is the absorption coefficient for band-to-band transitions, and Q is the Planck distribution function,

$$Q(\nu) = \frac{8\pi\nu^2 (n^*)^3}{c^3} \left[\frac{1}{\exp(h\nu/k_B T) - 1} \right] \quad (100)$$

In Equation (100), h is Planck's constant, k_B is the Boltzmann constant, and T is the absolute temperature. In Equations (99) and (100), the index of refraction is generally a function of ν .

To calculate τ_r at a given temperature, N_i must first be calculated from Equation (75) of Section 7.7, subject to the condition that $(N_D-N_A) = 0$. Then R_0 is calculated from Equation (99), with the functions $n^*(\nu)$ and $\alpha(\nu)$ as given in Section 7.7. Finally, N_i and R_0 are substituted into Equations (97) and (98) to obtain the intrinsic and extrinsic radiation-recombination lifetimes. The lifetimes can be calculated with precision if the semiconductor energy-band parameters E_G , P , and Δ are accurately known.

9. DEVICE FEASIBILITY

9.1 Detectivity

If Johnson noise, J_n , is assumed to be the dominant source of noise, an estimate can be made of the noise equivalent power (NEP) and detectivity, D^* , of a photoconductive element. The noise equivalent power is given by the relation

$$NEP = \frac{J_n}{\mathcal{R}} = \frac{\sqrt{4kTR_s}}{\mathcal{R}}, \quad (101)$$

and the detectivity can be calculated from the relation

$$D^* = \frac{\sqrt{A}}{NEP} = \frac{\sqrt{\ell\omega}}{NEP}, \quad (102)$$

where A is the surface area of the specimen, R_s is its resistance, and \mathcal{R} is the photoconductive responsivity.

Equations (101) and (102) and photoconductive responsivity data were used to calculate D^* for the photoconductivity specimens 24AA1PC1, 24B16PC1, and 24AB14PC2. The results are summarized in Table 15. The responsivity values in Table 15 are either the values for the maximum bias voltage used or the bias voltage at which departure from a linear volt-ampere characteristic began. It must be emphasized that the sample geometry, thickness, surface treatment, and lead contacts were not optimized to obtain the highest possible responsivity or detectivity. Time was not sufficient to develop the surface-treatment, surface-passivation, and lead-bonding methods that are required for fabricating high-responsivity, low-NEP detector elements from $Hg_{1-x}Cd_xSe$ crystals. We believe that the D^* values in Table 15 represent lower limits and that higher D^* values can be obtained for $Hg_{1-x}Cd_xSe$ that has 1×10^{16} electrons/cm³.

TABLE 15 CALCULATED DETECTIVITY FOR JOHNSON-NOISE-LIMITED
CONDITION OF $\text{Hg}_{1-x}\text{Cd}_x\text{Se}$ PHOTO-HALL-BAR ELEMENTS

Sample no.	Sample thickness (mm)	Mole fraction of CdSe, x	Temperature (K)	Resistance (Ω)	Bias voltage (V)	Wavelength (μm)	Photo-conductive responsivity (V/W)	Calculated detectivity, D^* ($\text{cm}\cdot\text{Hz}^{1/2}/\text{W}$)
24AA1PC1	0.005	0.352	77	260	3.5	2.65	102	1.3×10^{10}
			5	230	2.5	3.08	720	4.0×10^{11}
24AB16PC1	0.0075	0.328	77	217	1.5	3.15	70	8.4×10^9
24AB14PC2	0.020	0.251	77	6.0	0.50	4.95	0.24	1.8×10^8
			5	3.4	0.20	5.65	0.22	9.6×10^8

In the wavelength region of 2.6-5 μm , responsivity values up to 100 V/W were measured for $\text{Hg}_{1-x}\text{Cd}_x\text{Se}$ crystals at 77 K. The responsivity of $\text{Hg}_{1-x}\text{Cd}_x\text{Se}$ detector elements can be made much higher if the extrinsic electron concentration can be reduced and surface effects can be minimized. At a 77 K operating temperature, the detectivity (D^*) values calculated from the photoconductive response of $\text{Hg}_{1-x}\text{Cd}_x\text{Se}$ crystals ranged from 1.8×10^8 to $1.3 \times 10^{10} \text{ cm}\cdot\text{Hz}^{1/2}/\text{W}$. At 5 K, the responsivities were as high as 720 V/W and the calculated D^* values ranged from 9.6×10^8 to $4.0 \times 10^{11} \text{ cm}\cdot\text{Hz}^{1/2}/\text{W}$. At a wavelength of 3.0 μm , the 300 K background limiting value of D^* is $1 \times 10^{12} \text{ cm}\cdot\text{Hz}^{1/2}/\text{W}$ for an ideal photoconductor with a 2π sr field of view. The D^* values obtained for the $\text{Hg}_{1-x}\text{Cd}_x\text{Se}$ alloys at this stage of their development are encouraging because a decrease of their extrinsic electron concentration to $3 \times 10^{15} \text{ cm}^{-3}$, which is only a few times smaller than concentrations routinely achieved now, will increase their D^* values to the theoretical limit.

10. CONCLUSIONS

10.1 Phase Diagram of the HgSe-CdSe Systems

The experimentally-determined liquidus and solidus curves for the pseudobinary HgSe-CdSe system are calculable from the theory of ideal solutions and the thermodynamic data for HgSe and CdSe if minor corrections are made to account for small contributions to the entropy of mixing from interatomic-force changes. The liquidus temperature-composition curve implies a value for the entropy of mixing of $-2.69[x(1-x)]$ J/mol, and the solidus curve conforms closely with that of an ideal solution. The ideal-solution behavior of the solid HgSe-CdSe solutions is consistent with the small variation with x of the interatomic spacing.

The $\text{Hg}_{1-x}\text{Cd}_x\text{Se}$ alloys with $x < 0.55$ crystallize from the melt with the cubic zincblende structure, and alloys with $x > 0.55$ crystallize from the melt with the hexagonal wurtzite structure. All compositions of $\text{Hg}_{1-x}\text{Cd}_x\text{Se}$ alloys that can be used for infrared detection crystallize with the zincblende structure.

The solid phase of $\text{Hg}_{1-x}\text{Cd}_x\text{Se}$ that is in equilibrium with the liquid phase transforms by peritectic reaction at $947 \pm 4^\circ\text{C}$ from the zincblende to the wurtzite crystal-structure.

The narrow miscibility gap in the solid phase between the zincblende and wurtzite crystallographic phases has no perceptible effect on the solidus curve for the HgSe-CdSe system.

10.2 Alloy Preparation and Crystal-Growth Methods

The $\text{Hg}_{1-x}\text{Cd}_x\text{Se}$ alloys with $0 < x < 0.6$ can be prepared by reacting the constituent elements in sealed, evacuated, quartz capsules.

Single crystals of $\text{Hg}_{1-x}\text{Cd}_x\text{Se}$ alloys can be grown by the Bridgman method. Single crystals 1 cm diam and 14 cm long were prepared under a variety of temperature gradients and growth rates.

The radial, compositional homogeneity of Bridgman-grown crystals is greater for larger temperature-gradients at the solid-liquid interface during crystal growth.

The pressure of the vapor in equilibrium with stoichiometric, molten $\text{Hg}_{1-x}\text{Cd}_x\text{Se}$ increases from 5.5 MPa (55 atm) for $x = 0$ to 15 MPa (150 atm) for $x = 0.33$.

10.3 Crystal Preparations and Characterization

The average x -value for a $\text{Hg}_{1-x}\text{Cd}_x\text{Se}$ crystal or slice can be determined with precision from its mass density. The crystalline perfection, density of low-angle grain boundaries, angular misorientation of grains, and crystallographic orientation of $\text{Hg}_{1-x}\text{Cd}_x\text{Se}$ crystal slices can be determined from Laue x-ray topographs.

The compositional homogeneity of $\text{Hg}_{1-x}\text{Cd}_x\text{Se}$ crystal slices can be quantitatively determined from measurements of the infrared transmission edge at 300 K for 1 mm diam areas at regularly spaced locations on each slice.

$\text{Hg}_{1-x}\text{Cd}_x\text{Se}$ crystals as-grown from the melt are n-type and have extrinsic-electron concentrations that range from $3 \times 10^{18} \text{ cm}^{-3}$ for $x = 0$ to as low as $1.3 \times 10^{16} \text{ cm}^{-3}$ for alloys with $x < 0.4$.

The annealing in vacuum at 200-300°C of $\text{Hg}_{1-x}\text{Cd}_x\text{Se}$ crystals typically reduces their extrinsic-electron concentration by an order of magnitude and doubles the low-temperature electron mobility.

The annealing of $\text{Hg}_{1-x}\text{Cd}_x\text{Se}$ crystals at 200-300°C in Se vapor does not significantly alter the extrinsic-electron concentration but does increase the ratio of the electron mobility at 4.2 K to the mobility at 300 K.

$\text{Hg}_{1-x}\text{Cd}_x\text{Se}$ crystals that were prepared from 99.9999% pure constituent-elements had tens of parts-per-million impurity concentrations according to emission-spectrographic analyses.

10.4 Electrical Properties of the $\text{Hg}_{1-x}\text{Cd}_x\text{Se}$ Alloys

$\text{Hg}_{1-x}\text{Cd}_x\text{Se}$ alloys are invariably n-type, with conduction-electron concentrations from $3 \times 10^{18} \text{ cm}^{-3}$ in as-grown HgSe ($x = 0$) to as low as $1.3 \times 10^{16} \text{ cm}^{-3}$ in as-grown alloys with $x < 0.4$. The conduction-electrons in as-grown $\text{Hg}_{1-x}\text{Cd}_x\text{Se}$ alloys are apparently the result of Hg in excess of stoichiometry.

The conduction-electron mobility for a fixed electron concentration decreases as x increases (for $x > 0.1$).

The conduction-electron mobility for a fixed x -value increases as the electron concentration decreases.

The conduction-electron mobility is limited at low temperatures by ionized-impurity scattering and at 300 K by lattice scattering.

10.5 Infrared Absorption and Dependence of Energy Gap on Composition of

$\text{Hg}_{1-x}\text{Cd}_x\text{Se}$ Alloys

The energy-gap values determined from absorptance spectra of $\text{Hg}_{1-x}\text{Cd}_x\text{Se}$ alloys with $0.15 < x < 0.37$ are slightly smaller than values obtained by linear interpolations between the energy-gaps of HgSe and CdSe.

The energy gap increases as the temperature increases from 5 to 300 K for $\text{Hg}_{1-x}\text{Cd}_x\text{Se}$ alloys with $0.15 < x < 0.37$, and the temperature coefficient of the energy gap decreases as x increases. The functional relationships between energy gap, E_G , in electronvolts and x for $0 < x < 0.3$ are $E_G = -0.195 + 1.70x$ at 80 K, $E_G = -0.128 + 1.66x$ at 200 K, and $E_G = -0.061 + 1.57x$ at 300 K.

The band-structure theoretical model developed for InSb fits the experimental data for the $\text{Hg}_{1-x}\text{Cd}_x\text{Se}$ alloys.

10.6 Infrared Photoconductivity

The infrared photoconductive responsivity of $\text{Hg}_{1-x}\text{Cd}_x\text{Se}$ is a maximum at a wavelength corresponding to the sum of the band-gap energy and the Fermi energy of conduction-band electrons.

The excess carrier lifetime as determined from photoconductivity time-response measurements is limited at 77 and 300 K by radiative recombination of electron-hole pairs. Below 30 K, the excess carrier lifetime is high because of minority-carrier trapping.

10.7 Device Feasibility

The 77 K infrared photoconductive detectivity of $\text{Hg}_{1-x}\text{Cd}_x\text{Se}$ alloys with approximately 10^{16} conduction-electrons per cm^3 is between 1 and 2 orders of magnitude lower than the theoretical maximum for 300 K background operation at wavelengths between 2.5 and 5 μm . Because the photoconductive responsivity of the $\text{Hg}_{1-x}\text{Cd}_x\text{Se}$ alloys is inversely proportional to the square of the conduction-electron concentration, the detectivity will be the theoretical maximum for alloys that have approximately 5×10^{15} electron concentrations per cm^3 .

Additional development is required to prepare purified $\text{Hg}_{1-x}\text{Cd}_x\text{Se}$ alloys with conduction-electron concentrations smaller than $5 \times 10^{15} \text{ cm}^{-3}$. Methods also must be developed to chemically dope $\text{Hg}_{1-x}\text{Cd}_x\text{Se}$ to compensate the excess donors and to convert the material from n-type to p-type.

Unlike other semiconductor alloys for which the crystal lattice constant varies with composition and local variations of composition cause severe strains in the crystals and can preclude the growth of large crystal grains, the variation with x of the lattice constant is negligible for the zincblende form of $\text{Hg}_{1-x}\text{Cd}_x\text{Se}$ alloys. Even if HgCdSe melts are rapidly cooled and have local variations of composition, there is no barrier to the formation of large single crystals. The dendritic growth that accompanies constitutional supercooling need not disrupt the crystal lattice formations in the case of HgCdSe alloys; the dendrites may have a considerably different composition than the surrounding alloy but yet have the same crystalline orientation. For this reason, the growth of HgCdSe single crystals by the Bridgman method merits continued development. Fast growth rates through large temperature gradients may yield large single crystals that are inhomogeneous only on a microscopic scale. Subsequent high-temperature annealing for relatively short times could then be effective in homogenizing the composition of the single-crystalline ingot or slices from the ingot.

The research reported here has demonstrated that the development of $\text{Hg}_{1-x}\text{Cd}_x\text{Se}$ for infrared sensor applications is feasible. The suggested additional developmental work can make possible the fabrication of high-detectivity and large-area photoconductive detectors.

REFERENCES

1. E. Cruceanu, N. Nistor, and D. Niculescu, Growth of HgSe Crystals from Solutions and Some of Their Properties, *Kristallografiya* 11, 305 (1966).
2. H. E. Swanson, N. T. Gilfrich, and M. I. Cook, *Circ. U.S. Natl. Bur. Std.* 7, 35 (1957).
3. H. P. Singh and B. Dayal, Lattice Parameters and Thermal Expansion of Zinc Telluride and Mercury Selenide, *Acta. Cryst.* A26, 363 (1970).
4. A. Kalb and V. Leute, The Miscibility Gap of the System CdSe-HgSe, *Phys. Stat. Solidi* 5, K199 (1971).
5. H. E. Swanson, N. T. Gilfrich, and M. I. Cook, *Circ. U.S. Natl. Bur. Std.* 7, 539 (1957).
6. M. V. Kot and V. A. Mshenskii, Structure and Electrical Properties of the CdSe-HgSe System, *Izv. Akad. Nauk SSSR* 28, 1067 (1964).
7. A. D. Stuckes, and G. Farrell, Electrical and Thermal Properties of Alloys of CdTe and CdSe, *J. Phys. Chem. Solids* 25, 477 (1964).
8. M. E. Cruceanu and D. Niculescu, Solid Solutions in the CdS-CdTe and HgSe-CdSe Systems, *Compt. Rend.* 261, 935 (1965).
9. S. L. Lehoczky, J. G. Broerman, D. A. Nelson, and C. R. Whitsett, Temperature Dependent Electrical Properties of HgSe, *Phys. Rev. B* 9, 1598 (1974).
10. P. A. Slodowy and W. Giriat, The Dependence of the Energy Gap on the Composition in the Mixed Crystals $Cd_{\sqrt{1-v}}Hg_{1-v}Se$, *Phys. Stat. Solidi* 48, 463 (1971).
11. B. Ray and P. M. Spencer, Phase Diagram of the System HgTe-CdTe, *Phys. Stat. Solidi* 22, 371 (1967).
12. T. C. Harman, in *Physics and Chemistry of II-VI Compounds*, ed. by M. Aven and J. S. Prener (North-Holland, Amsterdam, 1967), p. 784.
13. A. J. Strauss and L. B. Farrell, Hg-Se System, *J. Inorganic Nucl. Chem.* 24, 1211 (1962).
14. F. A. Shunk, *Constitution of Binary Alloys*, Second Supplement (McGraw-Hill, New York, NY, 1969) pp. 223-224.

15. J. Steininger, Thermodynamics and Calculation of the Liquidus - Solidus Gap in Homogeneous, Monotonic Alloy Systems, *J. Appl. Phys.* 41, 2713 (1970).
16. A. J. Strauss and J. Steininger, Phase Diagram of the CdTe-CdSe Pseudobinary System, *J. Electrochem. Soc.: Solid State Sci.* 117, 1420 (1970).
17. *Handbook of Chemistry and Physics*, ed. by R. C. Weast (Chemical Rubber Co., Cleveland, 1974), pp. D185-D186.
18. *Ibid.*, pp. B68.
19. R. F. Brebrick, Pressures of Hg and Selenium over HgSe (c) from Optical Density Measurements, *J. Phys. Chem. Solids* 43, 3846 (1965).
20. W. J. Woesten, The Vapor Pressure of Cadmium Selenide, *J. Phys. Chem.* 65, 1949 (1961).
21. H. A. Bowman and R. M. Schooner, Procedure for High Precision Density Determinations by Hydrostatic Weighing, *J. Res. Natl. Bur. Std. (U.S.)* 71C, 179 (1967).
22. L. N. Swink and M. J. Brau, Rapid Nondestructive Evaluation of Macroscopic Defects in Crystalline Materials: The Laue Topography of (Hg, Cd)Te, *Met. Trans.* 1, 629 (1970).
23. L. J. van der Pauw, A Method of Measuring Specific Resistivity and Hall Effects of Discs of Arbitrary Shape, *Philips Research Reports* 13, 1 (1958).
24. J. Stankiewicz, W. Giriat, and W. Dobrowski, Shubnikov-de Haas Oscillations in $\text{Cd}_{1-x}\text{Hg}_x\text{Se}$, *Phys. Stat. Solidi* B61, 267 (1974).
25. E. O. Kane, Band Structure of Indium Antimonide, *J. Phys. Chem. Solids* 1, 249 (1957).
26. Z. I. Kir'iashekina, F. M. Popov, D. N. Bilenko, and V. I. Kir'iashekina, An Investigation of the Dielectric Permittivity of Semiconductors, *Zh. Tekh. Fiz.* 27, 85 (1957) [*Sov. Phys. - Tech. Phys.* 2, 69 (1957)].
27. D. Berlincourt, H. Jaffe, and L. R. Shiozawa, Electroelastic Properties of the Sulfides, Selenides, and Tellurides of Zinc and Cadmium, *Phys. Rev.* 129, 1009 (1963).

28. D. G. Seiler, R. R. Galazka, and W. M. Becker, Band Structure of HgSe: Band Parameter Determinations from Effective-Mass Data, and Concentration Dependence and Anisotropy of Beating Effects in the Shubnikov-de Haas Oscillations, Phys. Rev. B 3, 4274 (1971).
29. R. G. Wheeler and J. O. Dimmock, Exciton Structure and Zeeman Effects in Cadmium Selenide, Phys. Rev. 125, 1805 (1962).
30. T. S. Moss, Optical Properties of Semiconductors, (Butterworth's Publications, London, 1959), pp. 12.
31. J. G. Broerman, Dielectric Function Anomalies in Zero-Gap Semiconductors, Physics of Semiconductors; Proceedings of the Eleventh International Conference, (Polish Scientific Publishers, Warsaw, Poland, 1972), p. 417.
32. R. A. Reynolds, HgCdTe IR Detector Processing Techniques, Air Force Avionics Laboratory, Report No. AFAL-TR-69-252 (1969).